Review

International Journal of Modern Physics B
Vol. 27, No. 8 (2013) 1330004 (79 pages)

DOI: 10.1142/S0217979213300041

World Scientific
www.worldscientific.com

ELASTIC, PLASTIC, CRACKING ASPECTS OF THE HARDNESS OF MATERIALS

R. W. ARMSTRONG

Center for Energetic Concepts Development, University of Maryland, College Park, MD 20742, USA
rona@umd.edu

W. L. ELBAN

Department of Engineering, Loyola University Maryland, Baltimore, MD 21210, USA
welban@loyola.edu

S. M. WALLEY

Department of Physics, Cavendish Laboratory, University of Cambridge, Cambridge CB3 OHE, UK
smw14@cam.ac.uk

Received 28 January 2013
Accepted 31 January 2013
Published 11 March 2013

The hardness properties of materials are tracked from early history until the present time. Emphasis is placed on the hardness test being a useful probe for determining the local elastic, plastic and cracking properties of single crystal, polycrystalline, polyphase or amorphous materials. Beginning from connection made between individual hardness pressure measurements and the conventional stress–strain properties of polycrystalline materials, the newer consideration is described of directly specifying a hardness-type stress–strain relationship based on a continuous loading curve, particularly, as obtained with a spherical indenter. Such effort has received impetus from order-of-magnitude improvements in load and displacement measuring capabilities that are demonstrated for nanoindentation testing. Details of metrology assessments involved in various types of hardness tests are reviewed. A compilation of measurements is presented for the separate aspects of Hertzian elastic, dislocation-mechanics-based plasticity and indentation-fracture-mechanics-based cracking behaviors of materials, including elastic and plastic deformation rate effects. A number of test applications are reviewed, most notably involving the hardness of thin film materials and coatings.

Keywords: Hardness; elasticity; Hertz; plasticity; dislocations; cracking; indentation fracture mechanics; stress-strain curves; metrology; indentation size effect (ISE); Hall–Petch relation.

1. Introduction

The hardness test involves a shaped indenter tip, a specimen surface and a means of applying force and/or displacement associated with initiating contact and either intended blunting of the indenter or penetration of the specimen surface, then to be followed by unloading separation of the indenter and specimen. Walley has provided an historical context for the hardness test.[1] Our purpose here is to carry on by providing background to a number of developments on the subject and to reviewing researches on the topic until the present time. We begin by noting that the subjects of hardness and hardness testing are far too wide-ranging for complete coverage to be attempted in any single review article. Evidence for the preceding statement is provided by inclusion of a substantial list of books on the combined topics along with an additional listing of a number of review articles and conference proceedings on focused sub-topics. In the current report, particular emphasis is given to a number of issues:

(1) the governing equations for elastic, plastic and cracking behaviors at hardness indentations;
(2) comparison of the hardness and conventional stress–strain descriptions, leading to the relatively new consideration of a direct hardness-based stress–strain curve;
(3) metrological aspects of hardness testing, especially as relating to the recent explosion of activity on nanoindentation testing;
(4) selected descriptions of results reported on each of the subjects of
    (a) elastic hardness and rebound measurements,
    (b) the onset of indentation plasticity, particularly as described in terms of dislocation deformations and atomic modeling results and
    (c) the occurrence of cracking and indentation fracture mechanics measurements;
(5) hardness measurements on
    (a) crystals and anisotropy of slip deformations including dislocation-initiated cracking at slip band intersections,
    (b) Hall–Petch (H–P) aspects of polycrystal and composite polyphase deformations and
    (c) amorphous material shear banding and cracking and
(6) selected applications of hardness testing, especially, to thin films and coatings.

1.1. *Historical aspects*

We begin with mention of an early 17th century contribution by Hooke who signaled the beginning of the microscopic examination of materials via, at relatively low optical magnification, observing the rounded end of a needle point.[2] It waited until the 19th century for the microscopic examination of metals to gain significantly greater impetus from the seminal work by Sorby[3] while the idea of making

use of the "needle point" to reveal in any manner the lattice structure of a metal or to be a materials probe was only to be significantly brought forward in the 20th century. For example, Mueller presented a review of field ion microscopy observations of the lattice structure of crystal atoms and imperfections able to be made with atomic scale resolutions for needle points of $\sim 5 - \sim 150$ nm tip radii for tungsten emitters.[4] This was to be followed by a news note on a new technique of scanning tunneling microscopy that employed a sharpened tungsten tip positioned ~ 5 nm above a material conducting surface in order to reveal its topography at atomic scale resolution; these researchers being interested themselves in the use of a sharp indenter tip for measuring the ultimate hardness of a material with a smallest tipped indenter.[5] In 1986, Binnig and Rohrer shared, with Ernst Ruska for his earlier work on electron optics and designing the first electron microscope, the Nobel Prize in Physics for inventing the Scanning Tunneling Microscope (Atomic Force Microscope) based on the tunneling of electrons between the sharp tip of a probe and a specimen surface.[6]

Current probe-type research activities are reported at sub-nanometer dimensions for AFM measurements of an exaggerated difference in chemical bond order of 0.07 nm due to interaction at a separation of 0.34 nm between a tip-attached CO molecule and atomic displacements on a C60 fullerene surface structure.[7] The dimensional resolution compares with STM images of 0.06 nm dislocation slip-step heights revealed on an indented (001) gold crystal surface.[8] Blackman, Mate and Philpott[9] have reported on application of the AFM, as developed by Binnig and colleagues, to study discontinuous plastic deformation "pops" during tungsten tip loading of (soft solid) polymeric cadmium arachidate single and multi-atomic layer films deposited onto a silicon single crystal surface.

In a follow-up report containing Fig. 1 for a number of vertically offset pairs of curves for AFM interaction with different types of lubricant films on a silicon

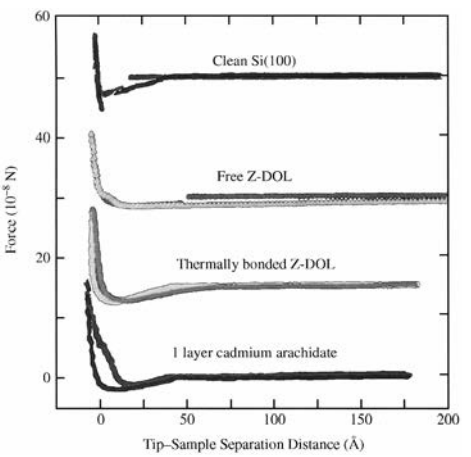

Fig. 1. Force on AFM tips associated with contact and withdrawal from different surface layers.[10]

surface, Mate[10] describes the upper broken curve for the AFM tungsten tip approaching the silicon surface until an attractive (van der Waals) force produces the indicated sudden jump to establish contact at ~ 2.0 nm distance between a meniscus of contaminant molecules on the tip and the silicon crystal surface and then, for the adjacent lower curve, the contaminated tip must be withdrawn over a larger distance to achieve a total break-free condition from the meniscus. The lowest pair of curves was obtained in meniscus-free condition for the tip and a single layer of soft solid cadmium arachidite material in which case evidence is shown of the material layer of ~ 2.8 nm thickness having been indented to a depth of ~ 2.0 nm. Such research effort has been directed to achieving a better understanding of lubrication and friction for designing and manufacturing electronic disk drives at the scale of atomic and molecular dimensions. The modern researches have counterpart hardness connection in pioneering hardness-based researches by Tabor and Winterton[11] on measurement of van der Waals forces between cylindrically-curved mica sheets at $\sim 5 - \sim 30$ nm separations and on wear-related measurement of adhesive forces by Pashley *et al.*[12]

Gane and Cox[13] obtained the scanning electron microscope (SEM) image of Fig. 2 in a study of indentation sizes made as small as 200 nm with a field-ion-microscope tungsten indenter applied to a gold crystal surface. The measurements made at small loads nevertheless led to clear determination of an indentation size effect (ISE) for the mean hardness pressure over a range in indentation sizes from ~ 0.5 mm down to ~ 0.2 μm through showing a substantial increase at smaller size. The measurements were achieved with a series of spherical indenters of different diameters so as to keep a constant ratio of indentation-diameter-to-ball-diameter,

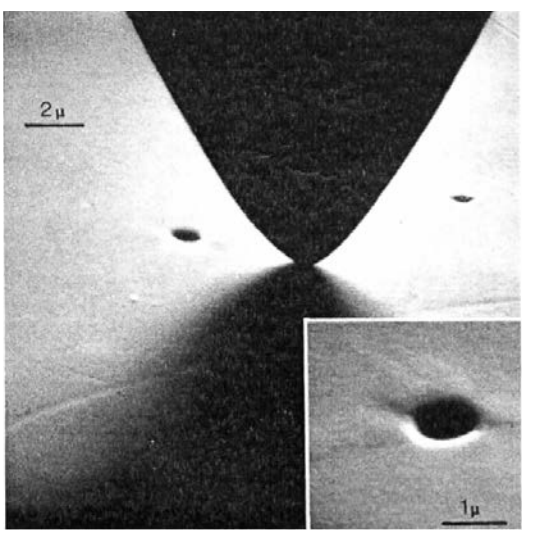

Fig. 2. SEM picture of tungsten indentation in gold.[13]

(d/D). The ISE was attributed to an increase in stress necessary to operate dislocation sources.

Follow-up research was done on the same topic of electron microscope examination of the indentation process by Gane.[14] Experiments were performed both in the SEM and in the transmission electron microscope (TEM). A smallest load of $\sim 10^{-6}$ N was applied. Very interestingly, Gane included study of the compression of ~ 2 mm and ~ 0.5 μm diameter spherical gold crystals with finding a substantial increase in hardness for the smaller particles. The additional case of blunting of a soft (aluminum) indenter tip against a hard surface was included. The initial dislocations involved in the blunting were observed to escape from the nearby indenter surface but were internally built-up at later stages of blunting. The latter case of intended indenter blunting relates to a much later report, made at very different hardness pressures and dimensional scales, of a hardened steel ball being blunted in the course of producing ring cracking in an industrial diamond material.[15]

1.2. *Analysis*

During the latter part of the 19th century and with a burst of activity at the beginning of the 20th century, a number of research reports centered on a combination of interests, first, in the new subject of contact mechanics and, secondly, of equal attention from industry in both reporting and interpreting indentation hardness test results. Here, we first concern ourselves with the breakthrough analysis of Hertz[16,17] in establishing the modern mechanics of indentation hardness testing. Hueber[18] later reported on the full elastic stress state beneath an elastic contact. And Hencky[19] provided pioneering insight on the nature of the deformation pattern produced by a plastic indentation.

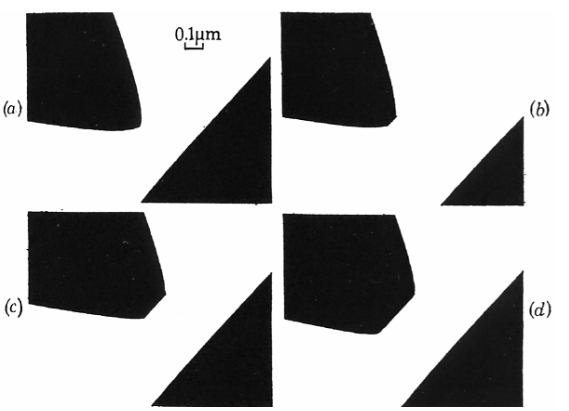

Fig. 3. TEM shadow micrographs of blunting of a gold indenter tip pressed against a hard surface and including contact pressure estimations: (a) pre-contact; (b) after a contact pressure of ~ 932 MPa; (c) after ~ 785 MPa; and, (d) after ~ 687 MPa; note the occurrence of a decreasing pressure at greater blunting indicative of an ISE.[13,14]

1.2.1. *Hertz equations*

The Hertzian analysis provides a mechanics basis for the description of stress as the mean pressure acting on an indenter contact area and a definition of strain either relating to the indenter penetration depth or area of contact. The pressure required for elastic penetration of a ball indentation is given by:

$$P = (4/3)[\{(1-\nu^2)/E\}_B + \{(1-\nu^2)/E_S\}]^{-1}(D/2)^{1/2}h_e^{3/2}$$
$$= (4/3)E_r(D/2)^{1/2}h_e^{3/2}\,. \tag{1}$$

In Eq. (1), P is the applied load, the ν and E terms are for the ball and specimen, respectively, D is the ball diameter, E_r is the effective elastic modulus for the indentation and h_e is the depth of elastic displacement (see Fig. 14 for elastic nanoindentation of an alumina crystal). The indentation depth, h_e, is related to the contact diameter, d_e, by:

$$h_e = d_e^2/2D\,. \tag{2}$$

A cubic dependence of P on d was experimentally verified by Hertz[16] for elastic displacement measurements made by pressing a glass lens onto a flat glass plate. Thus, Eq. (1) may be written in terms of dependence on d_e as:

$$P = (1/3)(E_r/D)d_e^3\,. \tag{3}$$

Equation (3) is to be utilized later in describing the elastic, plastic and cracking behavior of silicon. The mean pressure achieved in elastic contact is:

$$\sigma_{\mathrm{He}} = P/(\pi d_e^2/4) = P/(\pi h_e D/2)\,. \tag{4}$$

The elastic hardness dependence on d_e and on h_e is thus obtained as:

$$\sigma_{\mathrm{He}} = (4/3\pi)E_r(d_e/D) = (4/3\pi)E_r(2h_e/D)^{1/2}\,. \tag{5}$$

The (d_e/D) dependence in Eq. (5) suggests itself as a convenient measure of the hardness strain

$$\varepsilon_H = (d/D)\,. \tag{6}$$

1.2.2. *The plastic hardness stress and hardness-determined cracking stress*

In similar manner to Eq. (4), the plastic hardness stress is specified as:

$$\sigma_{\mathrm{Hp}} = P/(\pi d_p^2/4)\,. \tag{7}$$

In Eq. (7), d_p is the surface-projected indentation diameter measured generally after unloading and is generally unchanged from the value under load as the unloading displacement for a fully plastic indentation is accounted for by raising and flattening of the bottom of the plastic indentation. For a rigid ball indentation,

$$d_p = 2[h_p(D-h_p)]^{1/2}\,. \tag{8}$$

Thus by substitution, the plastic hardness stress, σ_H, can be expressed as:

$$\sigma_{\mathrm{Hp}} = P/\pi[h_p(D - h_p)] \approx P/\pi h_p D\,. \tag{9}$$

For indentation-produced cracking, a fracture mechanics-based relationship for the load dependence on crack size of a radial, penny-shaped or median crack was obtained in a seminal analysis reported by Frank and Lawn.[20] One expression for the load dependence of cracking is expressed in Eq. (10) as:

$$P = (1/0.015)([d_C/d_V] - 1)^{1/2}(H/E_S)^{2/3}K_C d_C^{3/2} \approx (1/\chi_r)K_C d_c^{3/2}\,. \tag{10}$$

Equation (10) was developed by Laugier[21] for a radial crack of tip-to-tip length, d_C, at a diamond pyramid (Vickers) indentation of hardness, H, obtained for a residual plastic diagonal length, d_V, in a material with elastic modulus, E_S, and indentation fracture mechanics value, K_C. Elban *et al.*,[22] evaluated K_C for measurements made on sucrose crystals. Atkinson *et al.*,[23] have described the obtainment of K_C values for various crack geometries. Puttick *et al.*,[24] reported development of a plasticity-based median crack geometry somewhat similar to that reported by Atkinson *et al.* for indentation of a silicon crystal and with connection to updated fracture mechanics results on PMMA reported by Lach *et al.*[25] Lach *et al.* utilized the method of Laugier to determine indentation fracture mechanics toughness values in agreement with conventionally determined values. Atkinson *et al.* provide a discussion and appendices on comparison of Hueber's description of the Hertzian-type and Boussinesq (point loading[26]) analyses further developed by Lawn and co-workers for median crack initiations. In another analysis, Eq. (11) was developed by Lawn[27] for a linear elastic stress dependence on crack size as:

$$\sigma_C = [4E_S\gamma/\pi(1 - \nu_S^2)(\kappa_1^2 + \kappa_2^2)]^{1/2}d_c^{-1/2} = K_C[2/\pi(\kappa_1^2 + \kappa_2^2)^{1/2}]d_c^{-1/2}\,. \tag{11}$$

In Eq. (11), γ is the crack surface energy and $(\kappa_1^2 + \kappa_2^2)^{1/2} = 2.5 \times 10^{-5}$. Thus, Eq. (11) was reported as a Griffith-like elastic hardness-based cracking stress and will be employed in the following descriptions of a number of hardness-based stress–strain curves; see Figs. 7, 11 and 15. On an effective (d/D) basis for the hardness strain, Eq. (11) is modified to confirm the experimental observation of a lowered cracking stress for a larger ball diameter.

On the industrial side of practically specifying the plastic hardness properties of materials, Brinell[28] reported in a series of articles a hardness pressure that he defined as the load divided by the surface area of a spherically-shaped cap taken for the shape of a residual plastic indentation. Wahlberg[29] elaborated on Brinell's description. Walley has tracked these and other research accomplishments of the era in detail.[1] In a follow-up to Brinell, Meyer[30] provided in a series of articles a more simple description of specifying the hardness pressure by employing the projected surface diameter, d_p, of a plastic indentation. The same measure is given above for the elastic contact in Eq. (7) and is often usefully approximated in Eq. (9) by making use of Eq. (8). Ludwik[31] is often given credit too for connection of hardness pressure and the stress–strain properties of materials especially in relation

to describing the conventional plastic stress–strain relation in terms of a logarithmic strain dependence of the plastic flow stress. An important discussion of the hardness measurements that were being made at the time was given by Turner based on his own considerable experience with the topic.[32]

1.3. *Previous books, reviews, proceedings*

The hardness properties of materials as related to modern understanding were first written about in a number of books published after the beginning of the 20th century and in continuing publications until the present time.

1.3.1. *Books*

Table 1. Selected hardness books.

P. Ludwik, *Die Kegeldruckprobe, ein neues Verfahren zur Härtebestimmung von Materialen* (Julius Springer, Berlin, 1908).
V. Poeschl, *Die Härte der festen Koerper* (Theodor Steinkopf, Dresden, 1909).
G. E. Garrett, *The Mechanical Properties of Wood: Hardness* (Wiley, New York, 1921).
W. P. Doehmer, *Die Brinellsche Kugeldruckprobe und ihre praktische Anwendung bei der Werkstoffprüfung in Industriebetrieben* (Springer, Berlin, 1925).
H. O'Neill, *The Hardness of Metals and Its Measurement* (Chapman & Hall, London, 1934).
F. C. Lea, *Hardness of Metals* (Charles Griffin & Co. Ltd., London, UK, 1936).
H. A. Holz, *On Hardness of Metals and Metal Products* (Privately printed, NY, 1937).
W. Späth, *Physics and Technology of Hardness and Softness* (in German), (Springer, Berlin, 1940).
S. R. Williams, *Hardness and Hardness Measurements* (Amer. Soc. Met., Cleveland, OH, 1942).
E. B. Bergsman, *The Microhardness Tester* (Axel Lundqvist A. B., Stockholm, Sweden, 1945).
P. A. Rehbinder, L. A. Schreiner and K. F. Zhigach, *Hardness Reducers in Drilling: A Physico-Chemical Method of Facilitating the Mechanical Destruction of Rocks During Drilling* (Council for Scientific and Industrial Research, Melbourne, Australia, 1948).
V. E. Lysaght, *Indentation Hardness Testing* (Reinhold, NY, 1949).
D. Tabor, *The Hardness of Metals* (Clarendon Press, Oxford, 1951).
H. von Weingraber, *Technical Hardness Measurement (in German)* (Carl Hanser Verlag, Munich, 1952).
B. W. Mott, *Micro-indentation Hardness Testing* (Butterworths Sci. Publ., London, UK, 1957).
H. O'Neill, *Hardness Measurement of Metals and Alloys* (Chapman & Hall, London, UK, 1967).
V. E. Lysaght and A DeBellis, *Hardness Testing Handbook*, (American Chain and Cable Co., Inc., Detroit, 1969).
A. A. Ivan'ko, *Handbook of Hardness Data*, ed. G. V. Samsonov (Israel Program for Scientific Translations, Jerusalem, 1971).
J. H. Westbrook and H. Conrad (eds.), *The Science of Hardness Testing and Its Research Applications* (Amer. Soc. Met., Metals Park, OH, 1973).
K. L. Johnson, *Contact Mechanics* (Cambridge Univ. Press, UK, 1985).
P. Blau and B. Lawn (eds.), *Microindentation Techniques in Materials Science and Engineering* (ASTM STP 889) (Amer. Soc.Test. Mater., Philadelphia, PA 1986).
A. Syzmanski and J. M. Syzmanski, *Hardness Estimation of Minerals, Rocks and Ceramic Materials* (Elsevier B. V., NY, 1989).
I. J. McColm, *Ceramic Hardness* (Plenum Press, NY, 1990).

Table 1. *Continued*.

H. Chandler, *Hardness Testing* (Amer. Soc. Met., Metals Park, OH, 1999), p. 192.
F. J. Balta Calleja and S. Fakirov, *Microhardness of Polymers* (Cambridge Univ. Press, UK, 2000).
A. C. Fischer-Cripps, *Nanoindentation* (Springer, DE, 2004), p. 266.
A. C. Fischer-Cripps, *Introduction to Contact Mechanics* (Springer, DE, 2007), p. 226.
L. A. Galin, *Contact Mechanics* (Springer, Berlin, 2008).
J. J. Gilman, *Chemistry and Physics of Mechanical Hardness* (J. Wiley & Sons Inc., NY, 2009), p. 214.
K. Herrman, *Hardness Testing: Principles and Applictions* (Amer. Soc. Mat., Metals Park, OH, 2011), p. 289.
M. M. Chaudhri (ed.) *Mechanical Behaviour of Materials* (Trans. Tech. Publ., Zurich, Switzerland, 2011).

1.3.2. *Reviews/proceedings*

The following lists a number of relatively current reviews and proceedings.

Table 2. Selected hardness reviews/proceedings

M. M. Chaudhri and Y. Enomoto, "First Intern. Indentation Workshop: Cavendish Laboratory, University of Cambridge, UK", *Philos. Mag. A* **74**(5), 1059–1346 (1996).
M. M. Chaudhri and Y. Y. Lim, Second Intern. Indentation Workshop: Cavendish Laboratory, University of Cambridge, *Philos. Mag. A* **82**(10), 1807–1809 (2002).
Special Focus Issue: Fundamentals and Applications of Instrumented Indentation in Multidisciplinary Research, *MRS Bull.*, **19**(1), 931–934 (2004).
M. M. Chaudhri, Dislocations and Indentations, in *Dislocations in Solids*, Vol. 12, eds. F. R. N. Nabarro and J. P. Hirth (Elsevier B.V., Oxford, UK, 2004), pp. 447–550.
N. K. Mukhopadhyay and P. Paufler, Micro- and nanoindentation techniques for mechanical characterization of materials, *Int. Mater. Rev.* **51**(4), 209–245 (2006).
E. Le Bourhis, D. J. Morris, M. L. Oyen, R. Schwaiger and T. Staedler (eds.), *Fundamentals of Nanoindentation and Tribology IV* (Mater. Res. Soc., Warrendale, PA, 2008). *Proc.* **1049**.
M. M. Chaudhri and Y. Y. Lim, Cluster Issue on Indentation, *J. Phys. D: Appl. Phys.* **41**(7), 074001–074029 (2008).
Special Focus Issue: Indentation Methods in Advanced Materials Research, *MRS Bull.*, **34**(3), 134–138 (2009).
N. H. Faisal, R. Ahmed and R. L. Reuben, Indentation testing and its acoustic emission response: Applications and emerging trends, *Int. Mater. Rev.*, **56**(2), 98–142 (2011).
R. W. Armstrong, D. F. Bahr, N. N. Thadhani and S. M. Walley (eds.), Hardness across the multi-scales of structure and loading rate, *Mater. Sci. Tech.* **30**(9–10), 1023–1206 (2012).

A list is provided in the Appendix of research articles additional to those directly commented-on in the text and is presented in the same order of topics and subtopics.

2. Stress–Strain Behavior

In many early researches, hardness measurements were made in association with separate determinations of force — elongation or compression curves leading to the development of now-conventional hardness-based stress–strain curves.

2.1. *Connection to compression/tension testing*

A natural outcome of the combination of the many experimental results reported on tensile testing as compared with hardness testing of metals and alloys leading up to the first half of the 20th century was to investigate the relation between the results obtained from the two testing procedures. Interest in the two property measurements were not far apart in time. Examples of earlier researches leading to a description of stress–strain results were given by Ewing[33] and by Unwin,[34] in the latter case drawing attention to the distinction between gradual onset of plasticity for face-centered cubic (fcc) copper as compared with a pronounced yield point behavior for body-centered cubic (bcc) mild steel, Unwin followed this referenced report with an article on development of a new indentation test.[35] Then later, several significant advances in understanding the nature of the plastic hardness property and its connection with the unidirectional stress–strain properties of metals began anew with the researches of Bishop *et al.*,[36] to be followed by Tabor[37,38] and by Krupkowski and Truszkowski.[39]

An early result included in Tabor's 1948 article[37] is shown in Fig. 4 that is credited to a 1931 report by Krupkowski. Note in the figure that the ordinate axis is expressed in terms of F/d^2, perhaps in deference to Meyer's work, and also that a dashed line has been newly added near to the ordinate axis of the graph in accordance with the prediction of Eq. (5) for the Hertzian elastic loading dependence.

The agreement between the plastic hardness results obtained at different ball sizes and comparison of the shape of the hardness-based stress–strain curve with that observed in the tensile deformation of copper served to further justify taking (d/D) as a measure of the hardness strain, this also being consistent with Meyer's above-referenced articles reporting on hardness stress–strain results. The early work

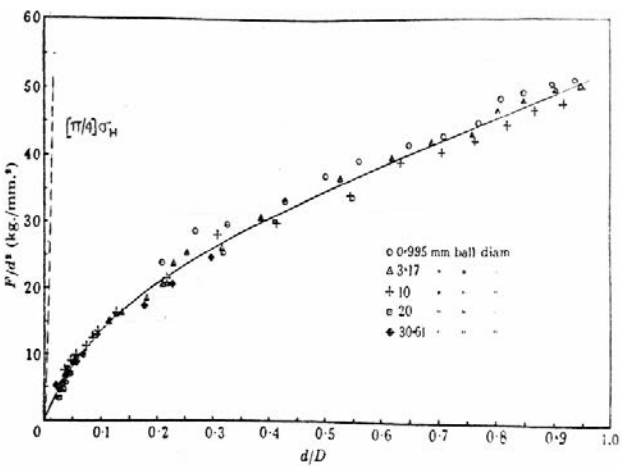

Fig. 4. Tabor compilation of steel ball indentations in copper, after Krupkowski.[37]

of Tabor and others preceding him led to the following relationship

$$\sigma_{\mathrm{Hp}} = C\sigma_{\varepsilon}\,. \tag{12}$$

In Eq. (12), the constant C was taken to be in the range of $2.8 \leq C \leq 3.0$, and σ_{ε} was taken as the ultimate tensile stress. The relationship between the tensile strain, ε, and the hardness strain, ε_H, was estimated as:

$$\varepsilon \approx (1/5)\varepsilon_H = (1/5)(d/D)\,. \tag{13}$$

Support for Tabor's description of the hardness stress–strain behavior was provided by Hill *et al.*, who re-examined on a continuum plasticity basis on the Brinell model for determining hardness.[40] Specific agreement was provided with Tabor's specification of $C = 2.8$ in Eq. (12) and for achieving comparable strain equivalence in Eq. (13). Such shift in plastic strain between the two testing procedures would bring the elastic and initial plastic stress–strain curves shown in Fig. 4 more nearly into agreement. Ishibashi and Shimoda reported also on the correlation of a spherically-determined hardness and the conventional material flow stress.[41] Other noteworthy investigations on the topic have been reported by Yan, Sun and Hodgson[42] and by Xu and Chen.[43] Hutchings has provided a recent review of Tabor's many contributions, with colleagues and students, to the science and practice of hardness testing.[44]

In Fig. 5, the steep line is the elastic loading line, $\sigma = E\varepsilon$, for the steel material tensile result and containing an inverted triangle point on the line for the maximum tensile stress elastically supported according to fit of the Hertz equation to the initial loading achieved with $D = 1.875$ mm for a hardened steel ball. The plastic hardness measurements, σ_{Hp}, were converted to plastic flow stress values, σ_{ε}, according to the relationship $\sigma_{\varepsilon} = \sigma_{\mathrm{Hp}}/2.8$. The two filled square points were obtained from the

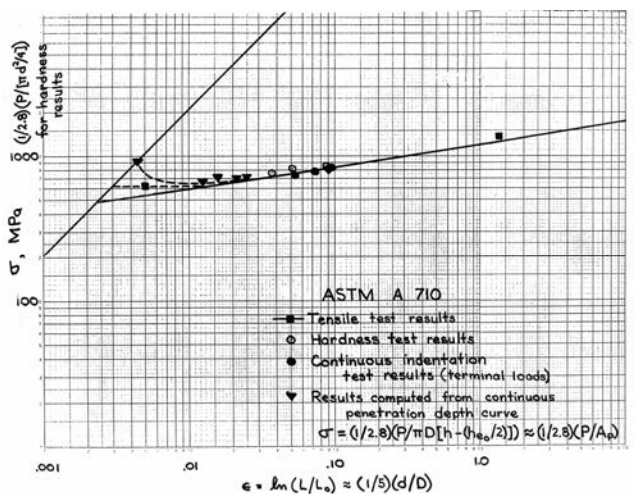

Fig. 5. Tensile stress–hardness comparison for ASTM A710 steel.[45]

tensile loading curve as an initial proof stress value and final true ductile fracture stress. The open circle measurements were obtained from individual (Rockwell) hardness test measurements. The remaining inverted triangle points were obtained from the terminal load values determined for individual continuous loading curve tests.

Connection also has been made between the temperature dependence of hardness measurements and a similar dependence for the flow stress of materials developed in pioneering work by Westbrook.[46] Gilman provides a succinct review on so-called "hot hardness".[47] There is relation by Gilman to work on the concentration dependence of hardness for halide crystals by Chin *et al.*,[48] and to the temperature dependence of the hardness of germanium and silicon. Recent measurements have been reported on silicon, also with determination of a high pressure transformation to a metallic phase whose presence was confirmed by Raman microanalysis.[49] The general consideration of a temperature dependence of the hardness connects also with influence of an indentation rate dependence that is treated here as a separate topic in Sec. 5, deformation rate effects.

2.2. *Direct determination of the hardness stress–strain curve*

The obtainment of continuous indentation loading curves led to the notion of directly measuring the hardness pressure of a material as a function of the elastic/plastic contact area that could be obtained as a function of the indentation depth.[50] Figure 6 shows a macro-scale continuous indentation loading result obtained on an NaCl crystal with a 6.35 mm steel ball and displacement measured autographically by crosshead movement while force was measured with a compres-

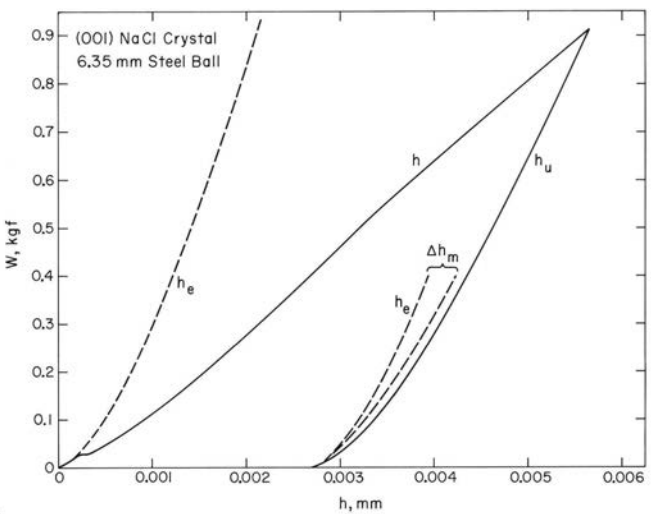

Fig. 6. Macroscopic loading curve for ball indentation in an (001) NaCl crystal surface.[51]

sion load cell mounted on a relatively stiff testing system.[51] On initial loading, the elastic displacement was measured to be in agreement with the Hertz prediction as indicated by the dashed h_e curve from Eq. (1), with $P = W$, and was followed by the type of "pop-in" plastic deformation to be shown later in the present article as being much more prominent in current nanoindentation test results. Shift of the dashed h_e curve to the unloading result in the figure showed that the unloading curve designated, h_u, when corrected for the machine compliance, Δh_m, followed closely the same Hertzian dependence. The effect was recently explained in terms of the negligible correction to the Hertzian behavior when only a small plastic strain, measured by (d/D), is produced in the indentation test.[52] In the present case, the maximum value of $(d/D) = \sim 0.06$. And from the elastic prediction in Eq. (4) and plastic prediction in Eq. (9), the respective hardness stresses can be seen in Fig. 6 to be gauged by the ordinate slope to each point of the loading curve. Thus for NaCl, the elastic hardness initially rises to a highest value at the onset of plasticity and then drops to a lowest value at the terminal pop-in displacement to be followed thereafter by an increase with further plastic straining. Such continuous loading/unloading curves as shown in Fig. 6 were reported for terminal load values of 100 MPa and 500 MPa. The unloading curves were steeper for the higher terminal loads. Similar measurements were made on KCl crystals. The alkali halide crystal work was followed by Robinson and Truman[53] who demonstrated application of the continuous indentation loading technique to produce a hardness-based stress–strain curve for aluminum material.

Figure 7 shows a compilation of hardness measurements, both obtained on a continuous loading basis for NaCl and for individual measurements for other crystal materials, all of which may be usefully compared on the framework of the proposed hardness stress–strain analysis.[54] The solid linear Hertzian dependence and follow on plastic stress–strain curve for NaCl is that determined from a result of the type shown in Fig. 6. The solid Hertzian line and other dashed ones shown in Fig. 7 were computed for a steel ball indenter. The terminal σ_C values shown for the dashed Hertzian curves were determined from Eq. (11) with employment of reported values of the cracking surface energy, γ. The value of σ_C for $D = 0.124$ mm on the Hertzian curve for MgO, as compared to the lower value shown for a 6.35 mm ball, is raised in accordance with expressing Eq. (11) on a (d/D) strain basis. The smaller D value was determined for the diamond pyramid hardness ball size equivalent on a Tabor basis to the diagonal indentation size shown for the MgO crystal measurements, also plotted at an equivalent 0.375 value of (d/D). The diamond pyramid hardness values are marked as VHN for Vickers hardness numbers in Fig. 7. As will be made clear for a number of experimental observations to be described in the present report, cracking at diamond pyramid hardness values frequently occurs at a lower hardness stress level than predicted for the Griffith-based indentation fracture mechanics stress of Eq. (11) because of the effect of stress concentrations at the tips of dislocation pile-ups, particularly, at slip band intersections. Such a

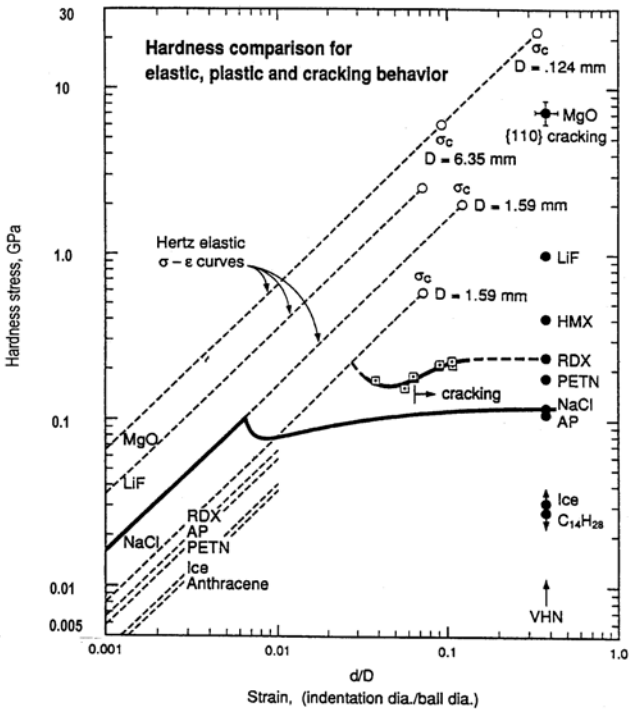

Fig. 7. Hardness stress–strain results.[54]

result applies in Fig. 7 for the post-plastic yield stress measurements shown for the explosive crystal, RDX. In addition, Fig. 7 gives indication for MgO of a relatively larger elastic strain contribution to the total plastic (d/D) value by virtue of the smaller separation of strain between the Hertzian elastic curve and the diamond pyramid hardness measurement, thus demonstrating the well-known observation that elastic recovery of the indentation shape is a relatively important consideration for harder crystals. Also, one might note the relatively greater brittleness of RDX compared to NaCl because of the smaller range between measured hardness and predicted cracking stresses. For RDX the indication is that there is little range in stress available for investigating any effect of deformation rate or temperature on the plastic deformation properties of the material.

2.3. *Metrology considerations*

The measurements provided thus far of the very significant range in load values applied to an indenter, say between 0.2 μN in Fig. 1 and 10 N in Fig. 6 (with 1.0 kgf = 9.81 N), give an indication that the main challenge of gaining an accurate evaluation of the hardness property comes not from measuring the load but from difficulty in determining the indentation contact dimensions during, or after, the hardness test.

2.3.1. *Indentation depth measurements*

In a pioneering hardness study of nickel, gold and silicon materials, Pethica *et al.* reported indentation depths as small as 20 nm as revealed in the electron microscope, including a continuous monitoring of the indenter penetration during loading and unloading.[55] There was a concern for the importance of the unassessed elastic strain during indentation. Nevertheless, the authors provided early quantitative measurements of an accompanying ISE that was associated with a higher plastic hardness being estimated for a smaller applied load coupled with smaller indentation size. The determination of higher hardness values at the smallest loads was attributed to very localized and enhanced strain hardening at the smaller indentations. An interesting observation was that small indents were able to be made in silicon without the material cracking.

An explanation of the ISE has been provided by Nix and Gao and leads to a predicted dependence of hardness on penetration depth of the form[56]:

$$\sigma_{\mathrm{Hp}} = \sigma_{\mathrm{Hp0}}[1 + (h * /h)]^{1/2} . \tag{14}$$

In Eq. (14), σ_{Hp0} is the extrapolated hardness at infinite depth and h^* is a characteristic length depending on the shape of the indenter, the shear modulus and σ_{Hp0}. Excellent agreement was demonstrated between Eq. (14) and experimental results reported from tests performed with a three-sided Berkovich indenter as applied to single crystals of copper and silver and to a work-hardened copper material. For hardness measurements at such nano-scale level, the connection between $h\ (= h_e + h_p)$ and the contact area of an indentation is of important concern. In a related investigation, Miyahara *et al.* have produced Fig. 8 showing connection between indentation depth and corresponding surface area.[57] As noted in the figure, the measurements were achieved with combination of a silicon tip AFM probe and

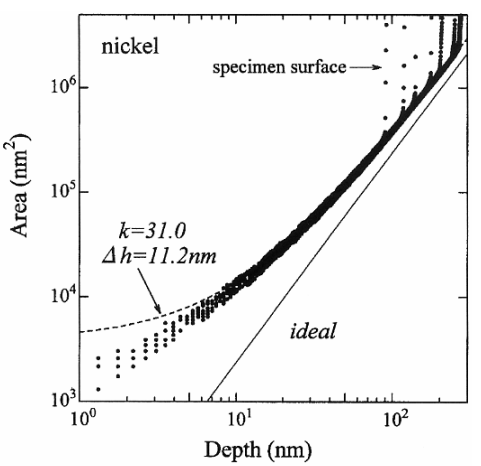

Fig. 8. Projected Berkovich surface area as a function of depth for $0.41 \leq P \leq 4.2$ mN.[57]

Berkovich (diamond) indenter but other materials were tested as well. The figure shows that the residual contact area was not reduced in direct relationship to the decrease in indentation depth and thus an ISE effect can be partly accounted for on such basis. The dashed curve shown in Fig. 8 was determined as a suitable area function to use in determining the material hardness. As will be described for other test results, particularly those involved in nanoindentation testing, the indenter tips are rounded in the same manner described by Hooke for his needle point when examined optically with a magnifying glass.

Another concern for the dimension scale at which interaction of an indenter tip and resultant specimen contact area occurs is shown in Fig. 9 for scanning probe microscopy results described by Coupeau *et al.* for a Berkovich indentation made under low-load condition in an MgO crystal surface.[58]

As shown in Fig. 9(d), Coupeau *et al.* produced a residual Berkovich indentation after loading to a total depth of $\sim$110 nm with indenter alignment along the [010] direction of one edge of the three-sided indentation. The total indentation depth was sufficient to produce the remnant three-sided impression shown in

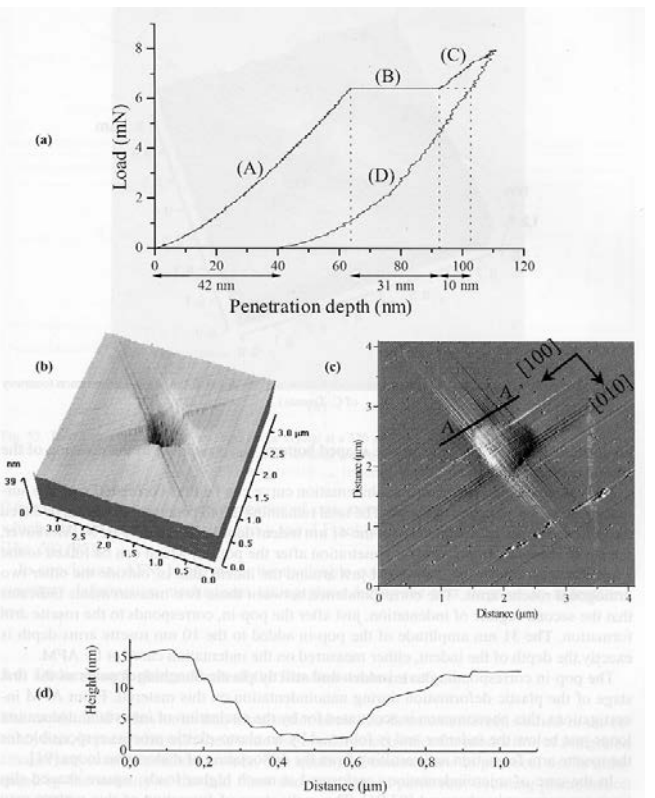

Fig. 9. (a)–(d) Loading curve, surface appearance and depth measurement for a Berkovich-tipped indentation in a (001) MgO crystal surface.[58]

Fig. 9(c). Equation (1) from Hertz was employed by Armstrong and Elban[59] to determine an indenter tip radius, $(D/2) = 1.6\ \mu$m, for the initial elastic loading curve in Fig. 9(a). Figure 9(b) gives indication of indentation-forming screw dislocation "troughs" spreading along the paired $(10-1)[-10-1]$ and $(-10-1)[10-1]$ slip systems set in juxtaposition along $\pm[010]$ directions and with $(01-1)[0-1-1]$ and $(0-1-1)[01-1]$ slip systems in the other orthogonal $\pm[100]$ directions. The measured residual indentation depth along one of the two troughs of ~ 14 nm, as indicated in Fig. 9(d), can be compared with one-half of the residual indentation depth of ~ 42 nm, thus the two trough depths, and tracked screw dislocation displacements account for a major part of the indentation strain. Such measurements will be related in the current report to an aligned diamond pyramid indentation result also produced for an (001) MgO crystal surface but at sufficient load to produce cracking. In that case, as well as the present one, it is important to appreciate that the elastic deformation, and its recovery, make an important contribution to the total deformation of indentations in MgO, consistent also with the hardness stress–strain measurements shown for MgO crystal hardness measurement in Fig. 7. Figure 10 shows quantitative assessments made by Shikimaka and Grabco of corresponding Berkovich and diamond pyramid (Vickers) indentations made in LiF and CaF_2 crystals including chemical etching of the dislocation "rosettes" and cracking observations.[60] The indentation-forming dislocation troughs pointed to in Fig. 9(c) are recognizable at the diamond pyramid indentation in Fig. 10(b).

Other aspects of indenter penetration depth relationship to tip radius[61] and bluntness of the indenter tip[62] have been described. In the latter case, a spherical

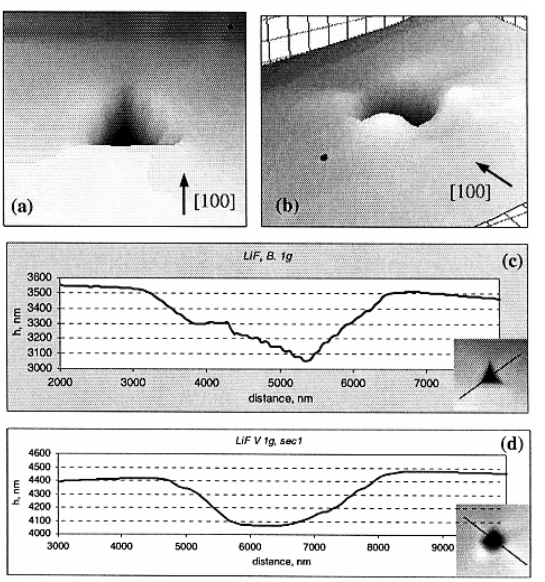

Fig. 10. LiF crystal 3-D images of Berkovich and diamond pyramid indentations at $P = 10$ mN.[60]

tip description was employed for relation to results obtained with a Berkovich indenter with a spherically-rounded tip applied to a fused silica glass and the load–penetration depth measurements were transformed to provide a stress–strain indentation curve. Berla *et al.*[63] have provided a two-parameter functional description of tip radius and equivalent cone slope for shape calibration of indenters. Observations have been reported of elastic–plastic contact area measurements made for copper and stainless steel spheres pressed against a flat transparent sapphire surface during loading–unloading tests.[64] Because of current concern for the direct imaging of indentations, Hou *et al.* provided a comparison of optical microcopy, metrological force microscopy and confocal laser scanning microscopy methods for quantifying surface shapes of indentations and plasticity length-scale effects.[65] Another investigation has focused on measurement of the indentation strain pattern via digital image correlation for surface strains somewhat interfered with by out-of-plane displacements.[66] Even at micro-scale indentation level, there is a concern for quantitative measurement of contact area because of pile-up or sinking-in around the indenter as described for *in-situ* measurements with a transparent spherical indenter applied to a relatively compliant polycarbonate material by Pelletier *et al.*[67] Additional discussion will be given on this issue in other results that follow.

2.3.2. *Advancements in hardness instrumentation/methods/techniques*

There are improvements in instrumentation being made even at the smallest dimensional scale relating to atomic force considerations as described in the introduction relating to Fig. 1. One improvement involves application of a "ferrule-top" optical system to cantilever design for a nanoindenter system.[68] Such design is proposed to extend AFM-based sensitivity to nanoindentation testing. A technique for AFM-based nanoindentation has been applied to measuring elastic and plastic aspects at nanometer dimensions of grafted and spin-coated glassy polymethylmethacrylate (PMMA) thin films.[69] The mechanical dynamics of the cantilever systems employed in such measuring systems have been investigated.[70] Contact of a nano-scale tip and substrate has been modeled for a half-spherical platinum tip contacting a same material substrate for AFM action avoiding plastic deformation.[71] A force feedback system has been employed[72] to evaluate tip-surface interaction with sensitivity of 1 pN; see comparison with Fig. 1. From determined knowledge of the lever spring constant, simultaneous measurement was provided of force, force gradient and damping properties of the system.

A number of optical-based instrumented indentation systems have been developed for the direct determination of indentation hardness values, particularly, involving employment of a harder spherical indenter.[73–75] And a number of test conditions have been investigated, such as: effective indenter radius and frame compliance[76]; effect of friction[77,78]; indenter misalignment relating to contact stiffnesses and Hertzian elastic prediction[79] and, surface roughness.[80–82] Interesting additions relating to metrological aspects of the hardness measurement systems

have been *in-situ* detections of acoustic emission[83] and Raman spectroscopy for phase transformation.[84] Cathodoluminescence measurements have been reported for gold sputter-coated nanoindentations in MgO crystals via an SEM fitted with a Cambridge S-180 cathodoluminescent measuring system.[85] Emphasis on indentation measurement aspects of hardness values have included length scale considerations,[86] low temperature testing,[87] quasi-nondestructive aspects of the test[88] and property measurements, including yield strength,[89] accelerated creep behavior,[90] viscoelasticity[91] and cavitation,[92] in the latter case spanning the gap between relevance of nano- and macro-hardness considerations.

2.4. *Nanoindentation testing*

In addition to the very important metrological advances directly associated with the advent of nanoindentation testing, there are a number of advantages relating to material properties that are able to be tested, for example: (1) an accurate method is provided for fully characterizing the elastic deformation behavior of crystals particularly during the initial loading behavior[52,59]; and, (2) the opportunity is provided to probe the elastic/plastic transition behavior at pop-in type conditions at a smaller dimensional scale than the separation of pre-existent dislocations.[93,94]

Figure 11 shows an early comparison made on a hardness stress–strain basis of nano-scale indentation measurements[95] obtained with a (fixed-shape) trigonal diamond-pointed indenter applied on a continuous loading basis to a polycrystalline copper standard hardness test block: NIST Standard Reference Material No. 1894. The NaCl crystal stress–strain curve is that same result shown in Fig. 7 as obtained with a 6.35 mm steel ball. The several filled-diamond and inverted triangle points

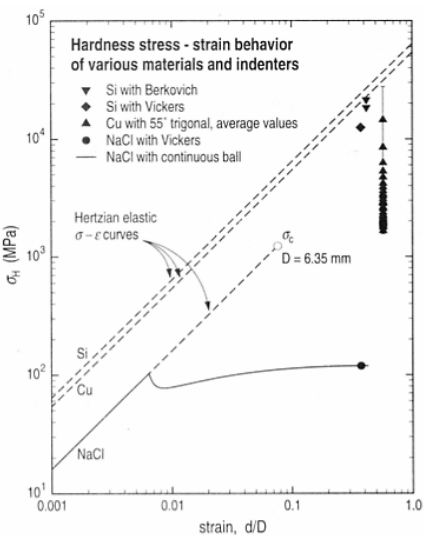

Fig. 11. Comparison of copper, silicon and NaCl results on a hardness stress–strain basis.[95]

for silicon crystal measurements are to be discussed in a later section of the current report. As noted, the dashed Hertzian curve for copper lies just below that shown for silicon. The vertical stack of filled-triangle points plotted at a Tabor-type fixed value of (d/D) were determined on the basis of a fixed depth dependence of the contact area, as described for Fig. 8.[57] The lowest hardness value of 1.67 GPa was calculated at a highest load point of 200 mN to be in reasonable agreement with separate determination of a diamond pyramid hardness of 1.14 GPa at 500 mN load. The highest hardness values shown in the figure were determined with lesser certainty at lower load values in line with the same type of ISE that was described above for the pioneering results of Pethica *et al.*[55] The highest hardness values were noted to approach the limiting Hertzian loading curve thus giving indication of comparable elastic and plastic strain values.

The results in Fig. 11 may be compared with somewhat similar nanohardness results reported by Lim and Chaudhri on polycrystalline annealed and work hardened oxygen-free copper materials.[96] In the latter case, a comparable range in load values of 1–100 mN was individually applied to a Berkovich indenter and accurate AFM measurements were made of the projected contact areas, including surface profile measurements for residual indentations obtained on both material conditions along one of the forward edge directions of the indentations. Significant elastic recovery could be recognized in the reported residual indentation shapes and was associated with either "piling-up" of material for the work-hardened case or "sinking-in" for the annealed case. From such actual area measurements then, a highest hardness value of only $\sim$1.8 GPa was reported for an ISE effect for the work-hardened material (compared to lowest $\sim$1.0 GPa value) and $\sim$1.2 GPa (compared to lowest $\sim$0.4 GPa) for the annealed case. Gerberich *et al.*[97] have added to the interpretations of higher hardness for shallow indentation depths less than several hundreds of nms by pointing to connection of the ISE and ratio of energy for a newly-created surface and plastic energy dissipation.

Basu and Barsoum[98] have reported excellent results on application of the hardness stress–strain method for characterizing the plastic deformation behavior of ZnO C-basal and A-prism crystal surfaces in spherically-tipped nanoindentation tests as shown in Fig. 12. A lower hardness-based yield stress was associated with basal slip for the prism surface. The yield point drop is of the same pop-in type indicated in the macro-scale continuous loading result for NaCl in Figs. 6 and 7, only much more pronounced in nanoindentation tests.[94] The advantage of gaining information on the strain dependence of the hardness stress with a spherical indenter is made clear in Fig. 12. The additional inset figure shows an anelastic character for the post-yield indentation behavior of the C-plane indented crystal.

Kalidindi and Pathak have proposed a modified technique for transforming the continuous load–displacement curves into effective hardness stress–strain curves based on taking into account the indenter loading–unloading behavior.[99] There is indication, for example, of a stiffer unloading dependence in Fig. 12. Armstrong and Elban[52] have discussed the issue, particularly, relating to the result obtained from

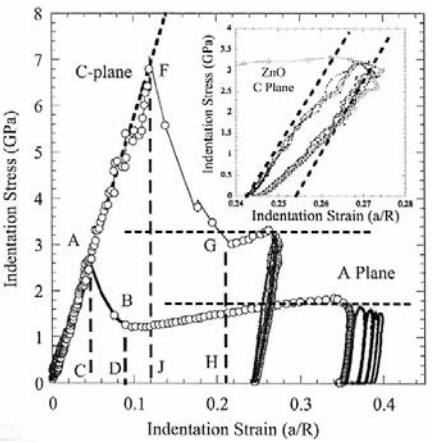

Fig. 12. Hardness stress–strain curves for ZnO crystal C (basal) and A (prism) plane orientations.[98]

the Hertz equations that the effective elastic modulus, E_r, is easily obtained from the initial loading curve in nanoindentation tests after "seating" of the indenter on the specimen surface at a small value of (d/D). Pathak, Shaffer and Kalidindi, in a follow-up report,[100] have provided comparative indentation stress–strain curves for tungsten and aluminum materials indented with two ball sizes. The issue will be revisited in the current report in the coming Sec. 3.1.1. Elastic loading results. For the present time, reference is made to work by Fischer–Cripps (see the book listings in Table 1) for providing example load-displacement curves[101] and to Bartier *et al.*[102] and Wei *et al.*[103] for further investigation of the contact radius associated with spherical indentations.

However, it is the obtainment of an improved understanding of the elastic–plastic "pop-in" transition that is of major interest in many nanoindentation experiments, as mentioned above.[93,94] In the latter reference, Bahr *et al.* employed the Hertzian–Hueber description of the elastic stress state below a spherically-tipped indenter to calculate, at the pop-in load level for a nickel crystal, a shear stress for dislocation nucleation approaching the perfect crystal theoretical limiting value. And subsequently in a number of articles,[104–107] Bahr and colleagues have investigated the influence of solid solution impurities, atomic vacancies, point defects and stacking fault tetrahedra on dislocation nucleation at nanoindentations. Tai-Gutelmacher *et al.* have looked at the effect of hydrogen.[108] Such nucleation consideration should be influenced naturally by the contact area dependence on the indenter radius for any applied load value, for example, relating to the macro- to nano-indentation D values and pop-in appearances spanning the hardness stress–strain results shown in Figs. 7 and 12. Poon *et al.*[109] have provided a mechanics analysis of such finite tip radius consideration by building onto the contact mechanics description originally developed for a sharp indenter tip with finite radius

by Sneddon[110]; see the relationship to Boussinesq description given above for an infinitely sharp tip[23,26] and Xu and Li[111] for connection of Sneddon and nanoindentation elastic–plastic behavior. The subject bears on the consideration of an essentially elastic unloading behavior after plastic yielding.

In two articles, one by Gao and Lou[112] and one by Lee *et al.*,[113] the nano-scale nucleation of dislocations under a wedge and matching of the small volume scales of contacted stress state and dislocation density have been modeled to provide a probability function for pop-in load characteristics. The pop-in stress is taken to be thermally-activated and so temperature and strain rate considerations are included. The model consideration of size scale is proposed to span the cases of homogeneous defect-free regions and heterogeneous mechanisms involving encompassed dislocation densities. Lodes *et al.*[114] have reported on connection of pop-in and ISE on dislocation density in CaF_2 single crystals in furtherance of earlier work with colleagues[115] also connecting with macroscopic hardness and use of a model description employing geometrically necessary dislocations.[116] A contribution to the physics of the nano-induced plasticity has been given recently in an interesting article by Fujikane *et al.*[117] Focus on the stress concentration to produce dislocation nucleation has been analyzed by Zhao *et al.*[118] in extension of previous work done with relation to cracking by Yan and Zhao.[119] A quantum mechanical description of solid solution effects on nucleation has been provided by Peng *et al.*[120]

Beyond the sensitive initial elastic loading behavior and pop-in type plastic yielding observations, the capability of nanoindentation testing is able to provide material strength measurements either not obtainable or not easily so by any other mechanical method. Thus, Huang *et al.*[121] have reported nanoindentation measurements made on tungsten microwhiskers significantly greater than for bulk material. Likewise, Daphalaparker *et al.*[122] while Zou and Yang have reported hardness results in excess of 100 GPa for individual sand particles, and Zou and Yang[123] have reported measurements for silica nanoparticles deposited on a single crystal silicon substrate. And for mechanical probing within the finer cellular structure of a material, Konnerth *et al*[124] have reported nanoindentation measurements obtained from wood. Reported measurements have ranged from such low hardness levels for wood and polypropylene[125] to nearly hardest results next to diamond of boron carbide[126] with in-between nanohardnesses of beta-tin,[127] indium and aluminum[128] and ZnO cone structures.[129]

3. Elastic, Plastic, Cracking Behaviors

As indicated thus far in the present report, an important outcome of interpreting the continuous loading deformation behavior during indentation testing over nano-, micro- and macro-scale behaviors was to provide a rather direct assessment of the elastic and plastic indentation deformation behaviors leading to a hardness-based stress–strain description. Beyond the early work described in Refs. 50–54, Rickerby and Macmillan produced continuous loading curves for spherical indentation of a

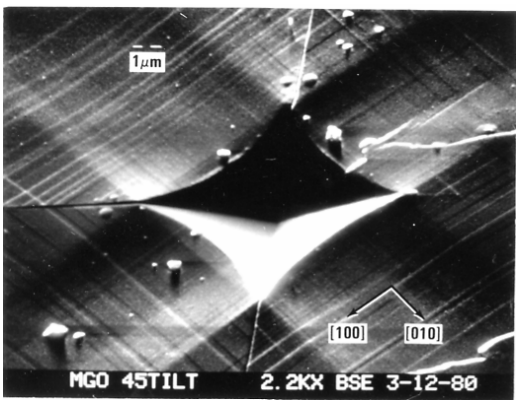

Fig. 13. Aligned diamond pyramid indentation on (001) MgO crystal surface.[132]

variety of materials including LiF, MgO and Ni crystals and with photographs of the resultant indentations.[130] Detailed optical, X-ray topographic and SEM photographs of [100] and [110] aligned micro-scale diamond pyramid indentations put into an (001) crystal surface had been reported by Armstrong and Wu,[131] including discovery of the downward displacements at "troughs" produced by the indentation-forming dislocations in screw orientation [see Figs. 9(a)–9(d)] and with sufficient load application to produce cleavage cracking on vertical {011} planes. In follow-up work, Hammond and Armstrong[132] produced the results shown in Fig. 13 for an indentation with diamond pyramid edges aligned along the respectively-marked ⟨100⟩ crystallographic directions. Details in the figure encompass considerations over the complete gamut of: (a) elastic recovery in the residual indentation depth and changed concave shape of the otherwise expectation of a square indentation pattern; (b) troughs produced by plastic flow of indentation-forming screw dislocations pushed away from the indenter tip as compared with volume-accommodating arrays of slip lines forming an apparent "picture frame" of indentation containment and (c) surface cracking made visible along traces of the indentation ⟨110⟩ directions by intersecting dislocation pile-up stress concentrations along internal ⟨111⟩ directions of the juxtaposed {110}⟨110⟩ slip systems not yet seen to be activated in Figs. 9(a) and 9(b). Feng and Nix[133]have investigated for MgO the ISE dependence predicted by Eq. (14). Significant deviation from the equation occurred for h values < 200 nm, most likely related to the different stages of dislocation involvements indicated between $h \approx 14$ nm in Fig. 9 and $h \approx 3$ μm in Fig. 13. Zong *et al.* have reported a bilinear ISE dependence for nano- as compared with micro-indentations made on (001) surfaces of nickel, gold and silver crystal surfaces.[134]

3.1. *Elasticity*

In the preceding description, the pioneering engineering mechanics analyses developed especially by Hertz,[16,17] Boussinesq,[26] Hueber,[18] Hencky[19] and Sneddon[110]

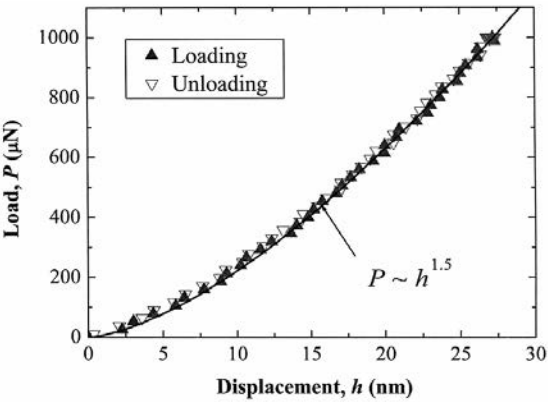

Fig. 14. Elastic loading/unloading of an α-Al_2O_3 (0001) crystal surface.[146]

have been referenced for contributing to a fundamental understanding of the elastic force–displacement relationship that develops during initial loading of an indenter pressed onto a contact surface.

3.1.1. *Elastic loading results*

Early elastic loading in a continuous indentation test led to determination of the elastic deformation behavior of compliant lignin material extracted from wood and to estimation of its elastic modulus, E_S.[135] Yoffe employed the loading curve in a re-examination of the Hertzian relation leading to a correction at larger displacements.[136] Useful elastic relations for other indenter shapes are also given by Yoffe. The preceding results relate to the elastic or viscoelastic indentation behaviors of other "softer" materials. For relatively compliant rubber-like materials, Liu *et al.* have described application of the Hertz equations to the load–displacement relation obtained for spherical indentation results at relatively small (d/D) values and make connection with Sneddon's solution.[137] A finite element description is developed for application up to $(h/D) \approx 0.4$. Chen *et al.* present a three-dimensional model for viscoelastic contact on polymer-based materials with modification of Hertz's E_r to be time-dependent.[138] And, Dokukin and Sokolov describe obtainment of bulk modulus (E_r) for polyurethane and polystyrene polymers with micrometer AFM tip probes with $D = 1.62$ μm, and 2.04 μm; measurements made with a $D = 44$ nm tip involved interference both from a "skin effect" and probe-surface adhesion.[139] Kindrachuk *et al.* report the obtainment of E_r values for LiF and KCl crystal surfaces with a blunted Berkovich indenter.[140] Other reports on the topic have included investigations of a piecewise description of elastic influence of indenter shape[141] and an effect of surface roughness.[142] Several reports have dealt with the general determination of Young's modulus and separation of Poisson's ratio in E_r.[143–145]

A direct nanoindentation measurement of the initial elastic loading/unloading behavior of an α-Al_2O_3 basal (0001) single crystal surface is shown in Fig. 14, as obtained by Lu *et al.* also with indication given within the figure body of excellent fit to the Hertzian Eq. (1) elastic dependence.[146] The sapphire crystal result was obtained with a Berkovich indenter and rounded tip of estimated $D \approx 408$ nm. Pop-in displacements were obtained beginning at the larger load value of 1300 μN. Plastic hardness values were determined through employment of an area function (see Fig. 8 and Ref. 57) and shown to be in agreement with the predicted form of Eq. (14) from Nix and Gao.[56] A theoretical Hertzian shear stress of 28.2 GPa was estimated for the pop-in initiation of plasticity. In relation to the plasticity observations made by Lu *et al.*, Lloyd[147] had previously identified, with the TEM applied to cross-sectional slices through nanoindented (0001) crystal surfaces of sapphire, operation of the three slip planes: basal, pyramidal $(-12-13)$ and prism (-1210). Results were also reported for spinel and magnesia crystals. In follow-up tandem articles on aspects of nanoindentation-induced plasticity in sapphire, Tymiak and Gerberich presented: first, scanning probe microscopy images of the surface indent topography revealed at spherical indents on basal, rhombohedral (-1012), and both prism (10–10) and (1–210) surfaces, and model analyses of them; and then secondly, load–displacement curves for various yield point-type pop-in behaviors.[148] The pop-in displacements were correlated with acoustic emission signals. And, most recently, Mao and Shen have reported on the pop-in characteristics of Berkovich-type nanoindentations put into sapphire rhombohedral (10–12) crystal surfaces, including estimation of the (10–11)[12–10] slip system being dominant and analysis of ISE measurements on Nix–Gao[56] and another basis.[149] Figure 15,

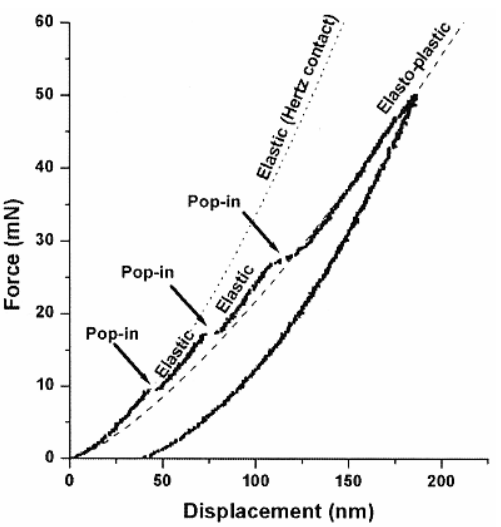

Fig. 15. Elastic–plastic nanoindentation loading curve for an (001) MgO crystal surface.[150]

from Gaillard *et al.* demonstrates for an nanoindentation of an (001) MgO crystal surface the sequential initial elastic loading behavior interrupted at several stages by plastic pop-in displacements.[150] The incipient plastic displacements produced by dislocation pile-ups contained within individual slip lines were monitored by application of chemomechanical polishing (CMP) for surface layer removal and of dislocation etching of the resultant indent. The nanoindentation result shown in Fig. 15 was obtained with application of a spherical diamond tip with $D = 20$ μm. In several experiments, the nanoindentation test was halted after individual pop-ins to demonstrate that each one was associated with nucleation of a new slip line structure. Quantitative measurements were reported for the number of dislocations in a slip line and the pile-up positions along the slip line commensurate with determinations from the loading curve of the Hertzian elastic contact radius just before first pop-in. Results from surface layers removals of up to 350 nm were reported.

Gaillard *et al.* indicate in Fig. 15 that elastic loading resumed after the first two pop-in displacements. Also, it may be noted that a total displacement of ~ 180 nm was achieved in this particular test thus corresponding to a total value of $(d/D) \approx 0.19$ (and consequent relatively low terminal hardness stress $\sigma_p \approx 4.5$ GPa; see Fig. 7 for comparison). Furthermore, it might be noted that the unloading curve from the terminal load value is not very much different in its displacement dependence from the Hertzian curve shown to be extended from the start of loading. The elastic loading and unloading comparison relates to an important method developed by Oliver and Pharr[151] of providing for determination of E_r from the top unloading part of a plastic loading curve after reaching the terminal loading value. The method was shown to give good results for fused silica, soda-lime glass and single crystal sapphire as well as aluminum, tungsten and quartz crystals. The procedure involves determination of a modified indentation depth to be used in conjunction with the indenter shape function to establish the contact area at terminal load. Miyahara *et al.*[57] have commented on such connection in relation to the contact area function shown here in Fig. 8. The issue also relates to Armstrong and Elban having pointed to the Hertzian prediction of the elastic load–displacement relation also depending on a radius of contact for the pre-indented contact surface; and, a reliable value of E_r being obtained from the initial loading curve if only a small pre-strain is applied to ensure proper contact of the indenter.[52] Ferranti *et al.*[152] have reported on a comparison of the two E_r determination methods at macro-scale dimensions for determining the lignan E_r described above[135] while also employing the Hertzian description for determining E_r values for fully dense and porous aluminum materials. Feng *et al.* have reported on a multiple partial unloading method for determining E_r in microindentation testing of steel, aluminum, bronze and single crystal superalloy materials.[153] Gao and Pharr have extended the Hertzian analysis to predict an elliptical contact area for an elastically anisotropic crystal and provided an example calculation for spherical indenter contact on a moderately anisotropic aluminium (110) crystal surface.[154] Other reports have been concerned, in one case,

with employing the method of Oliver and Pharr[151] to investigate the relationship between an indentation-determined elastic modulus and the corresponding material hardness,[155] or, in a second case, to investigate the connection between elastic and hardness anisotropies measured by Knoop hardness testing of iron pyrite single crystals.[156] As an example of practical application, Chromik *et al.* have reported determination of nanoindentation E_r and hardness measurements for lead-free solder and tin-based intermetallic materials, also with complementary AFM measurements of the residual indentation profiles.[157]

3.1.2. *Elastic/plastic rebound*

The separation of ball bearings into different bins according to how they bounced was tracked by Walley[1] to a 1917 report on quality control of manufactured steel bearings. The test relates to subsequent results of Tabor[37,38] and to a mid-20th century application by Vincent *et al.*[158] of comparing Hertzian prediction[159] for the elastic rebound mechanics of steel ball impacts and a time-dependent model description for the initiation of rate-dependent plasticity. For elastic rebound of a ball of reduced mass, $(m_B m_T/[m_B + m_T]) \approx m_B$ impacting a flat (target) surface of substantially greater mass, m_T, the Hertzian contact time, t, is given by:

$$t = 2.94(15 m_B g/16)^{-2/5}(D/2)^{-1/5} v^{-1/5}\,. \tag{15}$$

In Eq. (15), m_B is the mass of the ball, g is acceleration due to gravity, and v is the velocity on impact. Vincent *et al.* employed a comparison of contact t in Eq. (15) for first impact and a reduced contact time after multiple impacts, along with a dislocation mechanics-based plasticity analysis, to determine the dynamic yield stress of mild steel material. Initial and multiple impact tests were conducted in a controlled velocity apparatus with ball diameters of 40.8 mm and 70.6 mm diameter impacting at individual ball velocities within the range of 20–40 cm/s. The Hertzian prediction for initial contact durations was confirmed by comparison of results for the two ball sizes. The model plasticity description employed the Hertzian maximum value of shear stress at $(D/2)$ below the indenter and, with assumption of a spherical plastic impression being obtained after multiple impacts, led to prediction of a reduced time dependence on number of impacts.

Tirupataiah *et al.* described gravity-dropped ball impact results for Hertzian prediction of the coefficient of restitution, as rebound velocity divided by impact velocity, for a variety of metals and including assessment of cratering produced by plastic deformation.[160] A comparison was made of dynamic and static hardness values. Argatov and Fadin have reviewed the Hertzian elastic problem for spherical impact in connection with an extension to consideration of plate impacts.[161]

Wu *et al.* have investigated the effect of plastic deformation of a substrate on the rebound behavior of an elastic sphere by means of the finite element method employing the DYNA3D15 code.[162] Figure 16 illustrates the comparison with Hertzian prediction of the vertical contact force-displacement relationship at different impact

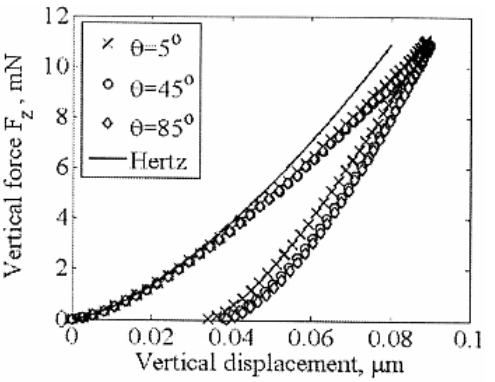

Fig. 16. FEM modeled elastic sphere impact on an elastic-perfectly plastic substrate.[162]

angles, θ from a vertical direction for a perfectly plastic substrate. A sphere of radius $(D/2) = 10$ μm was assumed and a constant normal velocity of 5 mm/s. Very interestingly, the comparison of the terminal Hertzian loading result and final unloading displacement shows that a major portion of the permanent deformation occurs during the rebounding action. Normal coefficients of restitution values were also obtained as a function of the ball contact time.

Clough *et al.* have reported comparison of high deformation rate dynamic hardness values obtained in dropped ball experiments and strength measurements obtained in conventional high rate tensile deformations.[163] The measurements were interpreted in terms of a dislocation mechanics-based constitutive relation employed for material dynamics calculations, not unlike the pioneering description employed by Vincent *et al.*[158] in their controlled velocity impact tests. Tirupataih and Sundararajan have reported on further investigation of the cratering aspects of dynamic impacts.[164] The topic has been reviewed by Sundararajan.[165]

For a condition of much greater deformation, the so-called "deep penetration" of a rigid sphere under hypervelocity impact conditions has been analyzed much earlier by Hanagud and Ross[166] in terms of a continuum plasticity description of a dynamically expanding cavity. The topic relates to modern constitutive equation applications to actual material deformations under extreme loading conditions as recently described by Murr,[167] including the use of hardness testing as a probe for correlation with changes in microstructure. For the case of more brittle material behavior, Chaudhri[168] has presented a review of his own researches on sequential high-speed imaging of indentation-type cracking initiated within a KCl crystal by impact of a tungsten carbide sphere at a velocity of 145 m/s. The associated plastic deformation was interpreted in terms of dislocation velocities reaching up to 700 m/s. Leavy *et al.*[169] have reported on spherical indentation experiments employed to characterize damage in ceramics, and particular results have been reported for silicon carbide material by Holmquist and Wereszczak.[170]

3.2. *Plasticity*

Beginning from the original work of Brinell[28,29] and others to use hardness determinations to assess the smallest amount of plasticity associated with brittle cracking of ceramic materials, and as indicated for many of the reports thus far referenced, there was a second thread of employing indentation hardness testing to investigate the crystallography of deformation systems beginning with optical microscope observations made on minerals and eventually extending to dislocation interpretations of plasticity.

3.2.1. *Slip, twinning, dislocation observations*

Interest in the abrasive hardness of minerals, for example, as associated with Mohs[171] in the 19th century, was rekindled in the 20th century by Schmid and Boas[172] in their book on crystal plasticity. Among the grand tabulations of crystal deformation and cleavage systems in the latter book were important references to Reis and Zimmermann[173] and Przibram[174] on the Brinell hardness of alkali halide crystals. Gilman took up the topic by correlating the hardness of alkali crystals and their ionic bonding[175] after having first tackled the bonding–structure relationships for metal–metalloid type carbides and refractory hard metals[176] crystals. Later attention was given to covalent bonding and the hardness of semiconductors[177]; see the listing for Gilman's book in Table 2. The difficulty of dislocation movement was especially considered in terms of atomic forces determining the crystal structure. Currently, specification of the hardness properties of crystals in relation to their operative dislocation-based slip and twinning systems and the consequent dislocation interactions is a main activity covering the complete range from softest to hardest material structures.

A number of reports have dealt with the hardness of diamond and superhard crystals,[178–180] including claims of dislocation movement at ambient temperature. There is always the question of having an indenter that is sufficiently hard or, alternatively, of investigating the indirect effect of deformation occurring both by the indenter and material being investigated, as mentioned above with respect to Refs. 14 and 15. In an investigation of the latter type concerning the hardness of diamond under high temperature–high pressure conditions, Brookes *et al.* obtained the image shown in Fig. 17 of slip bands in an (001) MgO crystal surface produced by a flattened copper cone.[181] The circular imprint of the flattened cone is marked by the segmented length of the slip bands. Note that the reported mean pressure given in the figure caption corresponds under the specified conditions to a hardness value of one-tenth of the average hardness value shown for ambient temperature measurements in the hardness stress–strain curve of Fig. 7.

Stokes *et al.*[182] reported early bend test results for MgO in which slip band development was initiated from dislocation sources put into the crystal surfaces. Other work by Stokes and colleagues had established by means of birefringence observations the importance of dislocation pile-ups forming at slip band intersec-

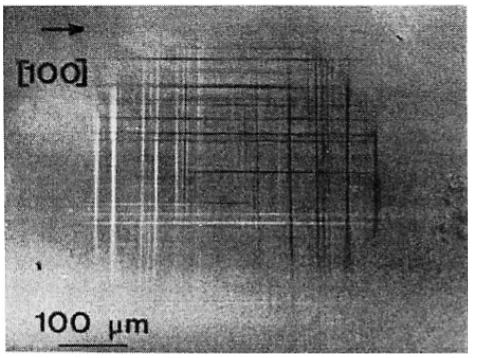

Fig. 17. Slip steps at an MgO (001) crystal surface indentation site produced at ambient temperature by a flattened copper cone subjected to a mean pressure of 700 MPa.[181]

tions and initiating cleavage cracks. Pande and Murty described {100} type slip band structures produced under dynamic indentation loading in NaCl crystals.[183] Gallagher *et al.*[184] reported on the observation of slip systems in PETN and RDX energetic crystals; see the representative hardness values from other measurements that are plotted in Fig. 7. A stereographic method of analysis applied to slip line patterns observed at diamond pyramid indentations in oxidizer ammonium perchlorate crystals was reported by Elban and Armstrong.[185] Nibur *et al.* reported on the use of surface observations of slip step structures around indentations in a procedure to analyze internal dislocation reactions.[186]

3.2.1.1. Dislocation rosettes

Chemical etch pits produced at points of emergence of dislocation lines on the surface of individual crystals have been an extremely valuable source of tracking dislocation mechanisms involved both in crystal growth and plastic deformation. Gilman reported on the chemical details of etch pit formation at dislocations in LiF.[187] In later deformation studies, Johnston and Gilman[188] investigated the stress dependent velocity of dislocations by employing ball impacts; (see also a review of the pioneering work in Ref. 189).

In the report by Stokes *et al.*,[182] dislocations had been introduced into the crystal surface by microscopic impacts from sprinkled carborundum particles. The reported "rosette" structures may be seen to be precursors of the now-familiar dislocation rosettes produced in many microhardness studies such as first reported for MgO by Keh[190] and for other alkali crystal results reported by Urusovskaya and Tyagaradzhan[191] and by Pariiskii.[192] In subsequent researches, indentation-produced rosettes have been investigated in metal, covalent and molecular crystals, for example: by Chen and Hendrickson[193] in silver at diamond pyramid indents under 0.2 mN load; by Hu[194] in silicon crystals at temperatures $\geq$ 673 K and at loads $\geq$ 20 mN; and in PETN and RDX molecular (energetic) crystals by Halfpenny

et al.[195] and also by Elban and Armstrong[196,197] in RDX at Knoop and diamond pyramid indents under loads ≥ 0.5 N sufficient to produce cracking; see the reference diamond pyramid hardness values plotted in Fig. 7. Punched-out dislocation rosettes at indentations in copper have been reported by Miura.[198] The effect of oxygen on dislocation locking in silicon was investigated by Harada and Sumino for rosettes produced in silicon at different temperatures,[199] thus relating to Westbrook's concern with the temperature dependence of hardness.[46] Nanoindentation rosettes have been reported for barium titanate crystals[200] and ZnO[201]; see in the latter case connection with reference.[98]

Study of dislocation rosettes in MgO and LiF crystals has been a particularly active topic of research extending over dimensional scales from those associated with optical microscopy and X-ray diffraction topography to SEM,[131,202] TEM[203] and AFM imaging.[204] Figure 18 shows a schematic diagram of the dislocation struc-

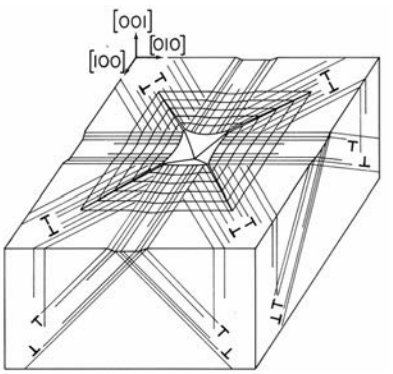

Fig. 18. Schematic dislocation structure at aligned MgO indentation.[131]

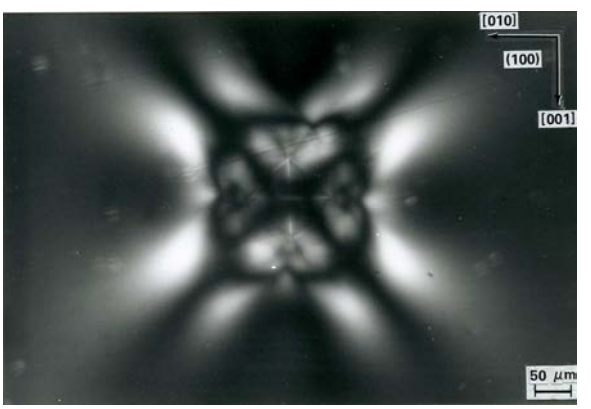

Fig. 19. Transmission optical photo with ⟨011⟩ axis polarizer of an aligned diamond pyramid indentation with edges along ⟨011⟩ directions in LiF (100) crystal surface[205]; see Ref. 131 for comparison with MgO ⟨001⟩ edges.

ture and induced cracking associated with the type of aligned diamond pyramid indentation shown for the MgO crystal surface in Fig. 13.[131] In Fig. 18,[131] the orientation of the aligned indentation and of the crystal-lattice-determined dislocation slip structures combine to produce the concave edges of the residual indentation, especially relating to the troughs along ⟨110⟩ directions produced by the indentation-forming dislocations emerging in a screw orientation on the (001) crystal surface.[200] The same orientation consideration was shown to change the shape of the indentation edges to a convex shape for an indentation rotated by 45° so as to produce side edges along ⟨110⟩ directions, as can be observed by close examination of Fig. 19 that is an optical transmission micrograph obtained with a beam polarizer for a LiF crystal.[205] The somewhat rounded edges of the indentation connect the central white cross formed in the figure by the indentation diagonals.

A hardness of 1.41 GPa was obtained for the LiF crystal shown in Fig. 19. The birefringent pattern shows contrast produced by greater light intensity being transmitted alongside the diagonal ⟨110⟩ directions perpendicular to the indentation side edges. Figure 18 shows that arrays of edge dislocations arranged in a dipole-like structure emerge along these directions. No influence on the transmitted light appears to be associated with the screw dislocation arrays aligned in the ±[001] and ±[010] directions. The substantial dilatation-associated edge dislocation contrast and consequent absent contrast for the screw dislocation arrays is in agreement with the previous work of Mendelson[206] on observation of birefringence in glide bands in NaCl single crystals being attributed to edge (and not screw) dislocations.

Gaillard *et al.* related the observation of dislocation rosette structures and the occurrence of pop-in behavior in the load–displacement curves of nanoindentations made on MgO and LiF crystals.[204,207] Slip step heights of 0.21 nm were measured.[204] Figure 20 shows A and B cases of rosettes obtained in an AFM tapping mode operation and corresponding pop-ins at load values of ∼0.13 mN and ∼0.4 mN measured with a Berkovich indenter, respectively[207]; see Ref. 58 and Fig. 9(a)–9(d). The elastic loading behavior was associated with the description for an axisymmetric indenter given by Sneddon.[208] The absence of evidence of dislocation slip activity along the ±⟨100⟩ directions is puzzling. Sufficient deformation was imposed to make visible the triangular impression of the Berkovich indenter but not in sufficient depth to activate the volume-accommodating dislocation slip bands that form the "picture frame" encasement shown schematically in Fig. 18. Other deformation curves were shown of unloading results obtained after different amounts of post-pop-in deformations. Discussion centered on the rosette pattern at B that was initiated at lower load but was pushed to further extent by the continued loading that is shown and was compared with the reverse situation of seemingly greater pop-in nucleation at higher load for A but without adding to the extension of the rosette pattern by further loading. Emphasis was given to a high and localized dislocation density being nucleated during pop-in and being formed within a small volume. Such observation relates to the description by Gane and Cox[13] for the ISE being associated with a highly localized volume of straining. Dong *et al.*

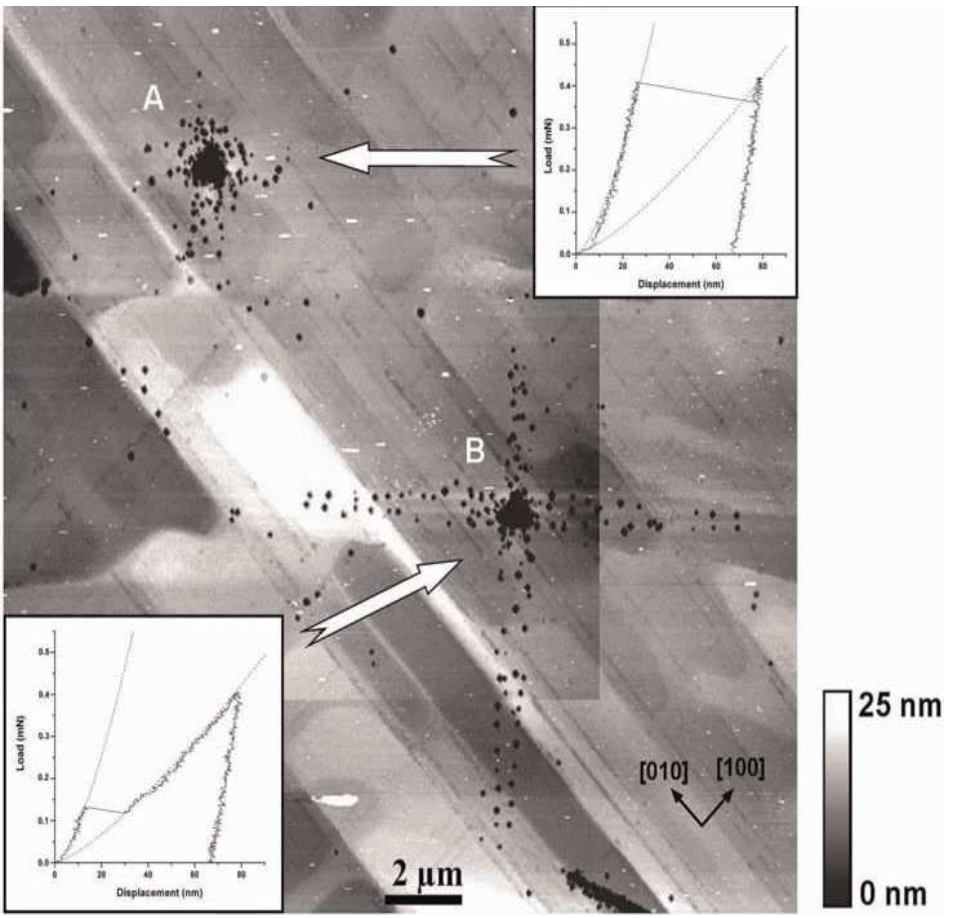

Fig. 20. Dislocation rosettes in LiF with associated nanoindentation pop-in curves.[207]

have investigated the nature of pop-in events occurring for nanoindentations made on both (001) and (110) crystal surfaces of MgO crystals and correlated the observations with Hertzian prediction of shear stresses and with acoustic emission measurements.[209] A greater shear stress was estimated for slip on the {100} planes as compared with the {110} planes. Savenko and Shchukin present an interesting comparative analysis of the separate lengths of etch pit extensions in ⟨100⟩ and ⟨110⟩ directions in NaCl and LiF crystals.[210]

3.2.1.2. X-ray diffraction (topography)

The observation via X-ray diffraction contrast of lattice strains produced by the residual dislocation structures at plastic indentations potentially provides an additional technique for deciphering the role of dislocations in effecting the hardness of crystals.[211] In particular, the back-reflection method, whether done by the

conventional Berg–Barrett method employing characteristic radiation or by the crystal-monochromated, asymmetric crystal topography (ACT) method,[212] affords insight into the generally more complicated nature of internal dislocation interactions determining the yield and strain hardening properties involved in determining crystal hardness values; see Ref. 131 for diffraction contrast produced at hardness indentations in an MgO crystal under different applied loads. Raghuram and Armstrong[213] matched the extent of etch pit rosettes and X-ray diffraction contrast at indentations on MgO. Yoo *et al.* extended the X-ray measurements to comparison of optical and X-ray diffraction patterns for indentations at macro-scale sizes.[214] Use of a synchrotron X-ray diffraction provides a very useful method of obtaining more accurate measurements faster.[215]

An interesting application of X-ray diffraction topography has been to investigate the hardness properties of energetic (explosive) crystals which are relatively brittle and otherwise decompose in the electron microscope.[216] The crystals are elastically compliant but relatively hard[197] as previously pointed-to in Fig. 7. Both diamond pyramid and Knoop hardness measurements were reported for crystal faces of RDX whose identifications were confirmed by X-ray diffraction.[217] Comparative etch pit rosettes and (Berg–Barrett) X-ray reflection topographs obtained for LiF and RDX led to explanation of the RDX crystal hardness being attributed to difficulty of dislocation movement through the intertwined molecular structure of the orthorhombic crystal lattice.[197,218] Halfpenny *et al.* have reported in a series of articles very complete crystal growth, (Lang) X-ray transmission topography and hardness resullts obtained on PETN crystals[195,219,220] and also to RDX crystals.[221,222]

Figure 21 shows application of the ACT reflection method to reveal the internal diffraction contrast at a central diamond pyramid indentation placed at 100 g load with vertical diagonal length along the [100] direction into a (1–10) copper crystal surface and with accompanying smaller indentations put at 5 g load into the strain

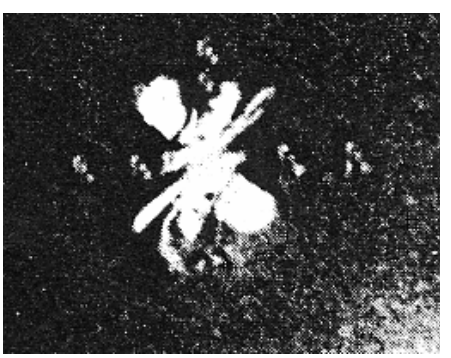

Fig. 21. X-ray diffraction (3–1–1) topograph of a central large diamond pyramid indentation with diagonal axis aligned along [110] on (1–10) copper crystal surface, and with smaller indentations in the [100] above and along the [110] horizontal centerline.[223]

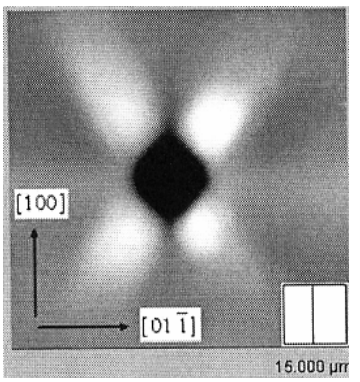

Fig. 22. AFM contour image of pile-up pattern at conical indent on (011) copper crystal surface.[224]

field of the larger indentation.[223] The complex geometry of white lobes centered on the indentation account for an absence of diffracted intensity. A stereographic method of analysis was employed to describe the physical diffraction geometry and to demonstrate a procedure for determining the crystal lattice rotations involved in producing such strain patterns. The more easily deciphered strain contrast was illustrated for the strain pattern of a Knoop indentation.

The X-ray diffraction contrast obtained from the internal strain pattern in Fig. 21 may be compared to some extent with the AFM surface profile measurement shown in Fig. 22 for a nanoindentation put into a same-oriented copper crystal; note the similar appearance of the two lobes along the $\pm$[1–11] directions.[224] Wang *et al.* obtained Fig. 22 for a conical indentation so as to place emphasis on the surface pattern measurement being solely determined by response from the crystal lattice. Simulated surface contour plots were also obtained to show reasonable agreement via mechanics modeling on a crystal slip plasticity basis and employing the FEM code MARC and HYPEL 2 subroutine 2. Good agreement was obtained for other AFM and modeled patterns of indented (001) and (111) crystal surfaces. Locally changed crystal texture measurements in the indents and in their surrounding regions were mapped by means of a high resolution electron back-scatter diffraction (EBSD) technique so as to follow the more-complicated slip system rotations, not unlike that involved experimentally in Fig. 21. The use of ESBD determinations for obtaining "orientation micrographs" at plastic indentation zones covering dimensions from 250 nm to 250 μm has been described by Rester *et al.*[225] Two-fold, three-fold and four-fold symmetry for respective nanoindentations on (011), (111) and (100) copper crystal surfaces were determined and experimentally simulated by Liu *et al.*[226]

Other X-ray usage has involved the very appreciable "time-saving" application of synchrotron radiation to obtain microdiffraction measurements of lattice rotations at indentations in single crystal copper,[227] relating to the ISE, and for

assessing nanoindentation determinations of residual stresses around micro-scale scratches scribed into aluminum alloy materials.[228]

3.2.1.3. Electron microscopy

A number of hardness results obtained with electron microscopy techniques have already been described. Beyond observation with the SEM of intimate tungsten indenter contact with the gold substrate is shown in Fig. 2, and such observation leading to quantitative sub-micrometer scale measurements of the ISE,[13] SEM application provided first detection of the downward surface troughs as shown in Fig. 13, thus leading to description of the indentation-forming screw dislocation patterns surrounding indentations in the (001) surfaces of MgO crystals.[131] The technique has been put to use for examination of dislocation rosettes at finer resolution than can be done with conventional optical microscopy. Valuable observations and quantitative measurements have been obtained at a finer dimensional scale with the scanning tunneling microscope in Ref 8 for nm-scale slip step heights at a nanoindentation in gold and for atomic force microscopy results illustrated in Fig. 9(a)–9(d) for a nanoindentation in an MgO (001) crystal surface,[58] including in the latter case, the mentioned troughs at the earliest stage of plastic deformation.

Chaudhri *et al.* obtained information on atomic color center activity at indentations in MgO crystals through the use of cathodoluminescence (and photoluminescence) measurements made at relatively low applied voltages in conjunction with SEM observations.[229] While strong luminescence was observed outside of the physical size of the residual indentation, a complete absence of effect was observed within the actual projected area of the indentation itself. The luminescence was attributed to the strain-induced creation of color centers at atomic defects. The effect was substantially quenched within the immediate confines of the indentations.[230,231]

The TEM was employed by Gane[14] to obtain the pioneering shadow micrographs shown in Fig. 3; otherwise, the technique has been employed for the principal purpose of observing dislocation structures produced at nano- and microindentations and quantifying the individual dislocation characteristics and arrangements, as reviewed by Chaudhri.[168] The observation by Humble and Hannik[179] of dislocations in ambient temperature indented diamond is an excellent example of expert TEM application. In general, the TEM has provided such observations in association with ultra-fine scale indentation loadings and the consequent deformations. An exception is provided by Chaudhri who points to the use of the TEM to investigate the relatively higher density dislocation structure immediately below an indentation. In silicon, TEM and selected area electron diffraction patterns were employed to investigate, in addition to dislocation initiations, whether the material had become amorphous and/or whether allotropic phase transformation had occurred. Minor *et al.* have presented evidence of room temperature dislocation plasticity in silicon using *in-situ* nanoindentation in the TEM.[232] The observation of dislocation plasticity was attributed to a special effect of free surface dislocation nucleation being

favored in their test system. Alternatively, Das *et al.*[233] report direct observation of amorphization of *p*-type silicon under an indentation by means of accompanying *in-situ* Raman spectroscopy measurements at $\sim$ 1 μm spatial resolution of the probing laser beam. Load-indentation depth curves were obtained under different low rate loading conditions, including pop-in observations and "pop-out" steps in the unloading curves. More recently, Chrobak *et al.* have explained the observation of dislocation plasticity on Hertzian-interpreted compression of Si nanospheres on the basis of a lesser constraint being provided by the smaller crystal sizes.[234] Hardness stress–strain curves were reported along with MD model calculations for confined (bulk-type) and unconfined (nanosphere) conditions. A two-times higher strength of $\sim$22.4 GPa was reported for the compressed nanoparticles controlled only by plasticity as compared with the lower strength plasticity of bulk silicon associated with its phase transition.

Other researches by Nowak *et al.*[235] have focused on an electrical spike measurement made during pop-in at the end of the elastic loading part of *in-situ* nanoindention experiments performed on GaAs crystals. The "mystery" of the measurements has been explained recently in terms of a simultaneous phase transformation from the zinc blende to rocksalt lattice structure.[236] Interatomic distance and bond angle measurements made during the experiment have been correlated with *ab initio* density functional model calculations of the indentation process.

3.2.1.4. Atomic force microscopy/Atomic modeling

Beyond the inventive relationship between the techniques of AFM for observing atomic-scale structure and development of instrumentation for nanoindentation hardness testing,[6–10] there are the direct applications of employing AFM observations in order to better understand material indentation properties; see Figs. 9, 10, 20 and 22. Earlier AFM observations had been made on MgO crystals relating to nanoindentation creep[237] and detection of plasticity on direct loading.[238] Gaillard *et al.* correlated plasticity observations with sub-surface dislocation positions that were revealed by chemical etching after removal of the nanoindented crystal surface layers in-depth by chemo-mechanical polishing.[239] An AFM investigation has been reported by Tall *et al.* of deformation twinning initiated at diamond pyramid indentations made at various temperatures in $LaAlO_3$ crystals, and especially for twinning occurring at the tips of cracks when subjected to sufficient applied load values.[240] Chromik *et al.* have described AFM results obtained on nanoindentations placed within individual grains of Pb-free solder and Sn-based intermetallic materials.[241]

The experimental AFM observations lend themselves to comparison with atomic-scale modeling, particularly at the dimensional scale of nanoindentations.[242] Thus, Szlufarska has reviewed MD simulation of nanoindentation load–depth curves obtained on SiC material, nickel indentation of gold, diamond pyramid indentation of Si_3N_4 material and MD and FE simulation of nanoindentations in copper. A number of atomic-scale images are contained in the article, including nanoinden-

tation probing of grain interiors and grain boundary effects in gold and in SiC. In coupling atomistics and discrete dislocation (CADD) plasticity modeling, Miller *et al.* have given emphasis to the same attractive size scale consideration of nanoindentation dimensions and simulated modeling of results.[243] At increasing depth below an indentation, their model development includes dislocation nucleation, dissociations, interactions, hardness size dependence, surface uplift, reverse plasticity, among other details. For the purpose of investigating deformation-induced "hot spot" development in energetic crystals, Chen *et al.* have provided MD simulations of temperatures generated in an RDX crystal when indented at nanoscale dimensions.[244] A comparable hardness of 391 MPa was obtained, somewhat greater than the average measurement shown for RDX in Fig. 7. Other simulations have been reported for alumina (ceramic)[245] and for polymer[246] materials, in the former case, involving very significant plastic anisotropy for indentations on different crystal faces, and in the latter case, relating indentation test results obtained on epoxy materials to their glass transition temperatures.

Both AFM nanoindentation experiments and modeling of results are particularly interesting for metals because of their exhibiting relatively high elastic stiffnesses and greater difficulty of nucleating dislocations that otherwise spread easily, thus leading to rapid elastic loading to a pop-in stress with substantial displacement. Figure 23 shows two load–displacement curves obtained at constant loading rate for a nickel (111) crystal surface.[94] One of the curves was reversed at 70–25 μN and reloaded to exhibit a lower pop-in load and reduced pop-in displacement; compare with the elastic and plastic displacements shown in Fig. 9(a). The comparison of curves shown in Fig. 23 demonstrated that a certain amount of plastic deformation could occur during otherwise essentially elastic loading, and that this should be taken into account in fitting to the Hertzian loading equation. Attention was

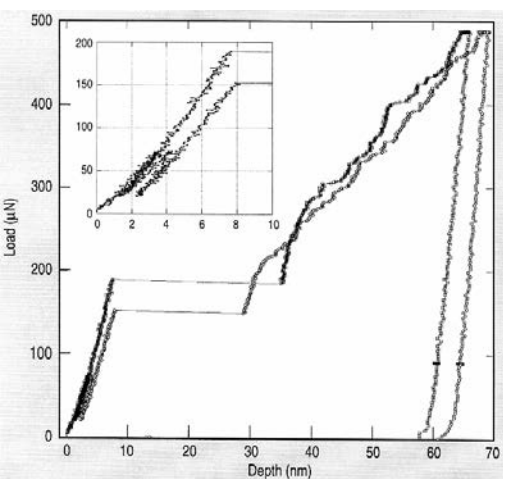

Fig. 23. Load–displacement curves for a (111) Ni crystal surface.[94]

directed to blunting of the indenter tip during repeated loadings and to other experimental and dislocation model considerations.[94]

Zhong and Zhu employed an interatomic potential in a finite element description of homogeneous nucleation of dislocations for (111), (110) and (100) crystal surfaces of aluminum, copper and nickel crystals.[247] Fang *et al.* reported MD results for aluminum. Also finding, as Zhong and Zhu had done, that nucleation, gliding and interaction involved Shockley partial dislocations.[248] Tsuru *et al.* also investigated the behavior of aluminum, in their case, with the embedded atom technique and produced simulated images accomplished with the visualization software ATOMEYE.[249] Emphasis was given to needed critical resolved shear stresses being higher than the theoretical shear strength because of the compressive stress state underneath the indenter. Their model load–displacement curves for aluminum show the same type of relative elastic and pop-in displacements as shown in Fig. 23.

As an example case for bcc metals, Alacala *et al.* have reported simulated dislocation structures at nanoindentations in tantalum crystals.[250] Figure 24 shows an early result of two dislocation loops spreading from underneath an impressed spherical indenter for incipient plasticity that nevertheless has involved rather complex pre-slip very fine scale twin nucleation and interaction plus annihilation to produce the loops. The leading edges of the loops are in edge orientation. Twin elimination has been attributed to reduction of stacking fault energy for twin layers thinner than four atomic layers and found to be enhanced at higher temperatures and decreased loading rates. Sectional views have been shown of the progressive development of dislocation loops and their interactions.

The cumulative dislocation-based mechanisms have led to the determination of load–displacement curves for (111), (011) and (001) crystal surfaces at the different temperatures of 296 K and 473 K while such results were simulated via MD at 77, 296, 473 and 900 K. The MD model description of dislocation nucleation, involving a combination of shear stresses and pressure under the rounded tip Berkovich indenter, proceeds onward from the single dislocation stacking faults and multiple atomic layer twins being nucleated and annihilated to form resultant slip-type dislocation loop structures that are shown in Fig. 24 to produce the results shown in

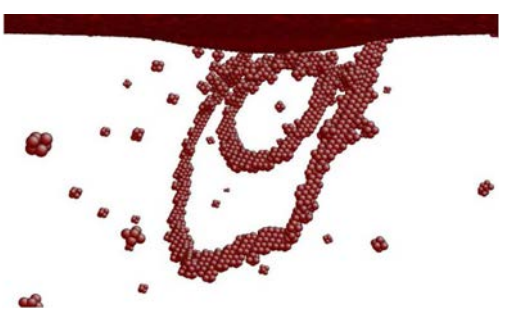

Fig. 24. Dislocation nucleation at an MD-modeled pop-in event in tantalum.[250]

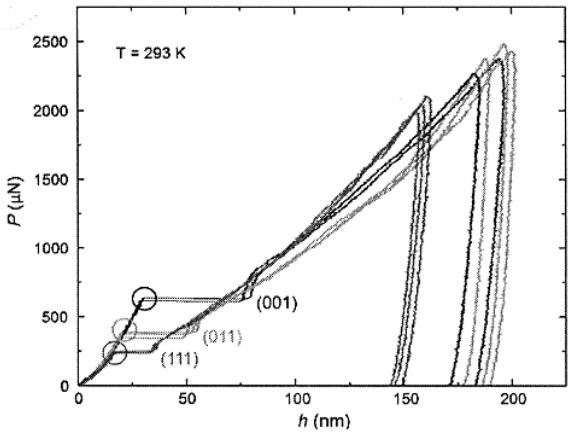

Fig. 25. Orientation dependent Berkovich indentations curves for tantalum.[250]

Fig. 25. Model descriptions based on indenter tip D values of 24 nm and 48 nm produce a similar trend of pop-in measurements to that shown experimentally in Fig. 25 with $D = 380$ nm. The current observation of the importance of a pressure effect in this bcc case is in agreement with the conclusion reached by Tsuru *et al.*[249] for their fcc case of aluminum.

Other aspects of atomic model computations have involved considerations of the relationship between hardness and atomic bond parameters,[251,252] in extension of early work by Gilman,[173–175] and to modeling the influence of indenter shape.[253] Particular aspects of atomic modeling have entered into practical considerations such as nanohardness aspects of steel surface treatments.[254] A quantum mechanical study of solid solution effects on nanohardness has been reported.[255] Microstructural aspects of nanotwinning on hardness have been assessed.[256] An advantage of strain gradient plasticity for simulation of microhardness has been presented,[257] as originally employed in the ISE model description developed by Nix and Gao.[56]

3.2.2. *Crystal hardness and plastic anisotropy*

After Knoop's development at the U.S. National Bureau of Standards of the exaggerated 7/1 length ratio for a diamond indenter shape for investigation of orientation-dependent plasticity measurements in metal and mineral systems,[258,259] Daniels and Dunn developed a remarkable geometrical analysis for explaining the orientation dependent anisotropy of hardness measurements in metal crystals.[260] The model description was based on achieving the critical resolved shear stress for particularly favorably oriented crystal slip systems. The topic of anisotropy brings together the subjects of crystal mechanics and continuum plasticity and involves results obtained, and continuing to be obtained, on all types of crystals and textured polycrystal and/or polyphase materials.

Brookes[261] produced an updated description of the Daniels and Dunn analysis with addition of a minor modification based on their own crystal anisotropy measurements. Armstrong and Raghuram[211] also re-examined the Daniels and Dunn analysis with conclusion that two orientation dependencies of crystal yielding and work hardening should be involved in determining the crystal hardness anisotropy. Evidence for such consideration was provided by Calder and Armstrong[262] in accounting in terms of increased work hardening for the greater Knoop anisotropies reported for aluminum, copper and nickel crystals, respectively.

Noteworthy assessments of different crystal hardness anisotropy measurements have been reported by Brookes,[263] and Sargent and Page.[264] Individual crystal anisotropy measurements and analyses have been obtained on many crystals, including the following: calcium fluoride[265]; calcium and sodium nitrate[266]; MgO[267]; LaB_6[268]; energetic (explosives)[269]; anthracene[270]; rare earth garnets[271]; magnesium sulphate hepta-hydrate[272]; gamma-TiAl[273] and, a nickel base superalloy.[274] A result from the latter reference is shown in the square-framed spherically-modified indentation of Fig. 26.

The indentation shape in Fig. 26 was accounted for in a finite element simulation that took into account the deformation gradient accompanying the indicated discrete slip band displacements. The overlap of surface pile-up/sink-in displacements was mainly attributed to the anisotropic crystal strain hardening property. Such a sink-in description presumably relates to screw dislocation activity of the type described for the special situation involved in accounting for the anisotropic shapes of [100] and [110] direction-aligned diamond pyramid indentation patterns observed on an (001) MgO crystal surface.[131] Further analysis related to Fig. 26 was presented in a follow-up detailed description of pyramidal indentations given by Eidel.[275] The over-riding influence of the geometry of the discrete crystal slip sys-

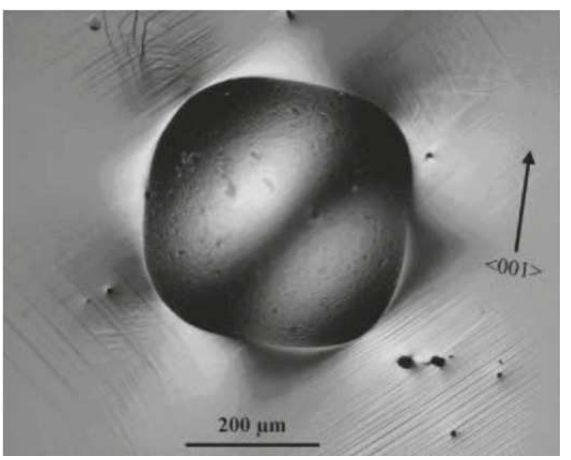

Fig. 26. Plastic anisotropy at a spherical indentation made on an fcc Ni-based superalloy CMSX-4 crystal (001) surface.[274,275]

tems was confirmed in the finite element simulation, and convex or concave shapes were confirmed depending on the relative orientation of the indenter and, again, emphasis was given to the importance of the crystal strain hardening property.

Additional concerns for hardness anisotropy occur for textured polycrystal or polyphase or composite materials. Thus the truncated spherical indentation shape of Fig. 26, that involves greater indentation displacement in ⟨110⟩ directions orthogonal to the easily-observed slip band traces relates to a similar observation and indentation spread along a direction perpendicular to aligned grain boundaries in an Al–Li 2090-T8E41 alloy[276]; see Ref. 52. Other related observations apply for anisotropy of indentations in a SiC-reinforced aluminum alloy[277] and a magnesium alloy.[278]

3.2.3. *Polycrystal/polyphase plasticity*

Hall proposed that the hardness dependence on polycrystalline grain diameter, ℓ, should follow a similar dependence to that observed for the yield point,[279] where dependence is now known as the Hall–Petch (H–P) relationship and is known to apply generally to the full tensile or compressive stress–strain behavior of polycrystals[280] as:

$$\sigma_\varepsilon = \sigma_{0\varepsilon} + k_\varepsilon \ell^{-1/2} . \tag{16}$$

In Eq. (16), σ_ε is the unidirectional flow stress at a constant value of strain, ε, and $\sigma_{0\varepsilon}$ and k_ε are experimental constants. Thus, the counterpart hardness dependence is expressed as:

$$\sigma_{\mathrm{H}} = \sigma_{\mathrm{H}0} + k_{\mathrm{H}} \ell^{-1/2} . \tag{17}$$

Comparative experimental evaluations of Eqs. (16) and (17) have generally assumed that $k_{\mathrm{H}} \approx 3k_\varepsilon$ and $\sigma_{\mathrm{H}0} \approx 3\sigma_{0\varepsilon}$ although there is a question about the appropriate value of $\sigma_{0\varepsilon}$ to be employed in the relationship.

Armstrong and Jindal[281] found historical evidence for the validity of Eq. (17) in a 1919 study by Bassett and Davis[282] describing Brinell hardness measurements obtained on two recrystallized cartridge brass materials over a range in grain sizes. The data are shown in Fig. 27 on an H–P basis in comparison with a parametric equation proposed in 1919 by Mathewson[283] and in comparison with other results on 70–30 α-brass reported more than 40 years later by Bassett and Rhines.[284] Much later, measurements made on the same basis of studying recrystallization, this time of α-titanium material by Cline and Hu,[285] were also shown by Armstrong and Jindal[286] to follow Eq. (17) over a very large range in grain size. Jindal and Gurland extended the H–P hardness relationship to include taking into account particle effects for tempered and spheroidized carbon steels.[287]

The grain size dependence of hardness for fcc metals, akin to the lesser grain size dependence observed for the conventional stress–strain behavior,[280] has been an active area of research. Lim and Chaudhri have reported on the nanohardness of high-purity copper and aluminum materials and concluded, from comparison with

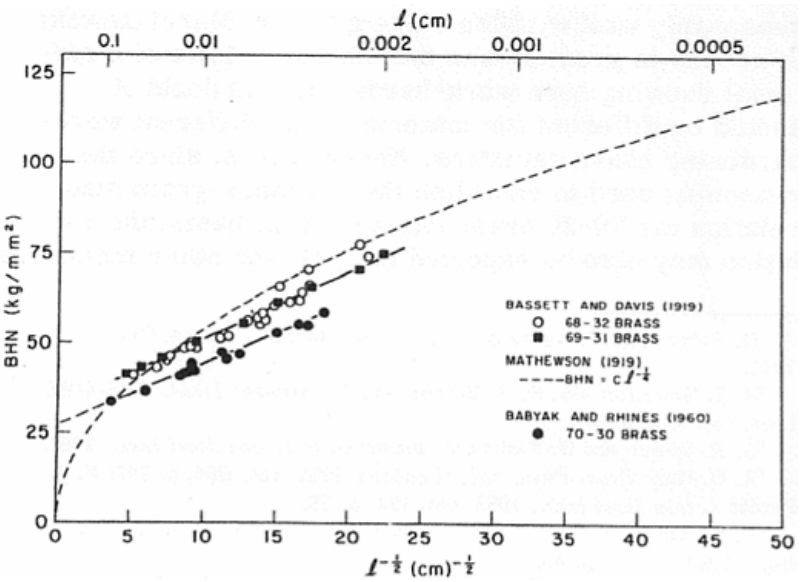

Fig. 27. H–P dependence for the hardness of α-brass.[281]

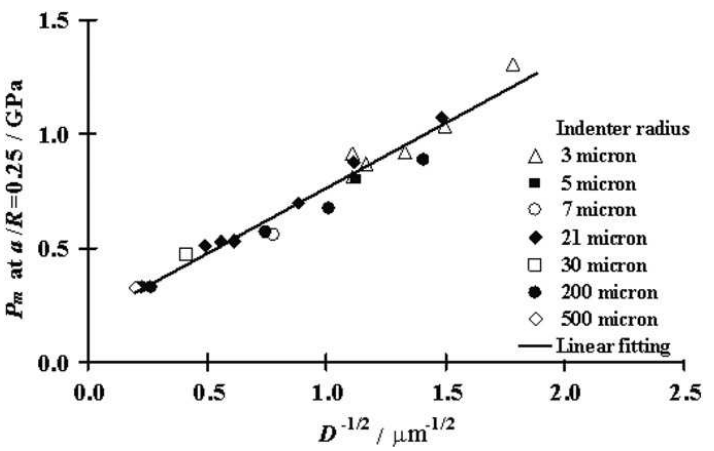

Fig. 28. H–P dependence for copper employing different ball sizes.[289]

single crystal values too, that the dislocation density was probably a more important factor in determining the behavior of purer material.[288] Lim and Chaudhri displayed their results on an effective stress–strain basis in line with Tabor's analysis.[38] In an important series of articles, Hou and colleagues have investigated the effect of spherical indentation size and H–P dependence for annealed copper polycrystals.[289–292] Figure 28 shows a result obtained with employment of different ball sizes applied to a large range in grain size in different materials.[289]

A principal concern for Hou and colleagues was to take proper account of an ISE at the different indentation size and grain size measurements. H–P behavior was verified for a ratio of grain diameter to projected diameter of contact area, d, less than a factor of 6. At larger ratios, the H–P dependence is observed to be superposed on the ISE. From the slope of the linear H–P dependence in Fig. 28, and taking $D = \ell$ in Eq. (17), $k_H \approx 18\ \mathrm{MPa} \cdot \mathrm{mm}^{1/2}$ and $k_H/3 = 6\ \mathrm{MPa} \cdot \mathrm{mm}^{1/2}$ in agreement with a reported $k_\varepsilon \approx 5\ \mathrm{MPa} \cdot \mathrm{mm}^{1/2}$ for copper unidirectional stress–strain behavior.[280,293] In Ref. 292, Hou and Jennett provide a simulation of combined ISE, H–P and dislocation density influences on determination of k_ε for copper. Konstantinidis and Aifantis have assessed the grain size dependence of hardness on a rule of mixtures approach for nanopolycrystalline metals and intermetallics in order to account for a reversal from H–P behavior at very small grain sizes.[294] The normal H–P division of strength into "grain volume" and "grain boundary" regions was also separated in the model analysis. Additional consideration was given to the presence of a grain boundary "width" and to the occurrence of grain "triple junctions" in accounting for the resultant properties.

Other researchers have directly measured the hardness near to or directly at the grain boundaries. Eliash *et al.* investigated the nanoindentation hardness of grain boundaries and their triple junctions in molybdenum tri-crystals.[295] An increased grain boundary hardness of $\sim 30\%$ was attributed to the boundaries being a barrier to nucleation of dislocation loops. Ohmura and Tsuzaki employed nanoindentation hardness testing on interstitial-free iron material to show that the grain boundary could initially be a source of dislocations and then subsequently act as a barrier to their motion.[296,297] Iron carbide films at the boundaries in a tempered Fe–C martensitic steel were shown to increase the H–P k value. Large pop-in displacements measured for the steel were associated with greater grain boundary hardness and analyzed in terms of the Hertzian description of stresses. Britton *et al.* measured the nanoindentation pop-in characteristics of grain boundaries in a Fe-0.01% C steel also to investigate the transfer of intragranular slip.[298] Such boundary-associated pop-ins were not observed for the cold-worked material nor for interstitial-free iron or for pure copper, thus leading to the conclusion that the (Cottrell–Bilby) mechanism of interstitial pinning of dislocations at or near the grain boundaries in steel was responsible for the H–P dependence as originally concluded by Hall and Petch. An effect of grain boundaries on the nanoindentation hardness of (bcc) iron, molybdenum, tungsten and tantalum materials was reported by Voyiadjis *et al.*[299] in a study employing a Berkovich indenter and a continuous stiffness measuring procedure, also including consideration of a strain gradient mechanism approach to evaluating the hardness on a simple power law basis.

The nanoindentation of fcc metals was also investigated in the same manner described for the bcc metals by Almasri and Voyiadjis, in this case, for silver, copper, aluminum, lead and nickel materials.[300] Qu and Zhou have reported atomistic MD simulations of twin boundary hardening measured by nanoindentations in copper.[301] Zhang *et al.* reported on the nanoindentation hardness of ultra-fine

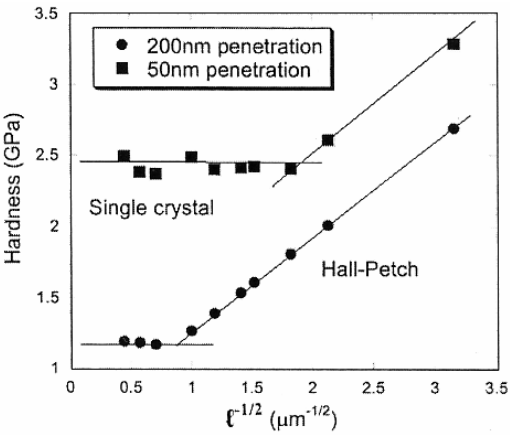

Fig. 29. Indentation size, crystal size, and H–P effect for copper.[306]

grain aluminum[302] which study may be contrasted in terms of hardness level and importance of the H–P grain size dependence with results reported on nanopolycrystalline diamond by Sumiya and Irifume[303] and by Gao.[304] And for a relatively hard material, smaller grain size association with greater hardness was reported in an evaluation of titanium nitride films produced by plasma nitriding on the surface of Ti-6Al-4V material.[305]

Figure 29 shows combination of ISE, H–P and specimen size aspects in an important investigation of nanoindentation measurements obtained by Bull *et al.* on submicrometer copper thin film materials.[306] First note the ISE-affected indentation depth influence on the levels of the hardness stresses. An increase of more than a factor of two occurs for the apparent hardness of an individual crystal (grain). The ISE was evaluated in line with the model proposed by Nix and Gao.[56] Secondly, there are the H–P dependencies shown at the smaller grain sizes leading to a $k_{\mathrm{H}} \approx 21\ \mathrm{MPa} \cdot \mathrm{mm}^{1/2}$; see Fig. 28 and the evaluation of $k_{\mathrm{H}} \approx 16\ \mathrm{MPa} \cdot \mathrm{mm}^{1/2}$, thus giving a result perhaps increased a bit by a continuation of ISE influence. And thirdly, there is the transition from individual crystal hardness to polycrystal hardness that Bull *et al.* associate with a need for 6–10 grains to be included within the plastic zone of the indentation in order to show H–P behavior. The effect is suggested to be analogous to the "specimen size" effect described for a tensile test in which ~ 20 grains through the thickness were proposed to be needed for measurement of a reliable H–P dependence.[307]

Lee and Gurland provided valuable extension to understanding the hardness properties of composite WC–Co materials by employing an H–P model description for the individual phase components in combination with a "rule of mixtures" relationship for the amount of each phase.[308] Thus, the relationship is obtained for the composite hardness, H_C

$$H_C = H_{\mathrm{WC}} V_{\mathrm{WC}} C + H_{\mathrm{Co}}(1 - V_{WC} C)\,. \tag{18}$$

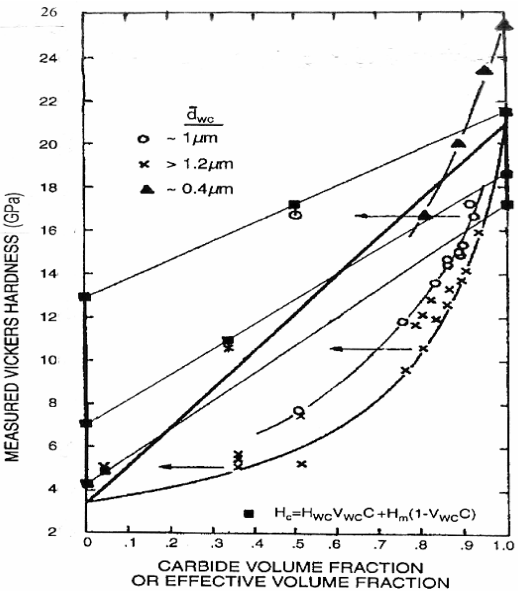

Fig. 30. Hardness of WC–Co composite with H–P dependences for the constituents.[309]

In Eq. (18), H_{WC} represents the WC phase and H_{Co} for the cobalt phase, each having their own H–P dependencies, V_{WC} is the volume fraction of the WC phase and C is the contiguity parameter to take into account the WC to WC particle contacts. Figure 30 shows the Lee and Gurland (open circle and cross) points that led to development of Eq. (18) and also includes a graphical method of assessing the relative contributions made by the H–P, C and V_{WC} factors in determining the overall hardness of the composite.[309] The figure includes added triangle measurements reported by Richter and von Ruthendorf.[310] Figure 30 was originally plotted by Lee and Gurland with only the open circle and cross points showing separate "rule of mixtures" dependencies on the carbide volume fractions obtained for the two particle sizes. In the current figure, three of those points, composed of two open circle ones and a cross one, have been shifted to an effective volume fraction value, $V^*_{WC} = CV_{WC}$, and matched with the linear dependence in Eq. (18) based on V_{WC}*and connecting to the H–P measurements plotted on the ordinate axis for each phase. The Lee–Gurland model relation seems to fit the experimental results quite well as may be compared with a semi-empirical description provided for the same and other hardness results analyzed by Makhele–Lekata *et al.*[311] A review of these results and other hard material results has been provided by Armstrong.[312]

Nanoindentation testing has been applied to a number of nanocomposite materials, for example, as described by Aldousiri *et al.*[313] for layered silicate-filled spent polyamide materials. Structural characterization was accomplished with application of XRD, TEM and SEM techniques in providing analysis for the improved

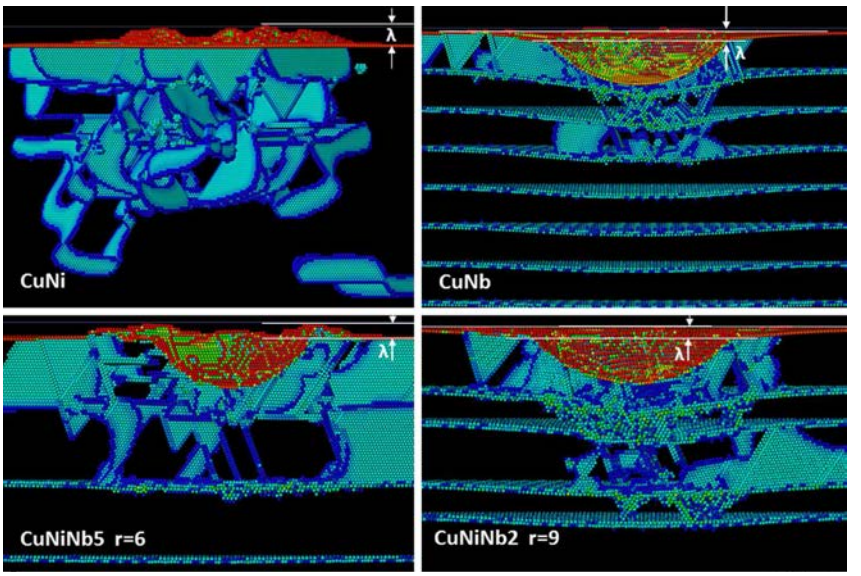

Fig. 31. Spherical indentation of multi-layers.[314]

nanohardness and moduli values that were achieved. Another example has been provided by Shao *et al.* on model development of spherical nanoindentations made on nano-scale multilayered metallic (NMM) composites of copper–nickel, copper–niobium and copper–nickel–niobium compositions.[314] Various single crystal layers of the different material combinations at nanometer thicknesses were constructed in the model system and indented with spheres also of nanometer diameters. Known orientation relationships were employed for the interface structures between the crystal layers. A power law relationship, using the Tabor relation for effective strain in Eq. (13), was employed to characterize the plastic stress–strain dependence that was monitored as it progressed through the stacked layers. Simulation of the load–depth dependence showed discrimination between piling-up, as for the copper–nickel case, versus sinking-in for the copper–niobium case. The dislocation densities generated in the different cases were also monitored and led to the qualified conclusion that the composite strength followed an inverse power law dependence on the layer spacing. Figure 31 shows some results for each of the four cases. The λ parameter marked in each inset snapshot measures the (CuNi) pile-up or (CuNb) sink-in and was utilized as a gauge against the plastic penetration depth. The lower left snapshot corresponds to a layers of 5 nm thickness indented with a sphere of radius $r = (D/2) = 6$ nm while the snapshot in the lower right corner involves 2 nm thick layers at the given r value. Partial dislocation Burgers vectors were identified at the initial stages of nucleation and were observed to form unit dislocations by various reactions.

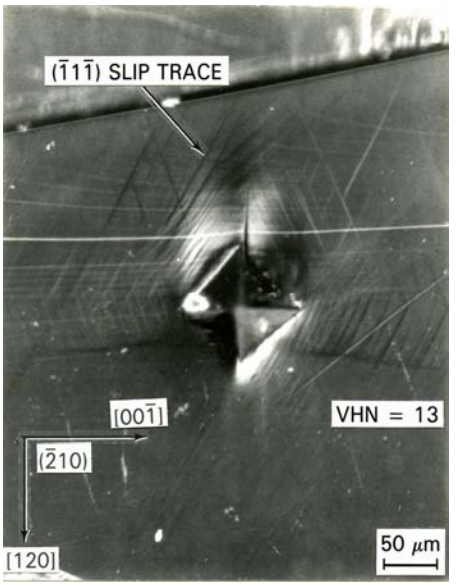

Fig. 32. Slip-initiated cracking at plane intersections in AP (ammonium perchlorate).[185]

3.3. *Cracking and indentation fracture mechanics*

Cracking at hardness indentations is of interest for reason of understanding the two aspects of how cracks are initiated by dislocation plasticity and how cracks propagate. Figure 32 is an AP crystal example.[185]

In Fig. 32, slip on intersecting {111} slip planes is clearly delineated and has produced a (−210) cleavage crack on the top-side of the aligned indentation. Additional plasticity was prompted by the crack initiation and so the top of the residual indentation is seen to be elongated in the [–1–20] direction. Such a result follows on from the early observation by Keh[190] of intersecting slip systems at indentations in MgO crystals and dislocation activity on them, for example, as described for the diamond pyramid indentation in Fig. 13. Keh *et al.*[315] developed a dislocation pile-up model for the {110} type cracking that is observed in MgO. And in a follow-up report, Chou *et al.* provided an evaluation of the intersecting slip band pile-up model on a dislocation mechanics basis.[316] Gaillard *et al.* provided a quantitative description of dislocation pile-ups produced at the indentations in MgO.[317] Armstrong and Elban presented a 3-D model description of the crack-forming dislocation interactions for an aligned diamond pyramid indentation.[318] Chaudhri has commented on the model considerations in light of his own experimental results obtained with a spherical indenter.[319] Related dislocation model results were presented for MgO[320] and for cubic zirconia[321] crystals.

The nucleation of cracks at dislocation pile-ups is dependent on the indentation size and hardness stress. Figure 33 shows a comparison of plasticity and predicted or

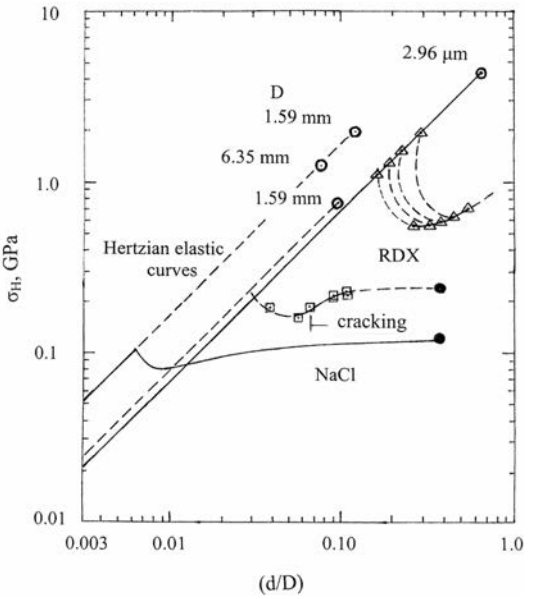

Fig. 33. Absent cracking in nanoindentation tests on RDX.[52]

observed cracking results determined for RDX and NaCl crystals.[52] First, consider the open square points obtained for an RDX crystal indented with a 1.59 mm diameter steel ball. The individual microhardness measurements demonstrated even for the relatively brittle RDX crystal that dislocation plasticity preceded cracking that, in turn, was initiated more easily than was predicted by the open circle point on the dashed elastic loading line. The terminal open circle point was calculated on the basis of Eq. (11) for the indentation fracture mechanics prediction of elastic loading proceeding directly to the hardness cracking stress.[27] The nearby solid line shown in Fig. 33 for RDX results reported by Ramos *et al.*, involving continuous loading of a rounded tip Berkovich indenter with $D = 2.96$ μm and different elastic modulus, was obtained for different surface treatments on a same RDX crystal surface.[320] No cracking occurred in analogous comparison of cracking being absent for MgO between the lower load case of Fig. 9(c) and higher load case of Fig. 13. In further comparison between the RDX and more ductile NaCl crystal result also obtained with a 1.59 mm diameter ball, such ductility for NaCl was explained in terms of slip occurring on {111} planes.[131]

Also in contrast to the old-time consideration that the occurrence of cracking at an indentation site would invalidate the hardness measurement, the development of indentation fracture mechanics by Frank and Lawn[20] has established connection with the Griffith theory for crack propagation in a gradient stress field, thus leading to characterization of crack surface energy and indentation fracture toughness stress intensity values, in the latter case, shown to agree with conventionally

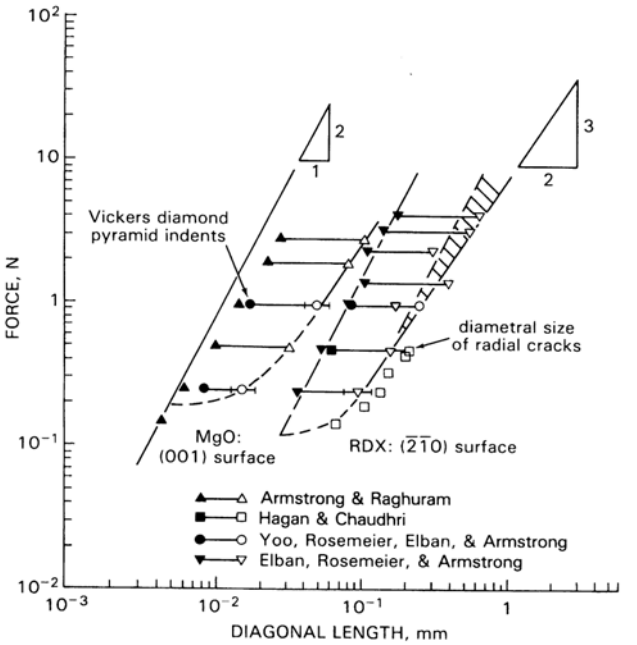

Fig. 34. Indentation size and crack size dependences for MgO and RDX.[325]

determined measurements.[310] Hagan and Chaudhri[321] used Eq. (10) to determine surface energy values for RDX that were shown by Elban[324] to be just larger than the thermodynamic value, thus giving indication of only a small plastic strain contribution to crack growth. The determination of the surface energy in Eq. (10) comes from the predicted (3/2) power of the slope of log P plotted versus the crack size. Figure 34 is a comparison of the load dependence of diamond pyramid indentation diagonal length and tip-to-tip crack length measurements made across the indenter diagonal directions, as compiled by Armstrong and Elban for microhardness indentations put into MgO and RDX crystal surfaces[325]; the Refs. 213, 323, 214 and 326 are included in the figure in order of their appearance.

The comparison of the quite different results for the two crystals in Fig. 34 shows that the cracking of MgO controls the hardness value whereas the reverse situation applies for RDX, that is, crack growth for RDX is apparently determined by the very small amount of plastic deformation occurring at the crack tip. Armstrong and Elban have related the results in Fig. 34 to other deformation characteristics of RDX.[327] Dong *et al.* have extended the study of (001) crystal indentations in MgO to observations made on {110} plane indentations.[328] Lin *et al.* have considered such measurements in relation to a brittle-to-ductile transition in behavior.[329] Yan and Zhou have looked into dislocation nucleation under a sharp tip indenter with regard to consideration of cracking.[330] And Thallidi *et al.* have looked into simulation of indentation fracture as a problem of mesoscale self-assembly.[331] Armstrong

has pointed to the relationship between the H–P grain size dependence and that originally ascribed to the Griffith analysis for an inverse square root of crack size dependence for the brittle fracture stress, thus leading to an H–P type dependence for the conventional and indentation fracture mechanics stress intensity.[332] Such dependence was found for indentation fracture mechanics measurements reported for the WC–Co system in Ref. 309 and in assessment of measurements reported for alumina materials.[333,334]

As for diamond, the issue of whether ambient temperature plasticity occurs during indentation of silicon crystals versus the alternative of an immediate onset of cracking is an important topic and with additional concern for the role of a phase transformation also occurring during indentation.[168] Apparently, the two behaviors are very close in terms of the required indentation stress. Atkinson *et al.*, in addition to assessing the indentation fracture mechanics aspects of the different indentation-related crack geometries,[23] performed their own measurements on silicon under a Berkovich nanoindenter. Direct observation with a focused ion beam system of a rather large well-defined residual nanoindentation created at ~ 110 mN was required to produce three median cracks extending from below the indentation tip to just past the surface-projected indenter diagonal lengths. Wan *et al.* have reported a finite element analysis of such cracking too on the radial, median, lateral and half-penny cracks.[335] Figure 35 shows an earlier compilation of results obtained on silicon

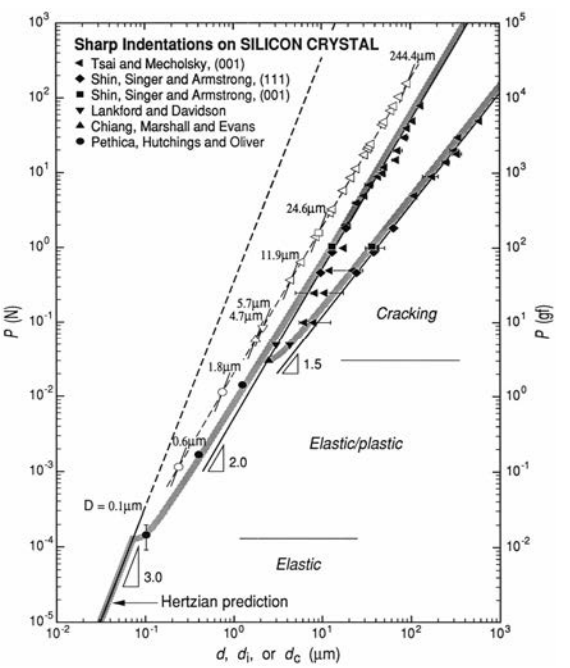

Fig. 35. Elastic, plastic, cracking load dependence for silicon.[336]

crystals by Armstrong *et al.* including their own measurements.[336] The log/log representation of the data includes a slope of 3 for the elastic behavior, 2 for the plastic hardness, and (3/2) for an indentation fracture mechanics dependence. The influence of the ISE is seen in the elastic/plastic regime and also carrying over to the low-load cracking behavior. As referenced above in connection with the pioneering ISE measurements in nanoindentations, cracking was absent in the results reported by Pethica *et al.*[55] Cracking was estimated to occur first at $\sim$30 mN, thus in reasonable agreement with the minor appearance of cracking at the higher load of $\sim$110 mN specified by Atkinson *et al.*[23] and with a $[\log P/\log c]$ type plot of diamond pyramid measurements obtained by Wan *et al.*[335] No obvious indication of any effect of phase transformation presents itself in Fig. 35.

However, in line with the above-referenced measurements reported by Minor *et al.*[232] and by Nowack *et al.*,[234] it seems reasonable that close availability of a free surface would favor easier dislocation nucleation over cracking or any need for transitional phase transformation to effect formation of a fully plastic indentation.

Sangwal has presented a review of ISE and cracking behaviors in relation to microhardness measurements obtained on brittle crystalline materials.[337] Yan and Zhao[338] have assessed the dislocation nucleation problem in connection with possible cracking behavior. Armstrong *et al.*[334] have considered further the elastic, plastic and cracking behaviors for especially hard crystalline materials. Relatively brittle aluminum oxynitride[339] and Cu_6Sn_5 intermetallic[340] materials have been investigated. Clough and Wadley obtained indentation fracture mechanics K_C values and acoustic emission measurements for the industrially important A533B nuclear pressure vessel steel.[341] Connection of hardness with cohesive energy of a material has been investigated by Roberts and Rowe for pharmaceutical compaction of crystals.[342] Also, there is very broad interest in indentation cracking behaviors associated with brittle glassy materials, for example, beginning with relationship of indent pre-cracks to the overall fracture behavior.[343]

4. Amorphous and Polymeric Materials

Two issues of major concern that emerge from hardness testing of amorphous materials are the increased local densification of the material at residual indentation sites and, separately, the nature of crack-initiated shear band structures accompanying permanent deformations. Yoshida *et al.*[344] have reported on the effect of indenter geometry on indentation-induced densification of soda-lime glass. And, Kato *et al.*[345] investigated densification under a diamond pyramid indenter for several glass materials in relation to their markedly different susceptibilities to crack initiation. The densification was measured via AFM examination before and after post-indentation annealing treatment. Early work on microhardness aspects of glass materials had been reported by Mackenzie, first with Neely,[346] and then with Yamane.[347] Hagan continued from the hardness report done with Chaudhri on RDX and PETN energetic crystals[323] with reports on the hardness of fused silica[348] and

soda-lime glass.[349] Another report on soda-lime glass by Gorham *et al.* describes the failure sequence observed on unloading.[350] Iwashita *et al.*[351] describe the indentation hysteresis for glassy carbon material. More recent test results have been reported, first by Smedskjaer *et al.*[352] and then by Smedskjaer *et al.*[353] with the aim of predicting hardness properties based on relation of the network topology as modified on the surface of the glass through diffusion of individual atomic species.

Comparison of crystal and metallic glass results has been investigated in nano-scale structural and test results and interpretations reported by Packard *et al.*[354] Perhaps surprisingly, these authors report smaller strain rate and temperature dependencies for the glass material tested far below its transition temperature. Computer modeled results are presented for a "nano-scale strength distribution" explanation of the nanoindentation measurements. As mentioned above, Torres-Torres *et al.*[62] have provided nanoindentation test results and FE simulation of them for fused silica material.

Yoo and Jang have obtained Fig. 36 in a macro-scale study of various stages of sub-surface shear banding achieved in spherical indentation tests of a split-specimen Zr-based metallic glass material.[355] Continuous loading curves were measured in obtaining the sectional views presented in Fig. 36. The sub-surface shear banding

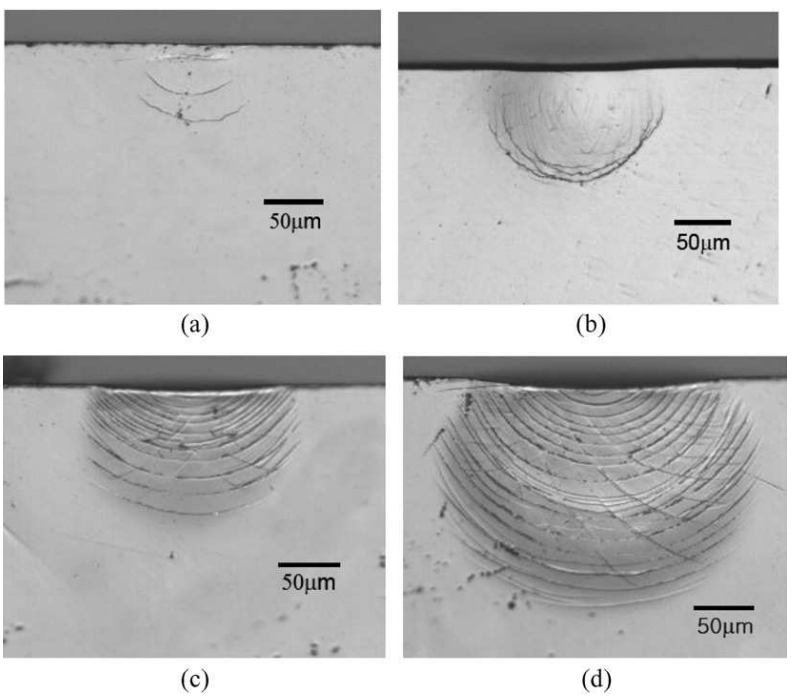

Fig. 36. Shear band structure observed on the post-bonded centerline interface of a Zr-based metallic glass at several stages of indentation with a WC sphere with $D = 1.0$ μm and applied loads of: (a) 19.6, (b) 49, (c) 98 and (d) 196 N.[355]

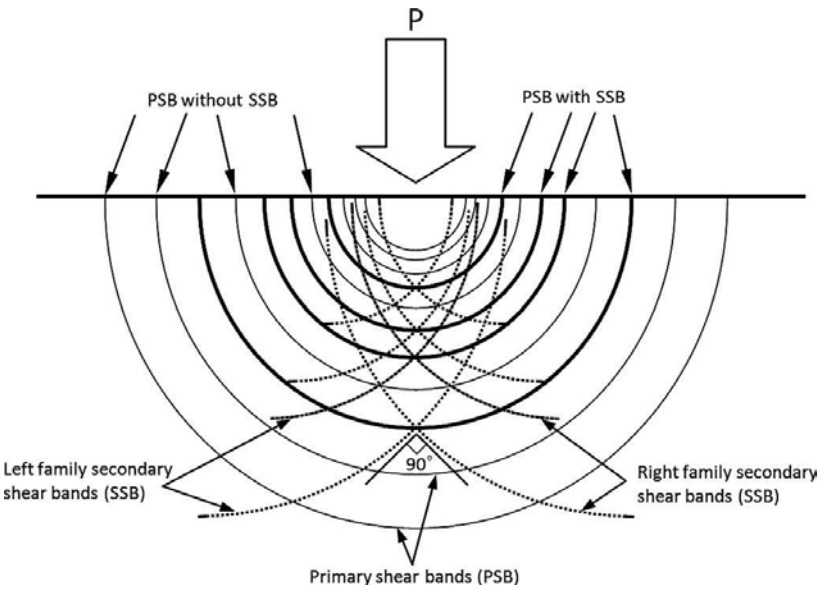

Fig. 37. Model description of primary and secondary shear band structures.[357]

morphology revealed in each sectional view was gently eliminated by polishing and then probed with a square pattern of nanoindentations spaced at ~ 25 μm separation and covering the deformed cross-section. The extent of the shear bands was analyzed on the basis of a Hertzian description. The deformed region was softer than the region outside of the deformation zone and attributed to the shear bands being softened. The softened shear band result was confirmed in a follow-up study by Yoo *et al.* including additional confirmation that the inter-shear-band regions were also softer.[356]

The results of Yoo *et al.* were analyzed in detail by Chen and Lin[357] in terms of primary and secondary shear band activity being basically responsible for the overall deformation response of the material. Figure 37 shows the schematically modeled pattern of primary and secondary shear bands. Chen and Lin present an instructive free-body diagram of the computer-simulated loading system applied to an elemental shear band annulus. The stress state consists of a hydrostatic core positioned immediately below the penetrating spherically-tipped indenter interfaced by an encompassing state of shear. Connection was made with the cavity expansion model of Johnson, see book listing in Table 1, and with slip-line field patterns developed in plasticity theory.[358] Characteristics of the primary and secondary shear bands, such as radii relationship, center positions, radii ratios, as well as the ratio of indentation radius to indenter diagonal length were enumerated. The Chen and Lin results relate to a description by Zhang *et al.*[359] of primary, secondary and tertiary shear band structures, also involving predictions obtained from modification of the expanding cavity analog.

Other reports on nanoindentation aspects of shear banding were reported by Greer *et al.* who also studied the behavior of partially devitrified material.[360] Pan *et al.* provided a correlation between measurements of structural relaxation obtained by annealing and reduction in size of the shear transformation zone accompanied by an increase in density.[361] Paduraru *et al.* modeled shear band formation of nanometer widths with atomic-scale simulations and drew comparison with simulation of dislocation avalanches in nanopolycrystalline material.[362] For the case of a sharp indenter, Conway and Kirchner related shearing behavior to the onset of fracturing.[363]

5. Deformation Rate Effects

The viscoelastic indentation behaviors of silicate glasses have been reported on by Sakai *et al.*[364] Misra *et al.* have dealt with plasticity aspects of rate-dependent serrated flow observed for a bulk metallic glass[365] and dynamic indentation deformation aspects of a chemically strengthened glass have been decribed by Jannotti *et al.*[366] An interesting approach in terms of interpretation of results has been reported by Liu *et al.*[367] They have utilized a "flow unit" model to describe anelastic and plastic deformations determined in the relaxation behavior of cyclic hysteresis measurements made on two metallic glass materials. The "flow unit" designation is remindful of the historical application made by Kauzmann of chemical reaction rate theory to the deformation rate dependence of plasticity in metals.[368] Armstrong and Walley have reviewed the subject as related to the high rate deformation behavior of metals.[369] An important parameter in the rate theory is the activation volume, v^*, that is determined from the product of Boltzmann's constant, the temperature and the logarithmic dependence of the strain rate on shear stress. Walley and Field[370] have reported extensive measurements for a number of polymeric materials of the dependence of stress on the natural logarithm of the strain rate. Chen *et al.* have investigated the viscoelastic behavior of polymer-based materials,[371] and relating to the preceding work in Ref. 79, Pelletier *et al.* have reported also rate effects and relaxation measurements for spherical indentation of glassy polymer materials.[372]

The foregoing references on rate dependence of hardness determinations for glassy ceramic and polymer materials give an indication of progress made from the early 20th century with metal deformations in mind, for example, involving the pendulum hardness test of Herbert[373] and reported time dependence of hardness measurements reported by Hargreaves[374]; see also Walley.[1] A particular interest in metals at the present time is to look into hardness testing for the purpose of developing constitutive relations for use in material dynamics calculations, particularly under dynamic loading conditions so as to relate to material penetrations; see Refs. 163–170. In addition to previous work mentioned above,[164,165] Sundararajan and Tirupataiah have produced a pair of articles on dynamic indentation loading and analysis of results.[375] Wu *et al.*[376] have presented an interesting application of such analysis to high-speed impact behavior exhibited by aluminum particles thrown onto a steel substrate in a coating operation, seen to be under less severe

condition of mass effect than that described by Murr[167] for penetration of copper by an aluminum sphere.

Almasri and Voyiadjis describe measurements for the strain rate dependence of hardness for a copper and a 1018 steel material.[377] Reference was made earlier to their article with Park on nanoindentation results for the bcc metals: iron, molybdenum, tungsten and tantalum.[299] Xu *et al.*[378] have characterized the strain rate sensitivity of polycrystalline copper in terms of v^* measurements determined in indentation relaxation experiments. Such measurements relate as well to creep deformation rate experiments at the other end of the strain rate deformation spectrum. A review of his own pioneering work on indentation creep had been given by Li with emphasis given to the ability of performing small-scale testing.[379] Choi *et al.*[380] have re-visited the topic. Shalaby has reported microhardness creep results on alloying of rapidly solidified tin-zinc solder materials[381]; see the nanoindentation results of Ref. 157. Somekawa and Mukai have reported on nanoindentation creep measurements made separately on grain interiors and at more strain rate sensitive grain boundaries in magnesium[382]; see Refs. 294–298. Yokouchi *et al.*[383] used repeated indentation testing of copper with spherical and cylindrical indenters and finite element modeling to characterize the deformation behavior. Basu *et al.* investigated the time-dependent nanoindentation hardness of ZnO (11–20) crystal surfaces.[384] A power law dependence was obtained for the time dependence of hardness and explained in terms of dislocation pile-up activity on the basal (0001) planes; see Fig. 12 and Ref. 98.

As indicated earlier for a KCl crystal, Chaudhri has given in his review of indentations and dislocations, a description of early results obtained on rate-dependent spherical indents under essentially static loading and in impacts.[168] The initiation of cracking was directly observed via TEM imaging. For the gradual spherical loading of an MgO crystal (001) surface, a series of micrographs was produced that optically tracked the loading behavior for larger ball size and consequently larger load over very nearly the total range of behavior described here between Figs. 9 and 13 for the respective Refs. 57 and 132. Clear delineation of slip band structures within the encompassing picture-frame structure was observed after the central indentation appeared as a shatter zone of multiple cracks. Dynamic tests involving 700 μm spherical diameter WC at 145 m/s impact on the (001) surface of a KCl crystal were also sequentially photographed with a high speed camera with sub-unit μs frame sequencing capability. Chaudhri employed the results to derive an operative shear stress that then was correlated with estimations of a linear dependence of dislocation velocity.

Dynamical aspects of $\langle 100 \rangle$ dislocation lines at indentations made on MgO $\{100\}$ crystal faces have been mentioned.[183] Williams *et al.*[385] made a comparison of both hardness and crack size dependencies measured in dropped ball experiments done on the same type MgO crystal surfaces as for the static measurements that were previously described[325]; see Fig. 34. Results from Rickerby and Macmillan[130] and Chaudhri *et al.*[386] are included in the figure.

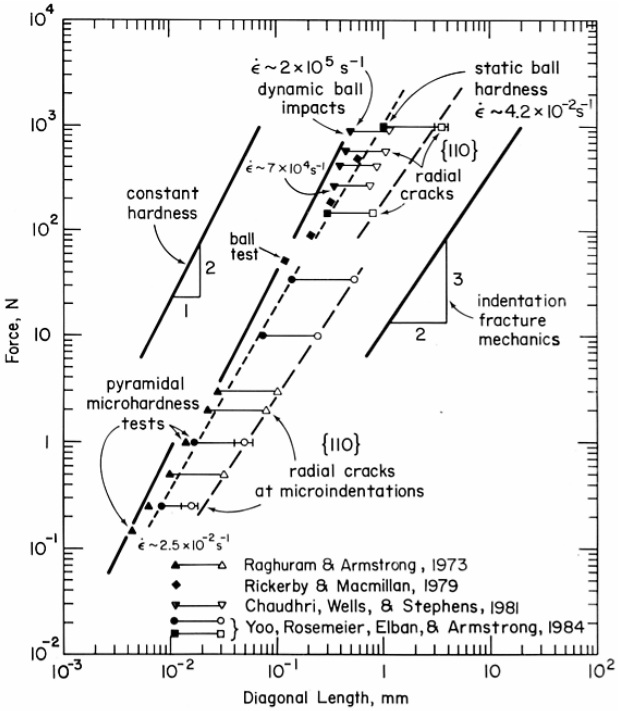

Fig. 38. Static and dynamic MgO crystal indentation measurements.[385]

An increased hardness at greater applied strain rate is seen by comparison of the topmost filled square and filled triangle points plotted in Fig. 38. The corresponding match of radial crack lengths shows an even greater effect of the strain rate.

6. Applications

The foregoing compilation of references and brief descriptions of them, while only covering a limited number of topics pertinent to hardness and hardness testing, provides evidence for the opening statement that one cannot hope to cover all aspects of the combined subjects. The situation is more true for all of the applications of hardness testing. Here, we mention only a few items that seem pertinent to the many application type topics.

6.1. *Quality control and ceramics*

As an example of the continuing progress in updating engineering standards, there is the recent note provided by Tobolski concerning the purview of ASTM on the subject.[387] A practical example of updating test equipment or methods of performing hardness tests is given in the report by Baxevani and Giannakoupoulos,[388] this consideration relates to some extent to the report by Schindler.[88] It is probably

safe to say that more hardness testing is done on ceramic materials than on any other type of material. Some evidence for this assertion comes from the results that have already been described. General coverage of the hardness considerations for ceramics is provided in reports by Roberts[389] and by Leavy *et al.*[390] Krell and Schaedlich[391] have described interpretation of ceramic hardness measurements on a depth-sensing basis. Nanoindentation size effect issues for initiation of plasticity have been described by Zhu *et al.*[392] A particular case of investigating the damage tolerance of ceramic Ti3SiC2 material has been reported by Kooi *et al.*[393]

6.2. *Thin films and coatings*

The topic of thin films and coatings deserves particular attention because of the physical condition of such materials are ideally suited to hardness testing of their mechanical properties. Important experimental results and interpretation have been provided by Doerner and Nix.[394] Yu *et al.* have provided an important elastic model description of flat, conical and spherical indentation hardnesses.[395]

In Ref. 395, graphical results are presented for the contact area and load dependencies on penetration depth for the film taken as an elastic layer either in frictionless contact or perfectly bonded onto a semi-infinite elastic half-space. Kulchytsky–Zhyhailo and Rogowski[396] have evaluated the stresses for a hard coating on a layered elastic half-space. Emphasis is given to the important ratio of layer thickness and contact area.

Chicot *et al.* have reported a method for determining thin film hardness by means of modeling the indentation loading curve.[397] Figure 40 shows one reported result. The figure shows the loading curve result for a rather complex diamond-like

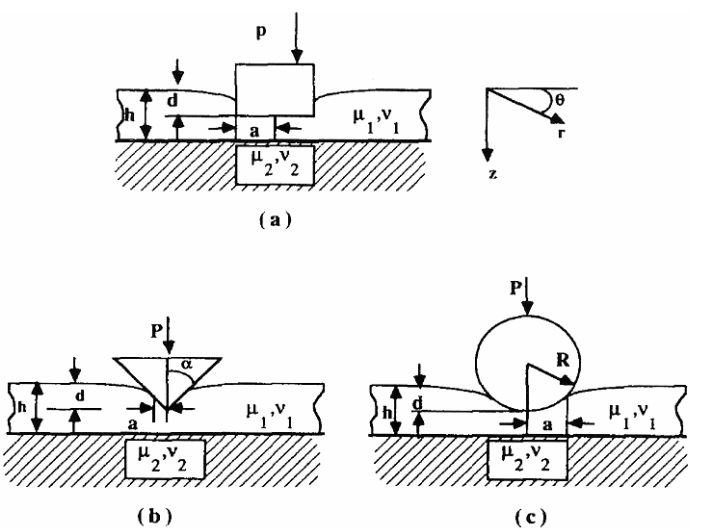

Fig. 39. Schematic diagram and parameters for flat, conical and spherical indentation of thin films.[395]

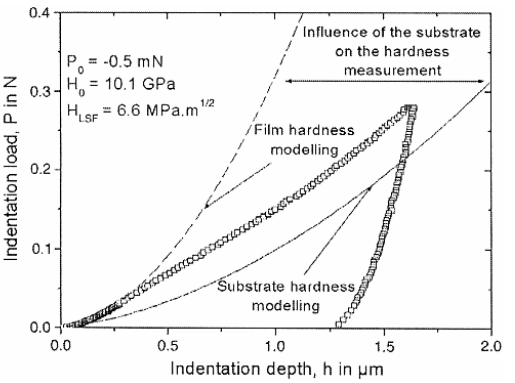

Fig. 40. Relationship of loading dependencies for limiting film and substrate hardnesses[397]

carbon coating of 2.55 μm thickness and measured 0.063 μm roughness put onto a 316L stainless steel substrate. Such films generally exhibit diamond pyramid (Vickers) hardnesses in the range of 20–40 GPa.[397] The limiting parabolic dependencies shown for the film and substrate apply for a constant hardness value; see Fig. 4 of Ref. 95. The quantities, P_0, H_0 and H_{LSF} are correction factors introduced for zero contact load and ISE corrections employed after the method of Nix and Gao.[56] Such load–penetration depth measurements were carried through to counterpart hardness versus relative indentation depth curves, again, shown to be contained within the limiting hardness values of the film and substrate materials. There is the relationship of the results to the MD simulations reported by Solar *et al.*[246] The hardness of ultra-thin-films has been characterized by Gitis *et al.* for relationship to tribological properties.[398]

Jaffar[399] has provided prediction of film thickness taken as a soft layer being squeezed by rigid spherical impression being made onto a rigid foundation. There is connection with lubrication of a synovial (bone) joint. The topic is only slightly removed from a coupled pair of articles by McCarthy *et al.*[400] on the sharpness of straight edge blades assessed in terms of their tip radii, edge angles and blade profiles. Hooke, in Ref. 2, had also applied his magnifying glass to making observations about the sharpness, or more accurately, the dullness of a 17th century razor blade. McCarthy *et al.* employed a finite element description and ABAQUS to develop a "blade sharpness index". To illustrate further connection with hardness, there are the two reports: first, by Akona *et al.*[401] on scratching materials ranging in hardness from butter to steel; and secondly, by Keryvin *et al.*[402] on scratching a ZrCuAlNi bulk metallic glass. The results of the latter report may be related to hardness and plastic flow measurements obtained on a related material by Ye *et al.*[403]

Hakiri *et al.*[404] have applied the optical indentation microscopy technique[73] to report *in-situ* observations of Berkovich-indented contact areas of thin film/substrate composites and modifications of sinking-in or piling-up behaviors in association with hardness and elastic modulus determinations. Continuous load-

ing curve results were obtained for sol–gel derived $MeSiO_{3/2}$ film put onto a number of polymer and glass substrate materials. The ISE has been investigated in single crystal copper films by Zong and Soboyejo[405] while MD simulations of single and polycrystal copper films on rigid or single crystal aluminum substrates have been investigated by Bolesta and Fomin[406]; see Fig. 29 and Ref. 307. Guisbiers *et al.*[407] investigated the nanoindentation hardness of isolated thin films of tantalum in association with fracture toughness and Young's modulus determinations. The hardness followed the H–P dependence given above in Eq. (17). Wang *et al.* have reported on surface roughness and internal stress aspects of the nanoindentation hardness of boron-doped polysilicon material.[408] Son *et al.* have correlated hardness, wear resistance and corrosion resistance of iron-alloy powder consolidated materials.[409] Quantitative hardness results are reported for measurements made by Kauffman *et al.*[410] on a nanocrystalline titanium nitride/silicon nitride coating.

For purpose of relating to polymer coating applications, Spinks *et al.* have performed spherical indentation testing of polystyrene material at temperatures though the glass transition temperature and reported glassy and rubbery modulus values.[411] The measurements relate to another report by Dinelli *et al.* in which indentation versus time curves were determined for thin surface layers so as to relate to the issue of a reduction in glass transition temperature because of the free surface.[412] Gacoin *et al.*[413] also determined hardness test results for an elastic substrate coated acrylate polymer film in the glass transition zone. The viscoelastic moduli were found to be sensitive to hydrostatic pressure. Bundschuh *et al.*[414] have reported hardness and Young's modulus values, in the latter case achieving a value of 9.3 GPa approaching the theoretical value of ~ 10 GPa or higher, for an epitaxially deposited, intrinsically porous, metal-organic framework material designated as HKUST-1.

7. Summary

A review has been presented of hardness and hardness testing results compiled on many different materials and over a very large range in indenter tip dimensions and applied loads. The indenter dimensions have ranged from those for the atomic-scale sharpness of tungsten field emission tips to millimeter-scale spheres, thus corresponding to a range in scale from nano-to-macro-indentation hardness testing. The applied loads have ranged over a scale from hundredths of micro-Newtons to kilo-Newtons. The structural states of the different materials tested have varied between the limits of either being essentially perfect crystals to being amorphous materials and each type of material tested in bulk or thin-film condition. Emphasis has been given to the important use and interpretation of continuous indentation loading curves obtained with a spherical indenter tip, particularly as naturally occurs for the rounded tip loading in nanoindentation hardness tests. Metrological aspects of the subject have been discussed. On such a combined basis, the elastic, plastic and cracking aspects of actual hardness or simulated results have been described for

conventional single crystal, polycrystal, nanopolycrystal and polyphase composites, and encompassing all types of atomic or molecular bonding.

Acknowledgments

The authors wish to thank Ms. Peggy Feild, Loyola Library, for help with ferreting of reference information and Ms. Marion Wielgosz, Loyola Technology Center, for providing the high resolution scans of Figs. 19 and 32.

Appendix A. Selected References on Topics and Sub-Topics of the Main Text

A.1. *Introduction*

A.1.1. *Historical aspects*

L. Makkonen, A thermodynamic model of sliding friction, *AIP Advances* **2**, 012179 (2012).
T. Thome, S. Fouchez and S. Delalande, Determination of silicone coating Young's modulus using AFM, *Physica B* **404**, 22–25 (2009).
L. Sirghi and F. Rossi, The effect of adhesion on the contact radius in atomic force microscopy indentation, *Nanotechnology* **20**, 365702 (2009).
E.-Y. Kwon, Y.-T. Kim and D.-E. Kim, Investigation of penetration force of living cell using an AFM, *J. Mech. Sci. Technol.* **23**, 1932–1938 (2009).
Y.-T. Yang, J.-D. Liao, Y.-L. Lee, C.-W. Chang and H.-J. Tsai, Ultrathin phospholipid layers physically adsorbed upon glass characterized by nanoindentation at the surface contact level, *Nanotechnology* **20**, 195702 (2009).
S. Chowdhury and M. T. Laugier, Non-contact AFM with a nanoindentation technique for measuring the mechanical properties of thin films, *Nanotechnology* **15**, 1017–1022 (2004).
O. Miesbauer, M. Gotzinger and W. Peukert, Molecular dynamics simulations of the contact between two NaCl nanocrystals: Adhesion, jump to contact and indentation, *Nanotechnology* **14**, 371–376 (2003).

A.1.2. *Analysis*

N. A. Sakharova, P. A. Prates, M. C. Oliveira, J. V. Fernandes and J. M. Antunes, A simple method for estimation of residual stresses by depth-sensing indentation, *Strain* **48**(1), 75–87 (2012).
S.-W. Kim and S.-S. Kim, Effect of frictional heating on the propagation of surface crack under Hertzian contact loading, *Int. J. Mod. Phys. B* **24**, 2524–2529 (2010).
I. Kosenko and E. Aleksandrov, Volumetric modification of the Hertz contact problem and its application to the multibody dynamics simulation, *J. Mech. Sci. Technol.* **23**, 931–937 (2009).
Y. P. Zheng, A. P. C. Choi, H. Y. Ling and Y. P. Huang, Simultaneous estimation

of Poisson's ratio and Young's modulus using a single indentation: A finite element study, *Meas. Sci. Technol.* **20**, 045706 (2009).
S. Jin and S. S. Kim, Estimation of stress intensity factors for vertical edge crack under Hertzian contact by geometric function method, *Int. J. Mod. Phys. B* **17**, 1659–1664 (2003).
F. M. Borodich, L. M. Keer and C. S. Korach, Analytical study of fundamental nanoindentation test relations for indenters of non-ideal shapes, *Nanotechnology* **14**, 803–808 (2003).
G. Geandier, S. Denis and A. Mocellin, Float glass fracture toughness determination by Hertzian contact: Experiments and analysis, *J. Non-Cryst. Solids* **318**, 284–295 (2003).
M. S. Bruno and K. J. Dunn, Does the Hertz solution estimate pressures correctly in diamond indenter experiments?, *Physica B & C* **139**, 746–749 (1986).

A.2. *Stress–strain behavior*

A.2.1. *Connection to compression/tension testing*

B. R. Donohue, A. Ambrus and S. R. Kalidindi, Critical evaluation of the indentation data analyses methods for the extraction of isotropic uniaxial mechanical properties using finite element models, *Acta Mater.*, **60**, 3943–3952 (2012).
D.-K. Leu, Evaluation of friction coefficient using indentation model of Brinell hardness test for sheet metal forming, *J. Mech. Sci. Technol.* **25**, 1509–1517 (2011).
B.-M. Kim, C.-J. Lee and J.-M. Lee, Estimations of work-hardening exponents of engineering metals using residual indentation profiles of nanoindentation, *J. Mech. Sci. Technol.* **24**, 73–76 (2010).
M. M. Chaudhri, Strain hardening around spherical indentations, *Phys. Stat. Sol. A* **182**, 641–652 (2000).

A.2.2. *Direct determination of the hardness stress–strain curve*

J. Dean, J. M. Wheeler and T. W. Clyne, Use of quasistatic nanoindentation data to obtain stress-strain characteristics for metallic materials, *Acta Mater.* **58**, 3613–3623 (2010).

A.2.3. *Metrology considerations*

L. Rautkari, K. Laine, A. Kutnar, S. Medved and M. Hughes, Hardness and density profile of surface densified and thermally modified Scots pine in relation to degree of densification, *J. Mater. Sci.* **48**, 2370–2375 (2013).
X. Yin and K. Komvopoulos, A discrete dislocation plasticity analysis of a single-crystal semi-infinite medium indented by a rigid surface exhibiting multi-scale roughness, *Philos. Mag.* **92**(24), 2984–3005 (2012).
L. Ma, D. J. Morris, S. L. Jennerjohn, D. F. Bahr and L. E. Levine, The role of

probe shape on the initiation of metal plasticity in nanoindentation, *Acta Mater.* **60**, 4729–4739 (2012).
K. Cicha, T. Koch, J. Torgersen, Z. Li, R. Liska and J. Stampfl, Young's measurement of two-photon polymerized micro-cantilevers by using nanoindentation equipment, *J. Appl. Phys.* **112**, 094906 (2012).
Y.-H. Lee, B.-G. Yoo and J.-I. Jang, Bluntness measurement of a Berkovich indenter, *Int. J. Mod. Phys. B* **25**, 4273–4276 (2011).
V. Seena, A. Fernandes, P. Pant, S. Mukherji and V. R. Rao, Polymer nanocomposite nanomechanical cantilever sensors: Material characterization, device development and application in explosive vapour detection, *Nanotechnology* **22**, 295501 (2011).
C. W. Chang and J. D. Liao, Nanoindentation at the surface contact level: Applying a harmonic frequency for measuring contact stiffness of self-assembled monolayers adsorbed on gold, *Nanotechnology* **19**, 315703 (2008).
F.-Y. Chen and R.-C. Chang, Study of the effect of imperfect tips on nanoindentation by FEM, *J. Mech. Sci. Technol.* **21**, 1471–1476 (2007).
J. McMinis, R. Crombez, E. Montalvo and W. D. Shen, Determination of the cross-sectional area of the indenter in nanoindentation tests, *Physica B* **391**, 118–123 (2007).
S. Qu, Y. Huang, G. M. Pharr and K. C. Hwang, The indentation size effect in the spherical indentation of iridium: A study via the conventional theory of mechanism-based strain gradient plasticity, *Int. J. Plast.* **22**, 1265–1286 (2006).
V. Bursikova, P. Sladek, P. Stahel and J. Bursik, Mechanical properties of thin silicon films deposited on glass and plastic substrates studied by depth-sensing indentation technique, *J. Non-Cryst. Solids* **352**, 1242–1245 (2006).
Y. M. Soifer and A. Verdyan, Dislocation indentation size effect in KCl single crystals, *Phys. Stat. Sol. A* **202**, 2454–2461 (2005).

A.2.4. *Nanoindentation testing*

A. Barnoush, Correlation between dislocation density and nanomechanical response during nanoindentation, *Acta Mater.* **60**, 1268–1277 (2012).
C. Schilde, B. Westphal and A. Kwade, Effect of the primary particle morphology on the micromechanical properties of nanostructured alumina agglomerates, *J. Nanopart. Res.* **14**, 745 (2012).
C. Tromas, M. Arnoux and X. Milhet, Hardness cartography to increase the nanoindentation resolution in heterogeneous materials: Application to a nickel-based single-crystal superalloy, *Scripta Mater.*, **66**, 77–80 (2012).
A. Kumar and K. Zeng, Measurement of hardness of ultrathin films by the first derivative of load–displacement curve from nanoindentation data, *Int. J. Mod. Phys. B* **24**, 256–266 (2010).
P.-J. Wei, W. L. Liang, C. F. Ai and J. F. Lin, A new method for determining the strain energy release rate of an interface via force-depth data of nanoindentation

tests, *Nanotechnology* **20**, 025701 (2009).
M. Balentekin, S. G. Onaran and F. L. Degertekin, Quantitative mechanical characterization of materials at the nanoscale through direct measurement of time-resolved tip-sample interaction forces, *Nanotechnology* **19**, 085704 (2008).
Y. Arai, Y.-H. Liang, K. Ozasa, M. Ohashi and E. Tsuchida, Simultaneous measurement of nanoprobe indentation force and photoluminescence of InGaAs/GaAs quantum dots and its simulation, *Physica E* **36**, 1–11 (2007).
B. Wolf, D. Meyer, A. Beiger and P. Paufler, Photoplastic effects in nanoindentation experiments, *Philos. Mag. A*, **82**(10), 1865–1872 (2002).
H. S. Leipner, D. Lorenz, A. Zeckzer, H. Lei and P. Grau, Nanoindentation pop-in effect in semiconductors, *Physica B* **308**, 446–449 (2001).

A.3. *Elastic, plastic, cracking behaviors*

A.3.1. *Elasticity*

F. Li, D. Ngo, J. Yang and C. Daraio, Tunable phononic crystals based on cylindrical Hertzian contact, *Appl. Phys. Letts.* **101**, 171903 (2012).
J. J. Roa, G. Oncins, F. T. Dias, V. N. Vieira, J. Schaf and M. Segarra, AFM as an alternative for Young's modulus determination in ceramic materials in elastic deformation regime, *Physica C* **471**, 544–548 (2011).
R. Bernal, Ch. Tassius, F. Melo and J.-Ch. Geminard, Elastic response and wrinkling onset of curved elastic membranes subjected to indentation test, *Eur. Phys. J. E* **34**(2), 1–5 (2011).

A.3.2. *Plasticity*

N. Zaafarani, D. Raabe, F. Roters and S. Zaefferer, On the origin of deformation-induced rotation patterns below nanoindents, *Acta Mater.* **56**, 31–42 (2008).
W. W. Gerberich, W. M. Hook, M. J. Cordill, C. B. Carter, C. R. Perrey, J. V. Heberlein and S. L. Girschick, Reverse plasticity in single crystal silicon nanospheres, *Int. J. Plast.* **21**, 2391–2405 (2005).

A.3.2.1. Slip, twinning, dislocations

B. O. Kolbesen, J. Mahliss and D. Possner, Defect delineation by chemical etching techniques in silicon and engineered silicon substrates: Novel chemistries and basic aspects, *Phys. Stat. Sol. A* **208**, 584–587 (2011).
W. B. Lee and Y. P. Chen, Simulation of microindentation hardness of fcc single crystals by mechanism-based strain gradient crystal plasticity, *Int. J. Plast.* **26**, 1527–1540 (2010).
M. Rathinam, R. Thillaigovindan and P. Paramasivam, Nanoindentation of aluminum (100) at various temperatures, *J. Mech. Sci. Technol.* **23**, 2652–2657 (2009).
A. Lefebvre, Y. Androussi and G. Vanderschaeve, A TEM investigation of the dislo-

cation rosettes around Vickers indentations in GaAs, *Phys. Stat. Sol. A* **99**, 405–412 (1987).
V. B. Pariiskii, Effect of stress state on the shape of the dislocation rosette near an indentation in some alkali halide crystals, *Phys. Stat. Sol.* **19**, 525–532 (1967).

A.3.2.2. Crystal and plastic anisotropy

B. Roebuck, P. Klose and K. P. Mingard, Hardness of hexagonal tungsten carbide crystals as a function of orientation, *Acta Mater.* **60**, 6131–6143 (2012).
A. A. Porporati and G. Pazzotti, Polarized Raman spectroscopy clarifies the effect of crystal anisotropy on elastic stress fields developed on the surface of silicon single crystal, *Phys. Stat. Sol. A* **208**, 1093–1098 (2011).
Y. Liu, S. Varghese, J. Ma, M. Yoshino, H. Lu and R. Komanduri, Orientation effects in nanoindentation of single crystal copper, *Int. J. Plast.* **24**, 1990–2015 (2008).
S. N. Luo, J. G. Swadener, C. Ma and O. Tschauner, Examining crystallographic orientation dependence of hardness of silica stishovite, *Physica B* **399**, 138–142 (2007).

A.3.2.3. Polycrystals/polyphases/composites

S.-W. Chang, A. K. Nair and M. J. Buehler, Nanoindentation study of size effects in nickel-graphene nanocomposites, *Philos. Mag. Letts.* doi:10.1080/09500839.2012.759293 (2013).
Y. Tian, B. Xu, D. Yu, Y. Ma, Y. Wang, Y. Jiang, W. Hu, C. Tang, Y. Gao, K. Luo, Z. Zhao, L.-M. Wang, B. Wen, J. He and Z. Liu, Ultrahard nanotwinned cubic boron nitride, *Nature* **493**, 385–386 (2013).
J. Qin, N. Nishiyama, H. Ohfuji, T. Shinmei, L. Lei, D. He and T. Irifune, Polycrystalline gamma-boron: As hard as polycrystalline boron nitride, *Scripta Mater.* **67**, 257–260 (2012).
A. K. Kothari, S. Hu, Z. Xia, E. Konca and B. W. Sheldon, Enhanced fracture toughness in carbon-nanotube-reinforced amorphous silicon nitride nanocomposite coatings, *Acta Mater.* **60**, 3333–3339 (2012).
C. Tromas, J. C. Stinville, C. Templier and P. Villechaise, Hardness and elastic modulus gradients in plasma-nitrided 316L polycrystalline stainless steel investigated by nanoindentation tomography, *Acta Mater.* **60**, 1965–1973 (2012).
Q. Tang and T. Yang, Nanoindentation simulation on mechanical behavior of nanocrystalline nickel, *Int. J. Mod. Phys. B* **25**, 1689–1700 (2011).
S. Qu and H. Zhou, Hardening by twin boundary during nanoindentation in nanocrystals, *Nanotechnology*, **21**, 335704 (2010).
S. Pathak, Z. G. Cambaz, S. R. Kalidindi, J. G. Swadner and Y. Gogotsi, Viscoelasticity and high buckling stress of dense carbon nanotube brushes, *Carbon* **47**, 1969–1976 (2009).
S. S. Nair and M. A. Khadar, Inverse Hall-Petch effect in nanostructured ZnS, *J.*

Nanopart. Res. **11**, 485–490 (2009).
L. Zhang, T. Ohmura, S. Emura, N. Sekido, F. Yin, X. Min and K. Tsuzaki, Evaluation of matrix strength in ultra-fine grained pure Al by nanoindentation, *J. Mater. Res.* (2009).
P. Vena, D. Gastaldi and R. Contro, Determination of the effective elastic-plastic response of metal-ceramic composites, *Int. J. Plast.* **24**, 483–508 (2008).

A.3.3. *Cracking and indentation fracture mechanics*

R. Ruzek, J. Pavlas and R. Doubrava, Application of indentation as a retardation mechanism for fatigue crack growth, *Int. J. Fatigue* **37**, 92–99 (2012).
H. Chai, On the mechanics of edge chipping from spherical indentation, *Int. J. Fract.* **169**, 85–95 (2011).
T. Vuherer, L. Milovic and V. Gliha, Behaviour of small cracks during their propagation from Vickers indentations in coarse-grain steels: An experimental investigation, *Int. J. Fatigue* **33**, 1505–1513 (2011).
I. Ratschinski, H. S. Leipner, F. Heyroth, W. Franzel, R. Hammer and M. Jurisch, Dislocations and cracks and Vickers indentations in GaN and GaAs bulk crystals, *Phys. Stat. Sol. C* **8** doi:10.1002/pssc.201084020 (2011).
I. Ratschinski, F. Heyroth, W. Franzel and H. S. Leipner, Anisotropy of crack and dislocation formation in GaAs, *Phys. Stat. Sol. C* **6** 1836–1840 (2009).
K. A. Iyer, Relationships between multiaxial stress states and internal fracture patterns in sphere-impacted silicon carbide, *Int. J. Fract.* **146**, 1–18 (2007).
M. Tanaka, K. Higashida, H. Nakashima, H. Takagi and M. Fujiwara, Orientation dependence of fracture toughness measured by indentation methods and its relation to surface energy in single crystal silicon, *Int. J. Fract.* **139**, 383–394 (2006).
A. Mikowski, F. C. Serbena, C. E. Foerster and C. M. Lepienski, Statistical analysis of threshold load for radial crack nucleation by Vickers indentation in commercial sodalime silica glass, *J. Non-Cryst. Solids* **352**, 3544–3549 (2006).
H. Y. Lin, J. L. Chu and S. Lee, The brittle to ductile transition of single crystal materials: An indentation model, *J. Mater. Sci.*, **36**, 3769–3775 (2001).

A.4. *Amorphous and polymeric materials*

W. Liu, H. Ruan and L. Zhang, On the plasticity event in metallic glass, *Philos. Mag. Letts.* doi:10.1080/09500839.2012.755270 (2013).
M. Rodríguez, J. M. Molina-Aldareguia, C. González and J. Llorca, Determination of the mechanical properties of amorphous materials through instrumented nanoindentation, *Acta Mater.* **60**, 3953–3964 (2012).

A.4.1. *Glasses*

L. Perrière, S. Nowak, S. Brossard, M.-T. Thai, M. Biétry and Y. Champion, Nanoindentation study of chemical effects on the activation volume controlling shear

band initiation in metallic glasses, *Scripta Mater.* **68**, 183–186 (2013).
K. R. Gadeirab, F. A. Bonilla and M. Chiesa, Densification modeling of fused silica under nanoindentation, *J. Non-Cryst. Solids* **358**, 392–398 (2012).
I.-C. Choi, Y. Zhao, Y.-J. Kim, B.-G. Yoo, J.-Y. Suh, U. Ramamurty and J.-I. Jang, Indentation size effect and shear transformation zone size in a bulk metallic glass in two different structural states, *Acta Mater.* **60**, 6862–6868 (2012).
K. Sangwal, J. Borc and T. Kavetsky, Study of microindentation cracks in bismuth-doped arsenic selenide glasses, *J. Non-Cryst. Solids* **357**, 3117–3122 (2011).
Y.-H. Lee, J. S. Park, H. M. Lee and S. H. Nahm, Stress-strain relationship of $Zr_{55}Al_{10}Ni_5Cu_{30}$ metallic glass analyzed by 3D images on spherical indents, *Int. J. Mod. Phys. B* **24**, 2453–2459 (2010).
A. Dey, R. Chakraborty and A. K. Mukhopadhyay, Nanoindentation of soda lime-silica glass: Effect of strain rate, *Int. J. Appl. Glass Sci.* **2**(2), 144–155 (2011).
Y. Kato, H. Yamazaki, S. Yoshida and J. Matsuoka, Effect of densification on crack initiation under Vickers indentation test, *J. Non-Cryst. Solids*, **356**, 1768–1773 (2010).
Y. W. Bao and S. J. Gao, Local strength evaluation and proof test of glass components via spherical indentation, *J. Non-Cryst. Solids* **354**, 1378–1381 (2008).
A. Koike and M. Tomozawa, IR investigation of density changes of silica glass and sodalime silicate glass caused by microhardness indentation, *J. Non-Cryst. Solids* **353**, 2318–2327 (2007).
L. F. Liu, L. H. Dai, Y. L. Bai and B. C. Wei, Initiation and propagation of shear bands in Zr-based bulk metallic glass under quasistatic and dynamic shear loadings, *J. Non-Cryst. Solids* **351**, 3259–3270 (2005).
S. Deriano, A. Jarry, T. Rouxel, J. C. Sangleboeuf and S. Hampshire, The indentation fracture toughness (K–C) and its parameters: The case of silica-rich glasses, *J. Non-Cryst. Solids* **344**, 44–50 (2004).
E. C. Ziemath and P. S. P. Herrmann, Densification and residual stresses induced in glass surfaces by Vickers indentations, *J. Non-Cryst. Solids* **273**, 19–24 (2000).

A.4.2. *Polymers*

D. G. T. Strange, T. L. Fletcher, K. Tonsomboon, H. Brown, X. Zhao and M. Oyen, Separating poroviscoelastic deformation mechanisms in hydrogels, *Appl. Phys. Lett.* **102**, 031913 (2013).
P. J. Wei, W. X. Shen and J. F. Lin, Analysis and modeling for time-dependent behavior of polymers exhibited in nanoindentation tests, *J. Non-Cryst. Solids* **354**, 3911–3918 (2008).
T. Altebaeumer, B. Gotsmann, A. Knoll, G. Cherubini and U. Duerig, Self-similarity and finite-size effects in nano-indentation of highly crosslinked polymers, *Nanotechnology* **19**, 475301 (2008).
L. Anand and N. M. Ames, On modeling the micro-indentation response of an amorphous polymer, *Int. J. Plast.* **22**, 1123–1170 (2006).

N. M. Vriend and A. P. Kren, Determination of the viscoelastic properties of elastomeric materials by the dynamic indentation method, *Test. Method*, **23**, 369–375 (2004).

A.5. *Deformation rate effects*

A.5.1. *Creep*

C. C. Huang, M. K. Wei and S. Lee, S. Transient and steady-state nanoindentation creep of polymeric materials, *Int. J. Plast.* **27**, 1093–1102 (2011).
H. Takagi, M. Dao and M. Fujiwara, Pseudo-steady indentation creep, *Int. J. Mod. Phys. B* **24**, 227–237 (2010).
R. Mahmudi, A. R. Geranmayeh, S. R. Mahmoodi and A. Khalatbari, Effect of cooling rate on the room-temperature indentation creep of cast lead-free Sn–Bi solder alloys, *Phys. Stat. Sol. A* **204**, 2302–2308 (2007).
J. Gratier, R. Guiguet, F. Renard, L. Jenatton and D. Bernard, A pressure solution creep law for quartz from indentation experiments, *J. Geophys. Res.* **114**, B03403 (2009).

A.5.2. *Dynamics*

E. J. Haney and G. Subhash, Static and dynamic indentation response of basal and prism plane sapphire, *J. Eur. Ceram. Soc.*, **31**(9), 1713–1721 (2011).
H.-S. Shin, S.-N. Chang and D.-K. Kim, Deformation behaviors of zirconium-based bulk metallic glass under impact indentation, *Int. J. Mod. Phys. B* **22**, 1775–1782 (2008).
C. M. Suh, D. K. Kim and M. H. Lee, A study on damage behavior of glass by oblique impact of steel ball, *Int. J. Mod. Phys. B* **20**, 4291–4296 (2006).

A.6. *Applications*

A.6.1. *Quality control and ceramics*

D. Jiang, Recent progresses in the phenomenological description for the indentation size effect in microhardness testing of brittle ceramics, *J. Adv. Ceram.* **1**(1), 38–49 (2012).
K. H. Guahk, I. S. Han and K. S. Lee, Strength degradation from Hertzian contact damage in nitrided pressureless sintered silicon nitride ceramics, *Int. J. Mod. Phys. B* **22**, 1819–1826 (2008).
J.-H. Kim, H. E. Kim, D. K. Kim and S. N. Chang, Characterization of subsurface damage of explosively indented silicon nitride ceramics, *Int. J. Mod. Phys. B* **22**, 1504–1509 (2008).

A.6.2. *Thin films and coatings*

J. J. Pang, M. J. Tan, K. M. Liew and C. Shearwood, Nanoindentation study of size effect and loading rate effect on mechanical properties of a thin film metallic

glass $Cu_{49.3}Zr_{50.7}$, *Physica B* **407**, 340–346 (2012).
J. Y. Sun, J. L. Hu, Z. L. Zheng, X. T. He and H. H. Geng, A practical method for simultaneous determination of Poisson's ratio and Young's modulus of elasticity of thin films, *J. Mech. Sci. Technol.* **25**, 3165–3171 (2011).
F. Zhang, R. Saha, Y. Huang, W. D. Nix, K. C. Hwang, S. Qu and M. Li, Indentation of a hard film on a soft substrate: Strain gradient hardening effects, *Int. J. Plast.* **23**, 25–43 (2007).
V. M. Kindrachuk, B. A. Galanov, V. V. Kartuzov and S. N. Dub, On elastic nanoindentation of coated half-spaces by point indenters of non-ideal shapes, *Nanotechnology* **17**, 1104–1111 (2006).
M.-Q. Le, J.-W. Yi and S.-S. Kim, Numerical investigation on ceramic coatings under spherical indentation with metallic interlayer. 1: Uncracked coatings, *Int. J. Mod. Phys. B*, **20**, 4395–4400 (2006).

References

1. S. M. Walley, *Mater. Sci. Tech.* **28**(9–10), 1228 (2012).
2. R. Hooke, Observ. I. Of the point of a sharp small needle, in *Micrographia, or Physiological Descriptions of Minute Bodies made by Magnifying Glasses; with Observations and Inquiries thereupon*, eds. J. Martyn and J. Allestry (Printers to the Royal Society, London, 1665), pp. 1–4.
3. H. C. Sorby, *J. Iron Steel Inst.* **31**, 255 (1887).
4. E. W. Mueller, Direct observation of crystal imperfections by field ion microscopy, in: *Direct Observation of Imperfections in Crystals*, eds. J. B. Newkirk and J. H. Wernick (Interscience Publishers, New York, 1962). pp. 77–99.
5. J. B. Pethica and M. D. Pashley, *Nature* **305**, 666 (1983).
6. G. Binnig and H. Rohrer, *Surf. Sci.* **126**, 236 (1983); Gerd Binnig, *Nobel Lecture – Scanning Tunneling Microscopy – From Birth to Adolescence*, Nobelprize.org 13 Nov 2012.
7. J. Miller, *Phys. Today* **65**(11), 14 (2012).
8. E. Carrasco *et al.*, *Philos. Mag.* **88**(3), 281 (2008).
9. G. S. Blackman, C. M. Mate and M. R. Philpott, *Phys. Rev. Letts.* **65**(18), 2270 (1990).
10. C. M. Mate, *MRS Bull.* **27**, 967 (2002).
11. D. Tabor and R. H. S. Winterton, *Proc. Roy. Soc., London A* **312**, 435 (1969).
12. M. D. Pashley, J. B. Pethica and D. Tabor, *Wear* **100**, 7 (1984).
13. N. Gane and J. M. Cox, *Philos. Mag.* **22**, 881 (1970).
14. N. Gane, *Proc. Roy. Soc. London A* **317**, 367 (1970).
15. K. L. Jackson *et al.*, *J. Mater. Sci.* **32**, 5035 (1997).
16. H. Hertz, Ueber die Beruehrung fester elasticher Koerper, *J. reine angewandte Mathematik* **92**, 156 (1881); see "On the contact of elastic bodies", in. *Miscellaneous Papers by Heinrich Hertz*, eds. D. E. Jones and G. A. Schott (Macmillan, London, 1896), pp. 146–162.
17. H. Hertz, Ueber die Beruehung fester elastiche Koerper and ueber die Harte, in: *Verhandlungen des Vereins zur Befoerderung des Gewerbefleisses* (Leipzig, 1882); see "On the contact of rigid elastic bodies and on hardness", in: *Miscellaneous Papers by Heinrich Hertz*, eds. D. E. Jones and G. A. Schott (Macmillan, London, 1896), pp. 163–183.

18. M. T. Hueber, *Ann. Phys.* **319**, 153 (1904).
19. H. Hencky, *Z. Angew. Math. Mech.* **1**, 15 (1921).
20. F. C. Frank and B. R. Lawn, *Proc. R. Soc. London A* **299**, 291 (1967).
21. M. T. Laugier, *J. Am. Ceram. Soc.* **68**(2), C-51 (1985).
22. W. L. Elban, D. B. Sheen and J. N. Sherwood, *J. Cryst. Growth* **137**, 304 (1994).
23. C. Atkinson, I. M. Martinez-Esnaola and M. R. Elizalde, *Mater. Sci. Tech.* **28**(4), 1079 (2012).
24. K. E. Puttick, L. S. A. Smith and L. E. Miller, *J. Phys. D: Appl. Phys.* **10**, 617 (1977).
25. R. Lach, L. A. Gyurova and W. Grellmann, *Polym. Test.* **26**, 51 (2007).
26. J. Boussinesq, *Application des Potentials a l'etude de l'Equilibre et du movement des solides elastiques* (Gauthier-Villars, Paris, FR, 1885).
27. B. R. Lawn, *J. Appl. Phys.* **39**, 4828 (1968).
28. J. A. Brinell, *Baumateriallenkunde* **5**, 276, 294, 317, 364, 392, 412 (1900).
29. A. Wahlberg, *J. Iron Steel Inst.* **59**, 243–298 (1901); *Ibid.* **60**, 234-271 (1901).
30. E. Meyer, *Z. Verein Deut. Ing.* **52**, 645, 740, 835 (1908).
31. P. Ludwik, *Die Kugeldruckprobe, ein neues Verfahren zur Haertebestimmung von Materialen* (Julius Springer, Berlin, 1908).
32. T. Turner, *J. Iron Steel Inst.* **79**, 426 (1909).
33. J. A. Ewing, *Proc. R. Soc. London* **58**, 123 (1895).
34. W. C. Unwin, *Proc. R. Soc. London* **57**, 178 (1894).
35. W. C. Unwin, *Min. Proc. Inst. Civil Engrs.* **129**, 334 (1896).
36. J. F. W. Bishop, R. Hill and N. F. Mott, *Proc. Phys. Soc. London* **57**, 147 (1945).
37. D. Tabor, *Proc. R. Soc. London A* **192**, 247 (1948).
38. D. Tabor, *The Hardness of Metals* (The Clarendon Press, Oxford, UK, 1951).
39. A. Krupkowski and W. Truszkowski, *Arch. Mech. Stos.* **2**, 235 (1950).
40. R. Hill, B. Storakers and A. B. Zdunek, *Proc. R. Soc., London A* **423**, 301 (1980).
41. T. Ishibashi and S. Shimoda, *Jpn. Soc. Mech. Eng. (JSME) Int. J.* **31**(1), 117 (1988).
42. W. Yan, Q. Sun and P. Hodgson, *Mater. Letts.* **62**, 2260 (2008).
43. B. Xu and X. Chen, *J. Mater. Res.* **25**(12), 2297 (2010).
44. I. M. Hutchings, *J. Mater. Res.* **24**(3), 581 (2009).
45. R. W. Armstrong and M. G. Vassilaros, *Stress–strain Curve from a Continuous Indentation Test* (David Taylor Naval Ship Research and Development Center, Annapolis, MD, 1987).
46. J. H. Westbrook, *Trans. Am. Soc. Met.* **45**, 221 (1953).
47. J. J. Gilman, *Chemistry and Physics of Mechanical Hardness* (John Wiley & Sons, New York, 2009), pp. 77, 122, 183.
48. G. Y. Chin *et al.*, *Scr. Metall.* **6**(6), 475 (1972).
49. V. Domnich *et al.*, *Rev. Adv. Mater. Sci.* **17**, 33 (2008).
50. R. F. Bunshah and R. W. Armstrong, Continuous ball indentation test for examining hardness dependence on indenter size, indentation size, and material grain size, in *The Science of Hardness Testing and Its Research Applications*, eds. J. H. Westbrook and H. Conrad (Am. Soc. Met., Metals Park, OH, 1973), Ch. 26, pp. 318–328.
51. R. W. Armstrong and W. H. Robinson, *New Zealand J. Sci.* **17**, 429 (1974).
52. R. W. Armstrong and W. L. Elban, *Mater. Sci. Tech.* **28**(9–10), 1060 (2012).
53. W. H. Robinson and S. D. Truman, *J. Mater. Sci.* **12**, 1961 (1977).
54. R. W. Armstrong and W. L. Elban, *Dislocations in Energetic Crystals*, in: *Dislocations in Solids*, Vol. 12, eds. F. R. N. Nabarro and J. P. Hirth (Elsevier B.V., Oxford, UK, 2004), Ch. 69, pp. 403–446.
55. J. B. Pethica, R. Hutchings and W. C. Oliver, *Philos. Mag.* **48**(4), 593 (1983).

56. W. D. Nix and H. Gao, *J. Mech. Phys. Sol.* **46**(3), 411 (1998).
57. K. Miyahara, N. Nagashima and S. Matsuoka, *Philos. Mag.* **82**(10), 2149 (2002).
58. C. Coupeau, J.-C. Girard and J. Rabier, Scanning probe microscopy and dislocations, in: *Dislocations in Solids*, Vol. 12, eds. F. R. N. Nabarro and J. P. Hirth (Elsevier B.V., Oxford, UK, 2004), Ch. 67, pp. 273–338.
59. R. W. Armstrong and W. L. Elban, *Exp. Mech.* **50**(4), 545 (2010).
60. O. Shikimaka and D. Grabco, *J. Phys. D: Appl. Phys.* **41**, 074012 (2008).
61. F. Abbes *et al.*, *J. Micromech. Microeng.* **20**, 065003 (2010).
62. D. Torres-Torres *et al.*, *Model. Simul. Mater. Sci. Eng.* **18**, 075006 (2010).
63. L. A. Berla *et al.*, *J. Mater. Res.* **25**(4), 735 (2010).
64. A. Ovcharenko *et al.*, *Tribology Lett.* **25**(2), 153 (2006).
65. X. D. Hou, A. J. Bushby and N. M. Jennett, *Meas. Sci. Technol.* **21**, 115105 (2010).
66. J.-C. Kuo *et al.*, *Strain* **46**, 277 (2010).
67. C. G. N. Pelletier *et al.*, *Philos. Mag.* **88**(9), 1291 (2008).
68. D. Chhavan *et al.*, *Rev. Sci. Instrum.* **83**, 115110 (2012).
69. D. Tranchida *et al.*, *Macromolecules*, **44**, 368 (2011).
70. I. Chakraborty and B. Balachandran, Noise influenced elastic cantilever dynamics with nonlinear tip interaction forces, *Nonlinear Dyn.*, **66**, 427–439 (2011); Near-grazing dynamics of base excited cantilevers with nonlinear tip interactions, *Ibid.* doi:10.1007/s11071-012-0534-8 (2012).
71. H. Kim, G. Venturini and A. Strachan, *J. Appl. Phys.* **112**, 094325 (2012).
72. M. S. Rodrigues *et al.*, *Appl. Phys. Lett.* **101**, 203105 (2012).
73. T. Miyajima and M. Sakai, *Philos. Mag.* **86**(33–35), 5729 (2006).
74. C. Feng and B. S.-J. Kang, *Exp. Mech.* **46**, 91 (2006).
75. C. Feng and B. S. Kang, *Exp. Mech.* doi:10.1007/s11340-007-9074-4 (2007).
76. S.-K. Kang *et al.*, *J. Mater. Res.* **24**(9), 2965 (2009).
77. X. Cai, *J. Mater. Sci. Lett.* **12**, 301 (1993).
78. Y. Zait, Y. Kligerman and I. Etsion, *Int. J. Sol. Struct.* **47**, 990 (2010).
79. C. G. N. Pelletier, *Poly. Test.* **26**, 949 (2007).
80. S. W. Wai *et al.*, *Poly. Test.* **23**, 501 (2004).
81. P. J. Wei, P. W. Tsai and J. F. Lin, *Tribology Int.* **41**, 1247 (2008).
82. P. Lu and S. J. O'Shea, *J. Phys. D: Appl. Phys.* **45**, 475303 (2012).
83. N. H. Faisal, R. L. Reuben and R. Ahmed, *Meas. Sci. Technol.* **22**, 015703 (2011).
84. T. Jochum *et al.*, *J. Am. Ceram. Soc.* **92**(4), 857 (2009).
85. M. M. Chaudhri, *Philos. Mag.* **77**(1), 7 (1998).
86. D. Chicot, *Mater. Sci. Eng. A* **499**, 454 (2009).
87. J. Chen *et al.*, *J. Phys. D: Appl. Phys.* **43**, 425404 (2010).
88. H. J. Schindler, *Int. J. Sol. Struct.* **42**, 717 (2005).
89. P. Leroux, *Adv. Mater. Processes* **34–35**, (2011).
90. A. S. Maxwell *et al.*, *Polym. Test.* **30**, 366 (2011).
91. J. Mencik, L. H. He and J. Nemecek, *Polym. Test.* **30**, 101 (2011).
92. C. Godoy *et al.*, *Tribology Int.* **42**, 1021 (2009).
93. C. A. Schuh, *Materials Today*, **9**(5), 32-40 (2006).
94. D. F. Bahr, S. L. Jennerjohn and D. J. Morris, *JOM* **61**(2), 56 (2009).
95. R. W. Armstrong, H. Shin and A. W. Ruff, *Acta Metall. Mater.* **43**(3), 1037 (1995).
96. Y. Y. Lim and M. M. Chaudhri, *Philos. Mag. A* **79**(12), 2979 (1999).
97. W. W. Gerberich *et al.*, *J. Appl. Mech.* **69**, 433 (2002).
98. S. Basu and M. W. Barsoum, *J. Mater. Res.* **22**(9), 2470 (2007).
99. S. R. Kalidindi and S. Pathak, *Acta Mater.* **56**, 3523 (2008).
100. S. Pathak, J. Shaffer and S. Kalidindi, *Scr. Mater.* **60**, 439 (2009).

101. A. C. Fischer-Cripps, *J. Mater. Res.* **22**(11), 3075 (2007).
102. O. Bartier, X. Hernot and G. Mauvoisin, *Mech. Mater.* **42**, 640 (2010).
103. P. J. Wei, P. W. Tsai and J. F. Lin, *Tribology Int.* **41**, 1247 (2008).
104. D. F. Bahr and G. Vasquez, *J. Mater. Res.* **20**(8), 1947 (2005).
105. E. K. Njiem and D. F. Bahr, *Scr. Mater.* **62**, 598 (2010).
106. I. Salehinia and D. F. Bahr, *Scr. Mater.* **66**, 339 (2012).
107. I. Salehinia and D. F. Bahr, *Mater. Sci. Tech.* **28**(9–10), 1141 (2012).
108. E. Tal-Gutelmacher *et al.*, *Scr. Mater.* **63**, 1032 (2010).
109. B. Poon, D. Rittel and G. Ravichandran, An analysis of nanoindentation in linear elastic solids, *Int. J. Sol. Struct.* **45**, 6018-6033 (2008); An analysis of nanoindentation in elasto-plastic solids, *Ibid.*, 6399-6415.
110. I. N. Sneddon, *Proc. Cambr. Philos. Soc.* **44**, 492 (1948).
111. Z.-H. Xu and X. Li, *Acta Mater.* **56**, 1399 (2008).
112. Y. F. Gao and J. Lou, *J. Nanomaterials* **2008**, 380961 (2008).
113. T. Li *et al.*, *Mater. Sci. Tech.* **28**(9–10), 1055 (2012).
114. M. A. Lodes *et al.*, *Acta Mater.* **58**, 4264 (2010).
115. P. Sadrabadi, K. Durst and M. Goeken, *Acta Mater.* **57**, 1281 (2009).
116. K. Durst *et al.*, *Acta Mater.* **54**, 2547 (2006).
117. M. Fujikane *et al.*, *Appl. Phys. Lett.* **101**, 201901 (2012).
118. J. Zhao, L. F. Ma and A. M. Korsunsky, *Mater. Sci. Tech.* **28**(9–10), 1167 (2012).
119. B. Yan and J. Zhao, *Int. J. Fract.* **155**, 119 (2009).
120. Q. Peng *et al.*, *Model. Simul. Mater. Sci. Eng.* **18**, 075003 (2010).
121. H. Huang *et al.*, *Mater. Sci. Eng. A* **523**, 193 (2009).
122. N. P. Daphalapurkar *et al.*, *Exp. Mech.* **51**, 719 (2011).
123. M. Zou and D. Yang, *Tribology Lett.* **22**(2), 189 (2006).
124. J. Konnerth *et al.*, *J. Mater. Sci.* **44**, 4399 (2009).
125. J. Chen *et al.*, *J. Phys. D: Appl. Phys.* **43**, 425404 (2010).
126. V. Dominich *et al.*, *Appl. Phys. Lett.* **81**, 3783 (2002).
127. O. Sahin *et al.*, *Mater. Charact.* **59**(4), 427 (2008).
128. G. Feng and A. H. W. Ngan, *Scr. Mater.* **45**, 971 (2001).
129. R. Nagar *et al.*, *J. Appl. Phys.* **108**, 063519 (2010).
130. D. G. Rickerby and N. H. Macmillan, *Mater. Sci. Eng.* **40**, 251 (1979).
131. R. W. Armstrong and C. C. Wu, *J. Am. Ceram. Soc.* **61**, 102 (1978).
132. B. L. Hammond and R. W. Armstrong, *Philos. Mag. Lett.* **57**, 41 (1988).
133. G. Feng and W. D. Nix, *Scr. Mater.* **51**, 599 (2004).
134. Z. Zong *et al.*, *Mater. Sci. Eng. A* **434**, 178 (2006).
135. W. J. Cousins, R. W. Armstrong and W. H. Robinson, *J. Mater. Sci.* **10**, 1655 (1975).
136. E. H. Yoffe, *Philos. Mag.* **50**(6), 813 (1984).
137. D. X. Liu, Z. D. Zhang and L. Z. Sun, *J. Mater. Res.* **25**(11), 2197 (2010).
138. W. W. Chen *et al.*, *J. Tribology* **133**, 041404 (2011).
139. M. E. Dokukin and I. Sokolov, *Macromolecules* **45**, 4277 (2012).
140. V. M. Kindrchuk *et al.*, *J. Mater. Sci.* **44**, 2599 (2009).
141. G. Fu and T. Cao, *Mater. Sci. Eng. A* **513–514**, 276 (2009).
142. M. H. Mueser, *Phys. Rev. Lett.* **100**, 055504 (2008).
143. D. Ma, C. W. Ong and T. Zhang, *Exp. Mech.* doi:10.1007/s11340-008-9177-6 (2008).
144. Y. P. Zhang *et al.*, *Meas. Sci. Tech.* **20**, 045706 (2009).
145. D. Ma and C. W. Ong, *J. Mater. Res.* **25**(6), 1131 (2010).
146. C. Lu *et al.*, *Philos. Mag. Lett.* **87**(6), 409 (2007).

147. S. J. Lloyd, J. M. Molina-Aldareguia and W. J. Clegg, *Philos. Mag. A* **82**(10), 1963 (2002).
148. N. I. Tymiak and W. W. Gerberich, *Philos. Mag.*, **87**(33), 5169 (2007); *Ibid.* 5169-5188.
149. W. Mao and Y. Shen, *J. Am. Ceram. Soc.* **95**(11), 3605 (2012).
150. Y. Gaillard, C. Tromas and J. Woirgard, *Acta Mater.* **54**, 1409 (2006).
151. W. C. Oliver and G. M. Pharr, *J. Mater. Res.* **7**, 1564 (1992).
152. L. Ferranti, Jr., R. W. Armstrong and N. N. Thadhani, *Mater. Sci. Eng. A* **371**, 251 (2004).
153. C. Feng *et al.*, *Exp. Mech.* **50**, 737 (2010).
154. Y. F. Gao and G. M. Pharr, *Scr. Mater.* **57**, 13 (2007).
155. Y. W. Bao, W. Wang and Y. C. Zhou, *Acta Mater.* **52**, 5397 (2004).
156. J. Aguilar-Santillan, *Acta Mater.* **56**, 2476 (2008).
157. R. R. Chromik *et al.*, *JOM*, **55**(6), 66 (2003).
158. B. J. Vincent, R. Gee and S. C. Hunter, A study of rapid micro-yielding in mild steel by scleroscopic methods, *The Properties of Materials at High Rates of Strain* (The Institution of Mechanical Engineers, London, UK, 1957), pp. 51–65.
159. H. Hertz, *J. Reine Angew. Math.* **92**, 156 (1881).
160. Y. Tirupataiah, B. Venkataraman and G. Sundararajan, *Mater. Sci. Eng. A* **124**, 133 (1990).
161. I. I. Argatov and Yu. A. Fadin, *J. Friction Wear* **30**(1), 1 (2009).
162. C. Y. Wu, C. Thornton and L. Y. Li, *Int. J. Mod. Phys. B* **22**, 1095 (2008).
163. R. B. Clough, S. C. Webb and R. W. Armstrong, *Mater. Sci. Eng. A* **360**, 396 (2003).
164. Y. Tirupataiah and G. Sundararajan, *Int. J. Impact Eng.* **9**(2), 237 (1990).
165. G. Sundararajan, *Mater. Sci. Tech.* **28**(9–10), 1101 (2012).
166. S. Hanagud and B. Ross, *AIAA J.* **9**(5), 905 (1971).
167. L. E. Murr, *Mater. Sci. Tech.* **28**(9–10), 1108 (2012).
168. M. M. Chaudhri, Dislocations and indentations, in *Dislocations in Solids*, Vol. 12, eds. F. R. N. Nabarro and J. P. Hirth (Elsevier B.V., Oxford, UK, 2004), Ch. 70, pp. 447–550.
169. R. B. Leavy, R. M. Brannon and O. E. Strack, *Int. J. Appl. Ceram. Tech.* **7**(5), 606 (2010).
170. T. J. Holmquist and A. A. Wereszczak, *Int. J. Appl. Ceram. Tech.* **7**(5), 625 (2010).
171. F. Mohs, *Grundriss der Mineralogie* (Arnold, Dresden, 1822).
172. E. Schmid and W. Boas, *Kristallplastizitaet* (Julius Springer, Berlin, 1935).
173. A. Reis and L. Zimmermann, *Z. Physikal. Chem.* **102**, 298 (1922).
174. K. Przibram, Zur Plastizitaet und Haerte von Alkalihalogenkristallen. 1, *Akad. Wiss. Wien. Ber.* **141**, 645–649 (1932); Zur Plaztizitaet und Haerte von Alkalihalogenkristallen. 2, *Ibid.* **142**, 259–261 (1933).
175. J. J. Gilman, *J. Appl. Phys.* **44**(3), 982 (1973).
176. J. J. Gilman, *J. Appl. Phys.* **41**, 1664 (1970).
177. J. J. Gilman, *Science* **261**, 1436 (1993).
178. N. Gane and J. M. Cox, *Philos. Mag.* **23**, 229 (1971).
179. P. Humble and R. H. J. Hannink, The plastic deformation of diamond at room temperature, in: *Physics of Materials; A Festschrift for Dr. Walter Boas on the Occasion of his 75th Birthday* (Griffin Press, Melbourne, Australia, 1979), pp. 145–153.
180. O. N. Grigor'ev, Investigation of the plasticity and strength properties of superhard materials by microindentation methods, *Sov. Powder Metall. Met. Ceram.* **21**, 65–73

(1982); (Transl.) *Poroshkovaya Metallurgiya*, **229**(1), 74–84 (1982).
181. C. A. Brookes, V. R. Howe and A. R. Parry, *Nature* **332**, 139 (1988).
182. R. J. Stokes, T. L. Johnston and C. H. Li, *Trans. Met. Soc. AIME* **215**, 437 (1959).
183. D. R. Pande and T. S. Murty, *J. Phys. D: Appl. Phys.* **7**, 403 (1974).
184. H. G. Gallagher *et al.*, *Phil. Trans. R. Soc. London A* **339**, 293 (1992).
185. W. L. Elban and R. W. Armstrong, *Acta Mater.* **46**, 6041 (1998).
186. K. A. Nibur, F. Akasheh and D. F. Bahr, *J. Mater. Sci.* **42**, 889 (2007).
187. J. J. Gilman, W. G. Johnston and G. W. Sears, *J. Appl. Phys.* **29**(5), 747 (1958).
188. W. G. Johnston and J. J. Gilman, *J. Appl. Phys.* **30**, 129 (1959).
189. J. J. Gilman and W. G. Johnston, Dislocations in lithium fluoride crystals, in: *Solid State Physics*, Vol. 13, eds F. Seitz and D. Turnbull (Academic Press, New York, 1962), pp. 147–222.
190. A. S. Keh, *J. Appl. Phys.* **31**, 1538 (1960).
191. A. A. Urusovskaya and R. Tyagaradzhan, *Sov. Phys. Crystallog.* **9**, 440 (1964).
192. V. B. Pariiskii, *Phys. Stat. Sol.* **19**, 525 (1967).
193. C. C. Chen and A. A. Hendrickson, *J. Appl. Phys.* **42**(6), 2208 (1971).
194. S. M. Hu, *J. Appl. Phys.* **46**(4), 1470 (1975).
195. P. J. Halfpenny, K. J. Roberts and J. N. Sherwood, *J. Mater. Sci.* **19**, 1629 (1984).
196. W. L. Elban and R. W. Armstrong, Microhardness study of RDX to assess localized deformation and its role in hot spot formation, in: *Seventh (Int.) Symp. on Detonation* (Naval Surf. Weapons, Center, Arlington, VA, 1981), NSWC MP 82-334, pp. 976–982.
197. W. L. Elban *et al.*, *J. Mater. Res.* **24**, 1273 (1989).
198. Y. Miura, *J. Appl. Phys.* **43**, 2917 (1972).
199. H. Harada and K. Sumino, *J. Appl. Phys.* **53**(7), 4838 (1982).
200. G. A. Schneider, T. Scholz and F. J. Espinosa-Beltran, *Appl. Phys. Lett.* **92**, 022906 (2008).
201. M. J. Klopstein and D. A. Lucca, *Appl. Phys. Lett.* **87**, 131906 (2005).
202. M. A. Velednitskaya *et al.*, *Phys. Stat. Sol.* (*A*) **32**, 123 (1975).
203. F. Gilberteau *et al.*, *Rev. Phys. Appl.* **17**, 777 (1982).
204. Y. Gaillard, C. Tromas and J. Woirgard, *Acta Mater.* **51**, 1059 (2003).
205. W. L. Elban *et al.*, *Investigation of the Origin of Hot Spots in Deformed Crystals: Studies on Ammonium Perchlorate and Reference Inert Materials*, Annual Progress Report No. 1, 1 April 1987 – 31 March 1988 (Naval Surface Weapons Center, Dahlgren, VA, Silver Spring, MD, 1988), NSWC MP 88-178.
206. S. Mendelson, *J. Appl. Phys.* **32**(10), 1999 (1961).
207. Y. Gaillard, C. Tromas and J. Woirgard, *Philos. Mag. Lett.* **83**(9), 553 (2003).
208. I. N. Sneddon, *Int. J. Eng. Sci.* **3**, 47 (1965).
209. Z. Dong, H. Huang and R. Kang, *Mater. Sci. Eng. A* **527**, 4177 (2010).
210. V. I. Savenko and E. D. Shchukin, *Phys. Sol. State* **54**(11), 2256 (2012).
211. R. W. Armstrong, X-ray topography of hardness indentations, in: *Applications of X-ray Topographic Methods to Materials Science*, eds. S. Weissmann, F. Balibar and J.-F. Petroff (Plenum Press, New York, 1984), pp. 295–300.
212. R. W. Armstrong and C. C. Wu, X-ray diffraction microscopy, in: *Microstructural Analysis: Tools and Techniques*, eds. J. L. McCall and W. M. Mueller (Plenum Press, New York, 1973), pp. 169–219.
213. R. W. Armstrong and A. C. Raghuram, Anisotropy of microhardness in crystals, in *The Science of Hardness Testing and Its Research Applications*, eds. J. H. Westbrook and H. Conrad (Amer. Soc. Met., Metals Park, OH, 1973), Ch. 13, pp. 174–186.
214. K.-C. Yoo *et al.*, *J. Mater. Sci. Lett.* **3**, 560 (1984).

215. G. Feng *et al.*, *J. Appl. Phys.* **104**, 043501 (2008).
216. R. W. Armstrong and W. L. Elban, Dislocations in energetic crystals, in: *Dislocations in Solids*, Vol. 12, eds. F. R. N. Nabarro and J. P. Hirth (Elsevier B.V., Oxford, UK, 2004), Ch. 69, pp. 403–446.
217. W. L. Elban, J. C. Hoffsommer and R. W. Armstrong, *J. Mater. Sci.* **19**, 552 (1984).
218. W. L. Elban *et al.*, *J. Mater. Sci.* **24**, 1273 (1989).
219. P. J. Halfpenny, K. J. Roberts and J. N. Sherwood, *J. Cryst. Growth* **67**, 202 (1984).
220. P. J. Halfpenny, K. J. Roberts and J. N. Sherwood, *J. Appl. Cryst.* **17**, 320 (1984).
221. P. J. Halfpenny, K. J. Roberts and J. N. Sherwood, *J. Cryst. Growth* **69**, 73 (1984).
222. P. J. Halfpenny, K. J. Roberts and J. N. Sherwood, *Philos. Mag.* **53**, 531 (1986).
223. K.-C. Yoo *et al.*, *Scr. Metall.* **15**(11), 1245 (1981).
224. Y. Wang *et al.*, *Acta Mater.* **52**, 2229 (2004).
225. M. Rester, C. Motz and R. Pippan, *Scr. Mater.* **59**, 742 (2008).
226. Y. Lim *et al.*, *Int. J. Plast.* **24**, 1990 (2008).
227. G. Feng *et al.*, *J. Appl. Phys.* **104**, 043501 (2008).
228. M. K. Khan *et al.*, *Acta Mater.* **59**, 7508 (2011).
229. M. M. Chaudhri, J. T. Hagan and J. K. Wells, *J. Mater. Sci.* **15**, 1189 (1980).
230. L. M. Brown, M. Younuis Khan and M. M. Chaudhri, *Phil. Mag.* **57**, 187 (1988).
231. M. M. Chaudhri, *Philos. Mag. Lett.* **77**(1), 7 (1998).
232. A. M. Minor *et al.*, *Philos. Mag.* **85**(2–3), 323 (2005).
233. C. R. Das *et al.*, *Appl. Phys. Lett.* **96**, 253113 (2010).
234. D. Chrobak *et al.*, *Nat. Nanotech.* **6**, 480 (2011).
235. R. Nowak *et al.*, *Nat. Nanotech.* **4**(5), 287 (2009).
236. R. Nowak *et al.*, *Mater. Sci. Tech.* **28**(9–10), 1202 (2012).
237. K. Sangwal, P. Gorostiza and F. Sanz, *Surf. Sci.* **446**, 314 (1999).
238. C. Tromas *et al.*, *J. Mater. Sci.* **34**, 5337 (1999).
239. Y. Gaillard, C. Tromas and J. Woirgard, Atomic force microscopy and nanoetching, in: *Proc. 25th Risoe Int. Symp.: Evolution of Deformation Microstructures*, eds. C. Gundlach *et al.*(Risoe National Lab., Roskilde, DK, 2004), pp. 311–316.
240. P. D. Tall, C. Coupeau and J. Rabier, *Scr. Mater.* **49**, 903 (2003).
241. R. R. Chromik *et al.*, *JOM*, **56**(6), 66 (2003).
242. I. Szlufarska, *Materials Today* **9**(5), 42 (2006).
243. R. E. Miller, L. E. Shilkrot and W. A. Curtin, *Acta Mater.* **52**, 271 (2004).
244. Y.-C. Chen *et al.*, *Appl. Phys. Lett.* **93**, 171908 (2008).
245. K. Nishimura *et al.*, *Appl. Phys. Lett.* **92**, 161904 (2008).
246. M. Solar *et al.*, *J. Phys. D: Appl. Phys.* **43**, 455406 (2010).
247. Y. Zhong and T. Zhu, *Comput. Meth. Appl. Mech. Engrg.* **197**, 3174 (2008).
248. T.-H. Fang, W.-Y. Chang and J. J. Huang, *Acta Mater.* **57**, 3341 (2009).
249. T. Tsuru, Y. Shibutani and Y. Kaji, *Acta Mater.* **58**, 3096 (2010).
250. J. Alcala *et al.*, *Phys. Rev. Lett.* **109**, 075502 (2010).
251. K. Edalati and Z. Horita, *Scr. Mater.* **64**, 161 (2011).
252. S. Grasso *et al.*, *Scr. Mater.* **64**, 256 (2011).
253. G. Fu and T. Cao, *Mater. Sci. Eng. A* **513–514**, 276 (2009).
254. E. Gualtieri *et al.*, *Tribology Int.* **42**, 699 (2009).
255. Q. Ping *et al.*, *Model. Simul. Mater. Sci. Eng.* **18**, 075003 (2010).
256. S. Qu and H. Zhou, *Nanotech.* **21**, 335704 (2010).
257. W. B. Lee and Y. P. Chen, *Int. J. Plast.* **26**, 1527 (2010).
258. F. Knoop, C. G. Peters and W. B. Emerson, *J. Res. Natl. Bur. Stand.* **23**, 39 (1939).
259. H. Winchell, *Am. Mineralogist*, **30**, 585 (1945).
260. F. W. Daniels and C. G. Dunn, *Trans. Am. Soc. Met.* **41**, 419 (1949).

261. C. A. Brookes, J. B. O'Neill and B. A. W. Redfern, *Proc. Roy. Soc. London A* **322**, 73 (1971).
262. R. W. Calder and R. W. Armstrong, *Mater. Sci. Eng.* **12**(1), 59 (1973).
263. C. A. Brookes, Hardness Measurements in the Evaluation of Hard Materials, in: *Science of Hard Materials*, eds. R. K. Viswanadham, D. J. Rowcliffe and J. Gurland (Plenum Press, New York, 1983), pp. 181–199.
264. P. M. Sargent and T. F. Page, *J. Mater. Sci.* **20**, 2388 (1985).
265. J. B. O'Neill, B. A. W. Redfern and C. A. Brookes, *J. Mater. Sci.* **8**, 47 (1973).
266. H. G. Gallagher *et al.*, *Cryst. Latt. Def. Amorph. Mat.* **16**, 137 (1987).
267. S. G. Roberts, *Philos. Mag. A* **58**, 347 (1988).
268. H. Li and R. C. Bradt, *Mater. Sci. Eng. A* **142**(1), 51 (1991).
269. H. G. Gallagher *et al.*, *Proc. Roy. Soc. London A* **339**, 293 (1992).
270. N. Vaiyda *et al.*, *Bull. Mater. Sci.* **20**(3), 333 (1997).
271. D. B. Sirdeshmukh *et al.*, *Bull. Mater. Sci.* **24**, 469 (2001).
272. S. Karan and S. P. Sen Gupta, *Mater. Sci. Eng. A* **398**, 198 (2005).
273. C. Zambaldi and D. Raabe, *Acta Mater.* **58**, 3516 (2010).
274. B. Eidel and F. Gruttmann, *Comput. Mater. Sci.* **39**, 172 (2007).
275. B. Eidel, *Acta Mater.* **59**, 1761 (2011).
276. R. W. Armstrong and S. Javadpour, Dislocation mechanics description of plastic anisotropy and fracturing observations in textured Al-Li 2090-T8E41 alloy, in: *Fourth International Conference on Aluminum Alloys*, ICAA4 (Georgia Inst. Tech. Atlanta, GA, 2004), pp. 405–409.
277. A. Yonezu *et al.*, *Mater. Sci. Eng. A* **527**, 7646 (2010).
278. S. Gollapudi *et al.*, *Scr. Mater.* **64**, 189 (2011).
279. E. O. Hall, *Nature* **173**, 948 (1954).
280. R. W. Armstrong *et al.*, *Philos. Mag.* **7**, 45 (1962).
281. P. C. Jindal and R. W. Armstrong, *Trans. TMS-AIME*, **239**, 1856 (1967).
282. W. H. Bassett and C. H. Davis, *Trans. TMS-AIME* **60**, 428 (1919).
283. C. H. Mathewson, *Trans. TMS-AIME* **60**, 451 (1919).
284. W. J. Babyak and F. N. Rhines, *Trans. TMS-AIME* **218**, 21 (1960).
285. H. Hu and R. S. Cline, *Trans. TMS-AIME* **242**, 1013 (1968).
286. R. W. Armstrong and P. C. Jindal, *Trans. TMS-AIME* **242**, 2613 (1968).
287. P. C. Jindal and J. Gurland, *Metall. Trans.* **5**, 1649 (1974).
288. Y. Y. Lim and M. M. Chaudhri, *Philos. Mag. A* **82**(10), 2071 (2002).
289. X. D. Hou, A. J. Bushby and N. M. Jennet, *J. Phys. D: Appl. Phys.* **41**, 074006 (2008).
290. B. Ehrler *et al.*, *Philos. Mag.* **88**, 3043 (2008).
291. X. D. Hou, A. J. Bushby and N. M. Jennett, *Meas. Sci. Technol.* **21**, 115105 (2010).
292. X. D. Hou and N. M. Jennett, *Acta Mater.* **60**, 4128 (2012).
293. F. J. Zerilli and R. W. Armstrong, *J. Appl. Phys.* **61**, 1816 (1987).
294. D. A. Konstantinidis and E. C. Aifantis, *NanoStruct. Mater.* **10**(7), 1111 (1998).
295. T. Eliash *et al.*, *Acta Mater.* **56**, 5640 (2008).
296. T. Ohmura and K. Tsuzaki, *J. Mater. Sci.* **42**, 1728 (2007).
297. T. Ohmura and K. Tsuzaki, *J. Phys. D: Appl. Phys.* **41**, 074015 (2008).
298. T. B. Britton, D. Randman and A. J. Wilkinson, *J. Mater. Res.* **24**(3), 607 (2009).
299. G. Z. Voyiadjis, A. H. Almasri and T. Park, *Mech. Res. Commun.* **37**, 307 (2010).
300. A. H. Almasri and G. Z. Voyiadjis, *Acta Mech.* doi:10.1007/s00707-009-0151-x (2009).
301. S. Qu and H. Zhou, *Nanotech.* **21**, 335704 (2010).
302. L. Zhang *et al.*, *J. Mater. Res.* (9) (2009).
303. H. Sumiya and T. Irifume, *J. Mater. Res.* **22**(8), 2345 (2007).

304. F. Gao, *J. Appl. Phys.* **112**, 023506 (2012).
305. M. A. Z. Vasconcellos, S. C. Lima and R. Hinrichs, *Revista Mater.* **15**(2), 334 (2010).
306. S. J. Bull *et al.*, *Mater. Sci. Tech.* **28**(9–10), 1177 (2012).
307. R. W. Armstrong, *J. Mech. Phys. Sol.* **9**, 196 (1961).
308. H. C. Lee and J. Gurland, *Mater. Sci. Eng.* **33**, 125 (1978).
309. R. W. Armstrong and O. Cazacu, *Int. J. Refract. Met. Hard Mater.* **24**, 129 (2006).
310. V. Richter and M. von Ruthendorf, *Int. J. Refract. Met. Hard Mater.* **17**, 141 (1999).
311. L. Makhele-Lekala, S. Luyckx and F. R. N. Nabarro, *Int. J. Refract. Met. Hard Mater.* **19**, 245 (2001).
312. R. W. Armstrong, *Materials* **4**(7), 1287 (2011).
313. B. Aldousiri *et al.*, *Poly. Test.* **30**, 688 (2011).
314. S. Shao *et al.*, *J. Appl. Phys.* **112**, 044307 (2012).
315. A. S. Keh, J. C. M. Li and Y. T. Chou, *Acta Metall.* **7**, 694 (1959).
316. Y. T. Chou, F. Garofalo and R. W. Whitmore, *Acta Metall.* **8**, 480 (1960).
317. Y. Gaillard, C. Tromas and J. Woirgard, *Acta Mater.* **54**, 1409 (2006).
318. R. W. Armstrong and W. L. Elban, Dislocation aspects of plastic flow and cracking at indentations in magnesium oxide and cyclotrimethylenetrinitramine explosive crystals, in: *Microindentation Techniques in Materials Science and Engineering*, eds. P. J. Blau and B. R. Lawn (Amer. Soc. Test. Mater., Philadelphia, PA, 1986), pp. 109–126.
319. M. M. Chaudhri, *Phil. Mag. Lett.* **53**, L55 (1986).
320. N. Khasgiwale and H. M. Chan, *Acta Metall. Mater.* **43**, 207 (1995).
321. B. Y. Farber, A. S. Chiarelli and A. H. Heuer, *Philos. Mag. A* **70**, 201 (1994).
322. K. J. Ramos, D. E. Hooks and D. F. Bahr, *Philos. Mag.* **89**, 2381 (2009).
323. J. T. Hagen and M. M. Chaudhri, *J. Mater. Sci.* **12**(5), 1055 (1977).
324. W. L. Elban, *J. Mater. Sci.* **14**, 1008 (1979).
325. R. W. Armstrong and W. L. Elban, *Mater. Sci. Eng. A* **111**, 35 (1989).
326. W. L. Elban *et al.*, *Summary Report: Microstructural Origins of Hot Spots in RDX Explosive and Several Reference Inert Materials*, Summary Report (Naval Surface Weapons Center, Silver Spring, MD, 1984), NSWC MP 84-358.
327. R. W. Armstrong and W. L. Elban, *Mater. Sci. Tech.* **22**, 381 (2006).
328. Z. Dong, H. Huang and R. Kang, *Mater. Sci. Eng. A* **527**, 4177 (2010).
329. H. Y. Lin, J. L. Chu and S. Lee, *J. Mater. Sci.* **36**, 3769 (2001).
330. B. Yan and J. Zhao, *Int. J. Fract.* **155**, 119 (2009).
331. V. R. Thalladi *et al.*, *J. Am. Chem. Soc.* **124**, 9912 (2002).
332. R. W. Armstrong, *Eng. Fract. Mech.* **77**, 1348 (2010).
333. R. W. Armstrong, *Int. J. Refract. Met. Hard. Mater.* **19**, 251 (2001).
334. R. W. Armstrong, L. Ferranti, Jr. and N. N. Thadhani, *Int. J. Refract. Met. Hard Mater.* **24**, 11 (2006).
335. H. Wan *et al.*, *J. Mater. Res.* **22**(11), 2224 (2010).
336. R. W. Armstrong, A. W. Ruff and H. Shin, *Mater. Sci. Eng. A* **209**, 91 (1996).
337. K. Sangwal, *Cryst. Res. Technol.* **44**(10), 1019 (2009).
338. B. Yan and J. Zhao, *Int. J. Fract.* **155**, 119 (2009).
339. J. J. Guo *et al.*, *Acta Mater.* doi:10.1016/j.actamat.2010.11.034.
340. Q. K. Zhang, J. Tan and Z. F. Zhang, *J. Appl. Phys.* **110**, 014502 (2011).
341. R. B. Clough and H. N. G. Wadley, *Met. Trans. A* **13**, 1965 (1982).
342. R. J. Roberts, R. C. Crowe and P. York, *Pharmacy Pharmacol. Commun.* **1**, 501 (1995).
343. K. Gopalakrishnan and J. J. Mecholsky, Jr., *J. Am. Ceram. Soc.* **95**(11), 3622 (2012).
344. S. Yoshida *et al.*, *J. Mater. Res.* **25**(11), 2203 (2010).

345. Y. Kato *et al.*, *J. Ceram. Soc. Jpn.* **119**(2), 110 (2011).
346. J. E. Neely and J. D. Mackenzie, *J. Mater. Sci.* **3**, 603 (1968).
347. M. Yamane and J. D. Mackenzie, *J. Non-Cryst. Sol.* **15**, 153 (1974).
348. J. T. Hagan, *J. Mater. Sci.* **14**(2), 462 (1979).
349. J. T. Hagan, *J. Mater. Sci.* **15**, 1417 (1980).
350. D. A. Gorham, A. D. Salman and H. Tan, *Philos. Mag.* **82**,(10), 2231 (2002).
351. N. Iwashita, J. S. Field and M. V. Swain, *Philos. Mag.* **82**(10), 1873 (2002).
352. M. M. Smedskjaer, J. C. Mauro and Y. Yue, *Phys. Rev. Letts.* **105**, 115503 (2010).
353. M. M. Smedskjaer *et al.*, *J. Chem. Phys.* **133**, 154509 (2010).
354. C. E. Packard *et al.*, *J. Mater. Res.* **25**(12), 2251 (2010).
355. B.-G. Yoo and J.-I. Jang, *J. Phys. D: Appl. Phys.* **41**, 07417 (2008).
356. B.-G. Yoo *et al.*, *Scr. Mater.* **61**, 951 (2009).
357. K.-W. Chen and J.-F. Lin, *Int. J. Plast.* **26**, 1645 (2010).
358. R. Hill, *The Mathematical Theory of Plasticity* (Clarendon Press, Oxford, 1950).
359. H. Zhang *et al.*, *Acta Mater.* **53**(14), 3849 (2005).
360. A. L. Greer *et al.*, *Mater. Sci. Eng. A* **375**, 1182 (2004).
361. D. Pan *et al.*, *Appl. Phys. Lett.* **95**, 141909 (2009).
362. A. Paduraru *et al.*, *Model. Simul. Mater. Sci. Eng.* **18**, 055006 (2010).
363. J. C. Conway, Jr. and H. P. Kirchner, Shear flow and fracture beneath sharp indentations in soda-lime glass, in: *Fracture Mechanics of Ceramics 5: Surface Flaws, Statistics, and Microcracking*, eds. R. C. Bradt, *et al.*, (Plenum Press, New York, 1983), pp. 71–79.
364. M. Sakai, S. Shimizu and S. Ito, *J. Am. Ceram. Soc.* **85**(5), 1210 (2002).
365. D. K. Misra *et al.*, *Sci. Technol. Adv. Mater.* **9**, 045004 (2008).
366. P. Jannotti *et al.*, *J. Eur. Ceram. Soc.* **32**, 1551 (2012).
367. S. T. Liu *et al.*, *Scr. Mater.* **67**, 9 (2012).
368. W. Kauzmann, *Trans. TMS-AIME* **143**, 57 (1941).
369. R. W. Armstrong and S. M. Walley, *Int. Mater. Rev.* **53**(3), 105 (2008).
370. S. M. Walley and J. E. Field, *DYMAT J.* **1**(3), 211 (1994).
371. W. W. Chen *et al.*, *J. Tribology* **133**, 041404 (2011).
372. C. G. N. Pelletier *et al.*, *Philos. Mag.* **88**(9), 1291 (2008).
373. E. G. Herbert, *The Engineer* **135**, 686 (1923).
374. F. Hargreaves, *J. Inst. Met.* **39**, 301 (1928).
375. G. Sundararajan and Y. Tirupataiah, The localization of plastic flow under dynamic indentation conditions; 1. Experimental results, *Acta Mater.* **54**(3), 565–575 (2006); 2. Analysis of results", *Ibid.* 577–586.
376. J. Wu *et al.*, *Mater. Sci. Eng. A* **417**, 114 (2006).
377. A. H. Almasri and G. Z. Voyiadjis, *J. Eng. Mater. Tech.* **129**, 505 (2007).
378. B. Xu, Z. Yue and X. Chen, *J. Phys. D: Appl. Phys.* **43**, 245401 (2010).
379. J. C. M. Li, *Mater. Sci. Eng. A* **322**, 23 (2002).
380. I.-C. Choi *et al.*, *J. Mater. Res.* **27**(1), 3 (2011).
381. R. M. Shalaby, *Cryst. Res. Technol.* **45**(4), 427 (2010).
382. H. Somekawa and T. Mukai, *Philos. Mag. Lett.* **90**(12), 883 (2010).
383. Y. Yokouchi, T. W. Chou and I. G. Greenfield, *Met Trans. A* **14**, 2415 (1983).
384. S. Basu, M. Radovic and M. W. Barsoum, *J. Appl. Phys.* **104**, 063522 (2008).
385. J. D. Williams *et al.*, Dynamic hardness testing of polycrystalline MgO, in: *Structures Congress '91 Compact Papers*, ed. T. J. Williamson (Amer. Soc. Civil Engrs., New York, 1991), pp. 287–290.
386. M. M. Chaudhri, J. K. Wells and A. Stephens, *Philos. Mag. A* **43**, 643 (1981).
387. E. L. Tobolski, *Adv. Mater. Process.* **168**(6), 16 (2010).

388. E. A. Baxevani and A. E. Giannakopoulos, *Exp. Mech.* **49**, 371 (2008).
389. S. G. Roberts, *Brit. Ceram. Trans.* **99**, 31 (2000).
390. R. B. Leavy, R. M. Brannon and O. E. Strack, *Int. J. Appl. Ceram. Tech.* **7**(5), 606 (2010).
391. T. T. Zhu, A. J. Bushby and D. J. Dunstan, *J. Mech. Phys. Sol.* **56**, 1170 (2008).
392. A. Krell and S. Schaedlich, *Int. J. Refract. Met. Hard Mater.* **19**, 237 (2001).
393. B. J. Kooi *et al.*, *Acta Mater.* **51**, 2859 (2003).
394. M. Doerner and W. D. Nix, *J. Mater. Res.* **1**(4), 601 (986).
395. H. Y. Yu, S. C. Sanday and B. B. Rath, *J. Mech. Phys. Sol.* **38**(6), 745 (1990).
396. R. Kulchytsky-Zhyhailo and G. Rogowski, *Tribology Int.* **43**, 1592 (2010).
397. D. Chicot *et al.*, *Thin Sol. Films* **518**, 5565 (2010).
398. N. Gitis *et al.*, Comprehensive mechanical and tribological characterization of ultra-thin-films, in: *Fundamentals of Nanoindentation and Nanotribology* (Mater. Res. Soc., Warrendale, PA, 2007), paper AA02-04.
399. M. J. Jaffar, *Tribology Lett.* **22**(3), 247 (2006).
400. C. T. McCarthy, M. Hussey and M. D. Gilchrist, On the sharpness of straight edge blades in cutting soft solids: Part I. — Indentation experiments, *Eng. Fract. Mech.* **74**, 2205–2224 (2007); Part II. — Analysis of blade geometry", *Ibid.* **77**, 437–451 (2010).
401. A.-T. Akona, P. M. Reis and F.-J. Ulm, *Phys. Rev. Lett.* **106**, 204302 (2011).
402. V. Keryvin *et al.*, *J. Phys. D: Appl. Phys.* **41**, 074029 (2008).
403. J. C. Ye *et al.*, *J. Appl. Phys.* **112**, 053516 (2012).
404. N. Hakiri, A. Matsuda and M. Sakai, *J. Mater. Res.* **24**, 1950 (2009).
405. Z. Zong and W. Soboyejo, *Mater. Sci. Eng. A* **404**, 281 (2005).
406. A. V. Bolesta and V. M. Fomin, *Phys. Mesomech.* **12**(3–4), 117 (2009).
407. G. Guisbiers *et al.*, *Appl. Phys. Lett.* **97**, 143115 (2010).
408. Q. Wang, R. Hu and Y. Shao, *J. Appl. Phys.* **112**, 044512 (2012).
409. C.-Y. Son, T. S. Yoon and S. Lee, *Metall. Mater. Trans.* **40**(5), 1110 (2009).
410. F. Kauffman *et al.*, *Scr. Mater.* **52**, 1269 (2005).
411. G. M. Spinks, H. R. Brown and Z. Liu, *Poly. Test.*, **25**, 868 (2006).
412. F. Dinelli *et al.*, *Macromolecules* **44**, 987 (2011).
413. E. Gacoin *et al.*, *Tribology Lett.* **21**(3), 245 (2006).
414. S. Bundschuh *et al.*, *Appl. Phys. Lett.* **101**, 101910 (2012).